

**QM/MM calculations on the  
membrane-bound hydrogenase from *Ralstonia  
eutropha***

vorgelegt von  
Diplom-Chemikerin  
Yvonne Rippers  
aus Meerbusch

von der Fakultät II – Mathematik und Naturwissenschaften  
der Technischen Universität Berlin  
zur Erlangung des akademischen Grades  
Doktor der Naturwissenschaften  
– Dr. rer. nat. –  
genehmigte Dissertation

Promotionsausschuss:

Vorsitzender: Prof. Dr. Roderich Süßmuth

Berichter: Prof. Dr. Maria Andrea Mroginski

Berichter: Prof. Dr. Petra Imhoff

Tag der wissenschaftlichen Aussprache: 02. Juli 2015

Berlin 2015



---

**Parts of this work have already been published in the following articles:**

1. Y. Rippers, T. Utesch, P. Hildebrandt, I. Zebger, M. A. Mroginski, *Insights into the structure of the active site of the O<sub>2</sub>-tolerant membrane bound [NiFe] hydrogenase of R. eutropha H16 by molecular modelling*, Phys. Chem. Chem. Phys. (2011), **13**, 16146–16149.
2. Y. Rippers, M. Horch, P. Hildebrandt, I. Zebger, M. A. Mroginski, *Revealing the Absolute Configuration of the CO and CN<sup>-</sup> Ligands at the Active Site of a [NiFe] Hydrogenase*, Chem. Phys. Chem. (2012), **13**, 3852–3856.
3. M. Horch, Y. Rippers, M. A. Mroginski, P. Hildebrandt, I. Zebger, *Combining Spectroscopy and Theory to Evaluate Structural Models of Metalloenzymes: A Case Study on the Soluble [NiFe] Hydrogenase from Ralstonia eutropha*, Chem. Phys. Chem. (2013), **14**, 158–191.
4. E. Siebert, M. Horch, Y. Rippers, J. Fritsch, S. Frielingsdorf, O. Lenz, F. Velazquez Escobar, F. Siebert, L. Paasche, U. Kuhlmann, F. Lenzian, M. A. Mroginski, I. Zebger, P. Hildebrandt, *Resonance Raman Spectroscopy as a Tool to Monitor the Active Site of Hydrogenases*, Angewandte Chemie-International Edition (2013), **52**, 5162–5165.
5. J. Salewski, F. Velazquez Escobar, S. Kaminski, D. von Stetten, A. Keidel, Y. Rippers, N. Michael, P. Scheerer, P. Piwowarski, F. Bartl, N. Frankenberg-Dinkel, S. Ringsdorf, W. Gaertner, T. Lamparter, M. A. Mroginski, P. Hildebrandt, *Structure of the Biliverdin Cofactor in the Pfr State of Bathy and Prototypical Phytochromes*, Journal of Biological Chemistry (2013), **288**, 16800–16814.
6. S. Frielingsdorf, J. Fritsch, A. Schmidt, M. Hammer, J. Loewenstein, E. Siebert, V. Pelmeshnikov, T. Jaenicke, J. Kalms, Y. Rippers, F. Lenzian, I. Zebger, C. Teutloff, M. Kaupp, R. Bittl, P. Hildebrandt, B. Friedrich, O. Lenz, P. Scheerer, *Reversible [4Fe-3S] cluster morphing in an O<sub>2</sub>-tolerant [NiFe] hydrogenase*, Nature Chemical Biology (2014), **10**, 378–385.
7. E. Siebert, Y. Rippers, S. Frielingsdorf, J. Fritsch, A. Schmidt, J. Kalms, S. Katz, O. Lenz, P. Scheerer, L. Paasche, V. Pelmeshnikov, U. Kuhlmann, M. A. Mroginski, I. Zebger, P. Hildebrandt, *Resonance Raman Spectroscopic Analysis of the [NiFe] Active Site and the Proximal [4Fe-3S] Cluster of an O<sub>2</sub>-tolerant Membrane-bound Hydrogenase in the Crystalline State*, Journal of Physical Chemistry (2015), *submitted*



# Abstract

Molecular hydrogen is a simple molecule which releases a large amount of energy when reacting with oxygen in the Knall-Gas-Reaction (572 kJ/mol). For this reason it is more frequently used as a clean energy source and as an alternative to  $CO_2$  emitting combustion energy sources.

Hydrogenases are metalloenzymes that are able to activate the hydrogen molecule at mild reaction conditions and cleave it into two protons and two electrons. Since this is a reversible process hydrogenases might be utilized to efficiently store and release high amounts of energy. For this reason gained a lot of attention given its particular potential in bioenergetic applications for alternative fuel productions. However, most hydrogenases are very sensitive towards oxygen. The membrane bound hydrogenase (MBH) from *Ralstonia eutropha* examined in this work is able to metabolize hydrogen even at ambient oxygen levels. Detailed knowledge of the mechanisms for the reversible hydrogen cleavage and the oxygen tolerance would greatly contribute to biomimetic catalysts applications. However, these mechanisms are still not clarified in all detail. The aim of this work was to elucidate structural details at the [NiFe] active site, where the hydrogen reaction takes place, and at the proximal iron sulfur cluster, which is essential for the oxygen tolerance of the MBH. As a tool, theoretical calculations of vibrational properties using the hybrid quantum mechanical / molecular mechanical (QM/MM) approach in combination with molecular dynamics (MD) simulations was chosen.

Before the x-ray crystallographic structure of the MBH from *Ralstonia eutropha* became available a structural model of the enzyme was constructed with the homology model technique in chapter 5. The modelled structure was confirmed by the comparison of vibrational infrared (IR) spectra computed at QM/MM level with experimental results. The modelled MBH could give first insights into the structure at the active site of an oxygen tolerant hydrogenase.

In chapter 6 the absolute active site configuration of the three inorganic ligands bound to the iron could be revealed, confirming former structural configuration suggestions. This work also aimed clarifying assigning problems concerning the inorganic ligands at the active site of the x-ray crystallographic structure of the reduced MBH published in 2011<sup>[11]</sup>.

After publication of the crystal structure of the reduced MBH, vibrational calculations at QM/MM level in combination with MD simulations on different reduced and light induced states of the active site (see figure 1.3) were performed and compared with experimental resonance Raman (RR) spectra. The results in chapter 7 demonstrate the potential of the RR spectroscopical technique to probe active site signals as alternative to IR spectroscopy. In combination with theoretical calculations a light induced state was identified and its structure previously proposed by Brecht et al.<sup>[5]</sup> was confirmed.

---

In chapter 8 results are presented for similar calculations as in chapter 7 that were repeated for different active site states of the oxidized MBH. In addition vibrational calculations were carried out on the proximal cluster of the superoxidized MBH. The comparison with RR experimental results confirmed the presence of a hydroxyl ligand at the iron sulfur cluster, which also has been detected in the crystal structure of the oxidized enzyme<sup>[9]</sup>. Furthermore, the QM/MM calculations enabled the assignment of probed active site signals to the MBH active state ( $Ni_a - S$  see figure 1.3).

Finally, the simulation of resonance Raman intensities was addressed and a new approach based on potential energy contribution weighting was developed as introduced in section 4.2.

# Zusammenfassung

Molekularer Wasserstoff ist ein einfaches Molekül, das in der Knallgasreaktion mit Sauerstoff viel Energie freisetzt (572 kJ/mol). Aus diesem Grund wird es immer häufiger als saubere Energiequelle und als Alternative zu  $CO_2$  emittierenden Verbrennungsenergiequellen in Betracht gezogen.

Hydrogenasen sind Metallenzyme, die in der Lage sind, Wasserstoff bei milden Reaktionsbedingungen zu aktivieren und in zwei Protonen und zwei Elektronen zu spalten. Da dies ein reversibler Prozess ist, können Hydrogenasen zur effizienten Lagerung und Freisetzung großer Energiemengen eingesetzt werden. Aus diesem Grund gewinnen sie immer mehr Aufmerksamkeit, da sie ein besonderes Potential in bioenergetischen Verwendungen für die alternative Treibstoffproduktion aufweisen. Allerdings sind die meisten Hydrogenasen sehr empfindlich gegenüber Sauerstoff. Die in dieser Arbeit untersuchte membrangebundene Hydrogenase (MBH) von *Ralstonia eutropha* kann Wasserstoff auch in der Gegenwart von natürlichen Sauerstoffmengen umsetzen. Ein detailliertes Wissen über den Mechanismus der reversiblen Wasserstoffspaltung und der Sauerstofftoleranz würde sehr zur Entwicklung biomimetischer Katalysatoranwendungen beitragen. Diese Mechanismen sind jedoch immer noch nicht im Detail geklärt.

Das Ziel dieser Arbeit war es, strukturelle Details des katalytisch aktiven [NiFe] Zentrums, an dem die Wasserstoffreaktion statt findet, und des proximalen Eisen-Schwefel-clusters, der eine wichtige Rolle in der Sauerstofftoleranz der MBH spielt, zu klären. Dazu wurden theoretische Berechnungen der Schwingungseigenschaften mittels des quantenmechanischen/molekularmechanischen (QM/MM) Ansatzes in Kombination mit moleküldynamischen (MD) Simulationen durchgeführt.

Bevor die röntgenkristallographische Struktur der MBH von *Ralstonia eutropha* verfügbar war, wurde in Kapitel 5 ein Strukturmodell für das Enzym mit Hilfe der Homologiemodell-Technik erstellt. Die modellierte Struktur wurde durch den Vergleich von QM/MM berechneten Infrarotspektren (IR) mit experimentellen Ergebnissen bestätigt. Diese modellierte MBH ermöglichte erstmals Einblicke in die Struktur des aktiven Zentrums einer sauerstofftoleranten Hydrogenase.

In Kapitel 6 wurde die absolute Konfiguration der an Eisen gebundenen, anorganischen Liganden im aktiven Zentrum aufgeklärt und bestätigte vorherige Vorschläge für die strukturelle Konfiguration. Diese Arbeit trug außerdem dazu bei, Zuordnungsprobleme der anorganischen Liganden im aktiven Zentrum der röntgenkristallographisch bestimmten Struktur der reduzierten MBH, die 2011 veröffentlicht wurde<sup>[11]</sup>, zu klären.

Nachdem die Kristallstruktur der reduzierten MBH veröffentlicht worden war, wurden schwingungsspek-

---

trooskopische Berechnungen auf QM/MM Level in Kombination mit MD Simulationen an verschiedenen reduzierten und lichtinduzierten Zuständen des aktiven Zentrums (siehe Abbildung 1.3) durchgeführt und mit experimentellen Resonanz Raman (RR) Spektren verglichen. Die Ergebnisse demonstrierten das Potential der RR Spektroskopie als Alternative zur IR Technik, Signale des aktiven Zentrums zu messen. In Kombination mit theoretischen Berechnungen konnte ein lichtinduzierter Zustand identifiziert und seine zuvor vorgeschlagene Struktur<sup>[5]</sup> bestätigt werden.

In Kapitel 8 werden die Ergebnisse zu ähnlichen Berechnungen wie in Kapitel 7 an verschiedenen Zuständen der oxidierten MBH vorgestellt. Zusätzlich wurden schwingungsspektroskopische Berechnungen für den proximalen Eisen-Schwefel-Cluster der superoxidierten MBH durchgeführt. Der Vergleich mit experimentellen RR Spektren bestätigte die Anwesenheit eines an ein Eisenatom des proximalen Clusters gebundenen Hydroxyliganden, der auch in der röntgenkristallographischen Struktur des oxidierten Enzyms<sup>[9]</sup> detektiert werden konnte. Außerdem ermöglichten die QM/MM Rechnungen die Zuordnung aufgezeichneter Signale vom aktiven Zentrum zum aktivierten Zustand der MBH ( $Ni_a - S$  siehe Abbildung 1.3). Schließlich wird in Abschnitt 4.2 die Simulation von resonanzverstärkten Raman-Intensitäten behandelt. Hierzu wurde ein neuer Ansatz entwickelt und angewendet, der Raman-Intensitäten auf der Basis individueller Schwingungsbeiträge zur potentiellen Energie gewichtet.

# Contents

<b>Abstract</b>	<b>III</b>
<b>Zusammenfassung</b>	<b>V</b>
<b>List of figures</b>	<b>IX</b>
<b>Abbreviations</b>	<b>XI</b>
<b>1 The Hydrogenases from <i>Ralstonia eutropha</i></b>	<b>1</b>
1.1 Introduction . . . . .	1
1.2 Structure . . . . .	2
1.2.1 Active site structure . . . . .	3
1.2.2 Proximal iron sulphur cluster . . . . .	4
1.3 Catalytic mechanism . . . . .	4
<b>2 Vibrational Spectroscopy</b>	<b>7</b>
2.1 Infrared Spectroscopy . . . . .	7
2.2 Raman Spectroscopy . . . . .	8
<b>3 Theoretical Background</b>	<b>13</b>
3.1 Quantum Mechanics . . . . .	13
3.1.1 Hartree Fock Method . . . . .	13
3.1.2 Density Functional Theory . . . . .	15
3.2 Molecular Mechanics . . . . .	17
3.2.1 Classical Force Fields . . . . .	17
3.2.2 Molecular Dynamics Simulation . . . . .	18
3.3 The combination of Quantum and Molecular Mechanics . . . . .	20
3.3.1 QM/MM partition . . . . .	20
3.3.2 Energy of the QM/MM system . . . . .	21
<b>4 Data Analysis</b>	<b>25</b>
4.1 Normal Mode Analysis . . . . .	25
4.1.1 Normal modes . . . . .	25
4.1.2 Internal Coordinates . . . . .	27
4.2 Resonance Raman Approach . . . . .	30

4.3	Correlation Analysis . . . . .	35
<b>5</b>	<b>Insights into the structure of the active site of the O<sub>2</sub>-tolerant membrane bound [NiFe] hydrogenase of <i>R. eutropha</i> H16 by molecular modelling</b>	<b>39</b>
<b>6</b>	<b>Revealing the Absolute Configuration of the CO and CN<sup>-</sup> Ligands at the Active Site of a [NiFe] Hydrogenase</b>	<b>45</b>
<b>7</b>	<b>Resonance Raman Spectroscopy as a Tool to Monitor the Active Site of Hydrogenases</b>	<b>51</b>
<b>8</b>	<b>Resonance Raman Spectroscopic Analysis of the [NiFe] Active Site and the Proximal [4Fe-3S] Cluster of an O<sub>2</sub>-tolerant Membrane-bound Hydrogenase in the Crystalline State</b>	<b>57</b>
<b>9</b>	<b>Appendix</b>	<b>71</b>
	<b>References</b>	<b>77</b>
	<b>Acknowledgement</b>	<b>85</b>

# List of Figures

1.1	the dimeric membrane bound hydrogenase from <i>Ralstonia eutropha</i> with active site in large subunit (red) and ironsulfur clusters in small subunit (blue) . . . . .	2
1.2	QM/MM optimized MBH structures of the proximal [Fe4S3] cluster structure for super-oxidized state and active site structure for Ni-B state in ball and stick representation; grey = carbon, blue = nitrogen, red = oxygen, white = hydrogen (only hydroxyl proton shown), yellow = sulphur, dark blue = nickel, green = iron	3
1.3	proposed mechanism includes a selection of all examined active site structures from the oxidized (top), reduced (middle) and illuminated (bottom) enzyme states	5
2.1	schematic overview of IR and Raman transitions; G = electronic ground state, R = electronic excited state; n,m,r = vibrational states . . . . .	9
3.1	overview of molecular mechanical potentials . . . . .	18
3.2	schematic example of the QM and MM region definitions of the hydrogenase protein solvated in water (light blue); the NiFe active site is the region of interest and therefore treated quantum mechanically . . . . .	21
3.3	schematic picture of the link atom scheme . . . . .	23
4.1	trigonal deformation of a six-membered ring; atoms 1, 3, 5 move inward while atoms 2, 4, and 6 move outward . . . . .	28
4.2	definition in the GVA input file “rexinp“ for the trigonal deformation of a six ring	28
4.3	GVA output file “assign“ for the vibrational spectrum of water . . . . .	29
4.4	steps in generating an Raman average spectrum from several MD/QM/MM structures . . . . .	33
4.5	stacked column representation for the $k$ 'th normal mode composition by individual internal coordinates; potential energy contributions are given in percent .	34
4.6	PEC weighted Raman intensities in comparison with unscaled averaged Raman spectrum and experimental resonance Raman spectrum . . . . .	35



# Abbreviations

DFT	Density Functional Theory
GGA	Generalized Gradient Approach
HF	Hartree-Fock
IR	Infrared
MBH	Membrane-bound Hydrogenase
MD	Molecular Dynamics
MM	Molecular Mechanics
NAD	Nicotinamide adenine dinucleotide
PEC	Potential energy contribution
PED	Potential energy distribution
PES	Potential energy surface
QM	Quantum Mechanics
QM/MM	Quantum Mechanics / Molecular Mechanics
RH	Regulatory Hydrogenase
RR	Resonance Raman
SCF	Self-consistent field
SH	Soluble Hydrogenase

# 1 The Hydrogenases from *Ralstonia eutropha*

## 1.1 Introduction

In 1931 the oxidation of molecular hydrogen was reported to be essential in the metabolism of autotrophic organisms by Stephenson and Stickland<sup>[46]</sup>. They characterized a specific enzyme responsible for the  $H_2 \rightleftharpoons 2H$  reaction which, according to the substrate that is metabolised, was named hydrogenase. In the following decades this enzyme gained significant attention given its particular potential in bioenergetic applications for clean fuel production<sup>[27]</sup>.

Hydrogenases are metalloenzymes which are classified by the composition of the active site where hydrogen processing takes place. There are three different types of active sites harbouring [NiFe], [FeFe], or [Fe] metal centres, respectively. In 1995 it was shown by x-ray and IR spectroscopic investigations that the [NiFe] and the [FeFe] centers carry inorganic, isoelectronic ligands which could not be attributed to the protein and whose vibrational signals exhibit shifts in the IR spectrum depending on the oxidation state of the enzyme<sup>[2,48,49]</sup>. For [NiFe] hydrogenases examined in this work, <sup>13</sup>C and <sup>15</sup>N labelling experiments revealed, the presence of three ligands, two  $CN^-$  and one  $CO$ , bound to the iron<sup>[13]</sup>. The bimetallic centre is attached to the protein via two bridged and two terminal cysteine amino acids (see figure 1.2).

Three hydrogenases with different tasks can be found in *Ralstonia eutropha*, named after their location in the cell. While regulatory hydrogenases (RH) sense the presence of hydrogen and regulate the expression of the hydrogenase gene, the soluble hydrogenase (SH) reduces  $NAD^+$ . They both are located in the cytoplasm. The membrane bound hydrogenase (MBH) serves as an electron donor in the respiratory chain and is located at the membrane of the cell, where it is anchored to the membrane lipids via a cytochrome B tail. It has the highest enzyme activity of the three hydrogenases and is able to work even at atmospheric levels of oxygen<sup>[41]</sup> which brought it into focus for biotechnological applications.

## 1.2 Structure

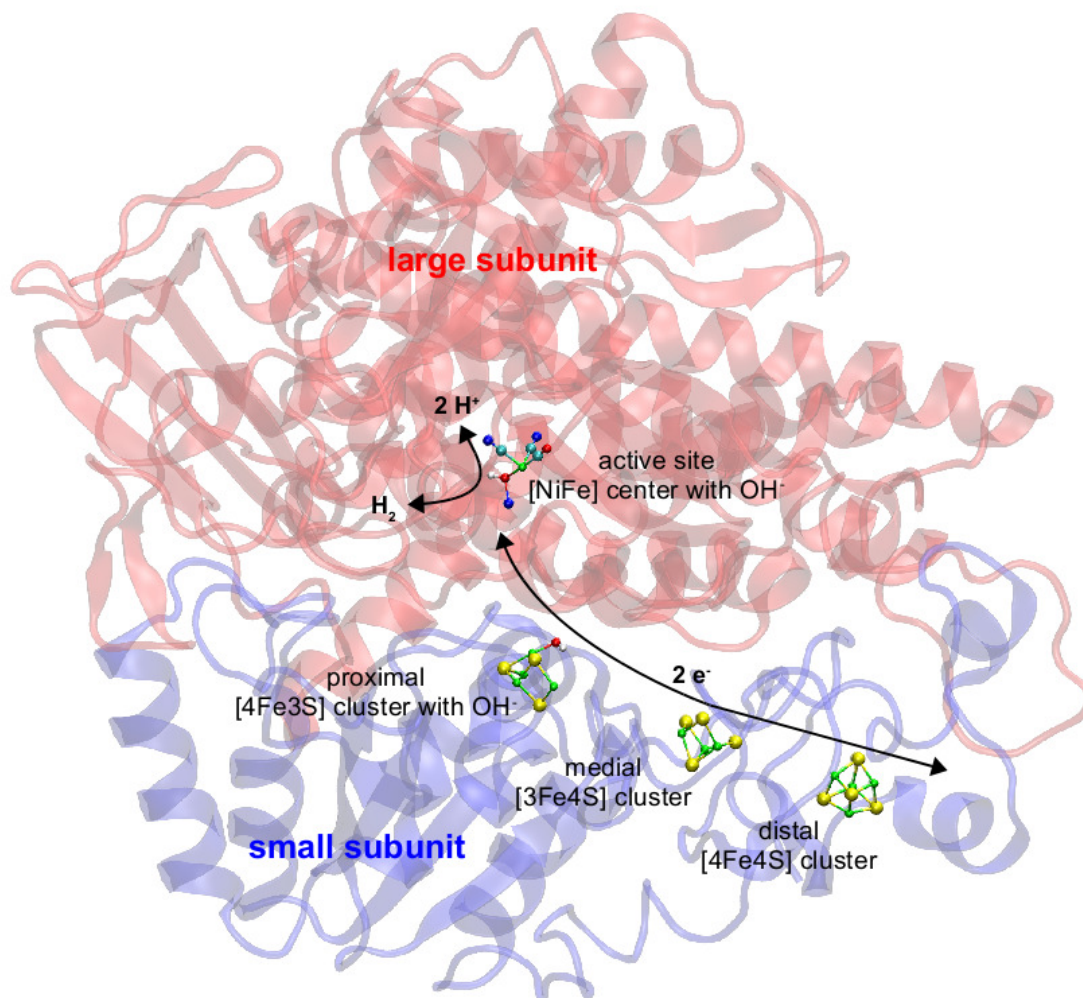


**Figure 1.1:** the dimeric membrane bound hydrogenase from *Ralstonia eutropha* with active site in large subunit (red) and iron-sulfur clusters in small subunit (blue)

The MBH consists of two subunits (see figure 1.1) and an additional to the cytochrome b tail. The [NiFe] active site is located in the large subunit. Electrons that are released during oxidation of molecular hydrogen are conducted to the cytochrome b tail via a chain of iron-sulfur clusters harboured in the small subunit<sup>[12]</sup>. An initial structural model was generated by Tillmann Utesch using the homology model and molecular dynamics methods.

The crystal structures of the enzyme from *Ralstonia eutropha* was solved by x-ray crystallography in 2011<sup>[11]</sup> for the reduced MBH and 2014 for the oxidized enzyme<sup>[9]</sup> and are the basis of calculations performed in this work.

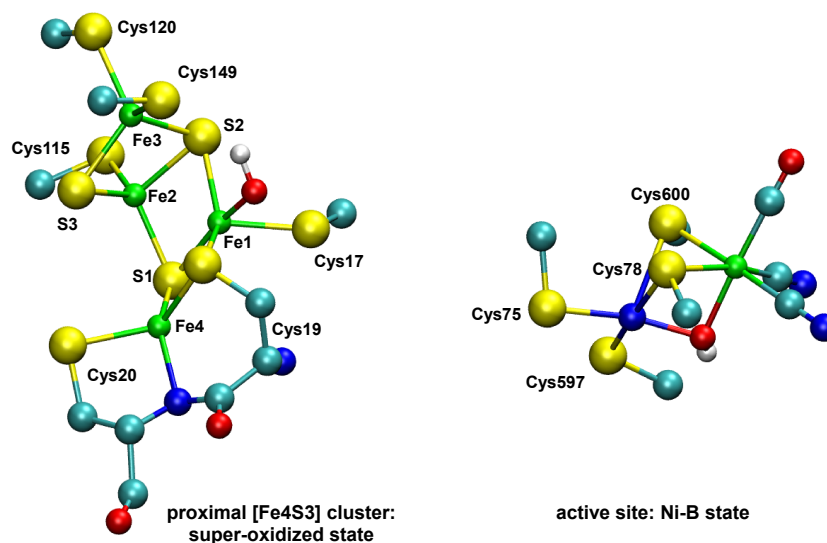


**Figure 1.2:** QM/MM optimized MBH structures of the proximal [Fe4S3] cluster structure for super-oxidized state and active site structure for Ni-B state in ball and stick representation; grey = carbon, blue = nitrogen, red = oxygen, white = hydrogen (only hydroxyl proton shown), yellow = sulphur, dark blue = nickel, green = iron

### 1.2.1 Active site structure

When exposed to oxygen, the MBH active site forms the Ni-B state (figure 1.2), which is referred to as one of the oxidized states of the MBH (see figure 1.3). Characteristic for this state is a hydroxyl ligand in the substrate binding site, which is the third bridging position between nickel, which is in oxidation state *III*, and iron, which remains always in oxidation state *II*<sup>[31]</sup>. Four deprotonated cysteine residues bind the bimetallic active site cluster to the protein: two (Cys78, Cys600) can be found in bridging positions between the metals and two (Cys75, Cys597) are bound to nickel in a terminal position.

The coordination pattern of nickel exhibits a square pyramidal geometry with a slight distortion to a see-saw geometry, which is considered to be important for efficient  $H_2$  binding and cleavage<sup>[7]</sup>. Furthermore, cysteine residue 597 is supposed to be part of a proton transfer pathway and indeed becomes protonated during the reaction cycle for the Ni-RS and the Ni-L state<sup>[5,44]</sup> (figure 1.3).

The iron atom remains in the oxidation state *II* throughout the complete reaction cycle. Ligated by six ligands its coordination sphere is octahedral. Apart from the two bridging cysteines and either the bound substrate or the hydroxyl ligand, there are two  $CN^-$  and one  $CO$  inorganic ligands which exhibit a strong ligand field. Hence, according to the Hund's rule all six d-orbital electrons of iron *II* are paired in the molecular orbitals model for octahedral geometry forming the low spin state.

The three inorganic ligands are arranged in such a way that the  $CO$  ligand is found in *trans* position to the binding site of the substrate (figure 1.2) and presumably influences the binding

energy of ligands in this *trans*-position<sup>[22]</sup>. The two  $CN^-$  ligands are involved in a complex hydrogen network with the protein environment. They are hydrogen bonded to threonine 553 and to arginine 530, respectively. The guanidine group of this Arg530 presumably also influences the binding of a substrate in the third bridging position as it is in close distance suitable for hydrogen bonding.

### 1.2.2 Proximal iron sulphur cluster

The *Ralstonia eutropha* MBH contains a proximal iron sulphur cluster which is structurally different compared to standard oxygen sensitive hydrogenases. The  $[Fe_4S_3]$  cluster which is attached to the protein via six cysteine residues<sup>[12]</sup> instead of four. Furthermore, during the oxidation of the protein a hydroxyl ligand is bound to one of the iron atoms (figure 1.2). The special geometry enables the protein to be reactivated within minutes after interaction with molecular oxygen at the active site<sup>[9,41]</sup>. Oxygen sensitive enzymes such as the  $[NiFe]$  hydrogenase from *Desulfovibrio vulgaris* Myazaki F have a standard  $[Fe_4S_4]$  cubane cluster in proximity to the catalytic centre. They also exhibit an additional state with an oxidized active site, the Ni-A state, which needs hours to be reactivated<sup>[41]</sup>.

The structure of the proximal  $[Fe_4S_3]$  cluster undergoes several changes during the oxidation of the protein, details of this process are still under discussion<sup>[9]</sup>. The enzyme exhibits redox-dependent transformations at Fe4 which, together with a reversible attachment of the hydroxyl ligand at Fe1, allow the cluster to release two electrons, which is one more compared to standard hydrogenases<sup>[9]</sup>.

In addition to the proximal cluster, two further iron sulphur cluster exist in medial and distal position to the catalytic centre (figure 1.1). They have standard like geometries, a  $[Fe_4S_3]$  medial and a  $[Fe_4S_4]$  distal cluster, and provide one electron each during the activation and reduction of the enzyme<sup>[23,26]</sup>.

## 1.3 Catalytic mechanism

The oxidized  $[NiFe]$  hydrogenase is denoted as inactive since the reactivation needs some time<sup>[41]</sup>. The oxygen tolerant MBH from *Ralstonia eutropha* resides in the Ni-B state, which is characterized by the presence of a hydroxyl ligand in the third bridging position between nickel in oxidation state *III* and iron in oxidation state *II*.

Under reducing conditions the *Ni(III)* takes up an electron and the  $OH^-$  ligand binds a proton, the  $Ni_r-S$  states in figure 1.3 are formed. By releasing a water molecule the catalytic centre turns active, in the  $Ni_a-S$  state the substrate binding site empty. Now the active site can bind molecular hydrogen and the enzyme cycles between the reduced states denoted as Ni-C and Ni-RS. Characteristic for the Ni-C is a hydride in the third bridging position. Most probably also the Ni-SR states carry a hydride in this position, but infrared spectroscopic investigations showed that several similar states exist that differ only slightly from each other<sup>[41]</sup>. During the turnover at the active site the hydrogen molecule is cleaved into two protons and two electrons.

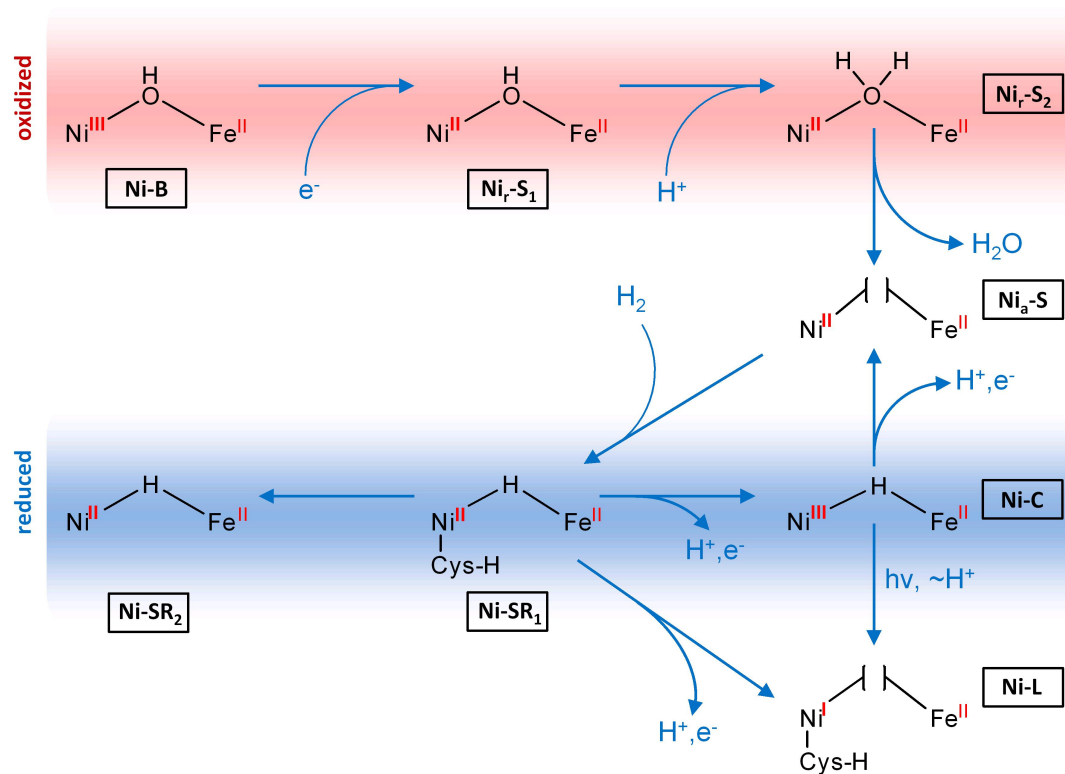


**Figure 1.3:** proposed mechanism includes a selection of all examined active site structures from the oxidized (top), reduced (middle) and illuminated (bottom) enzyme states

Figure 1.3 depicts an additional Ni-L state which was found to form upon irradiation of the reduced enzyme with visible light and is characterized by a  $Ni(I)$  and a protonated Cys597<sup>[44]</sup>.



## 2 Vibrational Spectroscopy

For a N-atomic nonlinear molecule  $3N$  degrees of freedom for translation, rotation and vibration exist. While there are 3 degrees of freedom for translation in every direction and 3 degrees of freedom for rotation along every axis in the 3-dimensional space,  $3N-6$  degrees of freedom remain for vibrational transitions. They are independent from each other and called normal modes, which can be described by normal coordinates  $Q_k$ . Normal modes of vibration can be induced with energies larger than 0.005 eV, corresponding to light with a wavelength in the infrared (IR) range. Vibrational transitions are excited by two different physical processes: the absorption of a photon carrying energy in the range of a vibrational transition and the inelastic scattering of photons with energies higher than the vibrational transition energy.

### 2.1 Infrared Spectroscopy

Infrared Spectroscopy (IR Spectroscopy) is a method where vibrations are probed by the absorption of a photon with the energy of a certain vibrational transition. The molecular system is irradiated with polychromatic light in the range of typical vibrational transitions, that is in the infrared region. To probe this physical mechanism of photon absorption, the vibrational transition and the corresponding normal coordinate  $Q_k$  has to be associated with a change of the dipole moment  $\mu$ . The intensity of such an IR absorption is expressed as

$$I_{IR} \propto \left| \frac{\partial \mu}{\partial Q_k} \right|^2. \quad (2.1)$$

The absorptions are detected either in a disperse setup, e. g. with a prism, where the absorption spectrum is directly probed by scanning through a wavelength range and measuring the intensity of the absorption. Or the molecule is irradiated at once with polychromatic light. In this case absorptions are recorded as interferograms which are Fourier-transformed to obtain the frequency-dependent absorption spectrum instead of the time dependent one.

The intensity of a vibrational transition is proportional to the transition probability  $P_{nm}$  from the vibrational level  $n$  to level  $m$ , which can be expressed quantum mechanically as

$$P_{nm} = \langle \Psi_m^* | \hat{\Omega} | \Psi_n \rangle. \quad (2.2)$$

$\Psi_m$  and  $\Psi_n$  are the wavefunctions of the initial and final vibrational states, respectively.  $\hat{\Omega}$  is the operator acting on the system and represents the perturbation resulting from the impact of electromagnetic radiation, which is the electrical dipole moment operator  $\hat{\mu}_q$  in the case of

photon absorption. After Taylor series expansion,  $\hat{\mu}_q$  can be written as

$$\hat{\mu}_q = \mu_q^0 + \sum_{k=1}^{3N-6} \left( \frac{\partial \mu_q}{\partial Q_k} \right)_0 Q_k \quad (2.3)$$

with  $Q_k$  being the normal coordinates. Combining equation 2.3 and equation 2.2, one obtains the expectation value for the transition dipole moment  $[\mu_q]_{nm}$

$$\begin{aligned} [\mu_q]_{nm} &= \langle \Psi_m^* | \hat{\mu}_q | \Psi_n \rangle \\ &= \mu_q^0 \langle \Psi_m^* | \Psi_n \rangle + \sum_{k=1}^{3N-6} \left( \frac{\partial \mu_q}{\partial Q_k} \right)_0 \langle \Psi_m^* | Q_k | \Psi_n \rangle. \end{aligned}$$

Since the wavefunctions  $\Psi_m$  and  $\Psi_n$  are orthogonal, the first term is zero, and the expectation value for the strength of the absorption simplifies to

$$[\mu_q]_{nm} = \sum_{k=1}^{3N-6} \left( \frac{\partial \mu_q}{\partial Q_k} \right)_0 \langle \Psi_m^* | Q_k | \Psi_n \rangle. \quad (2.4)$$

This equation is only non-zero, when the change of the dipole moment  $\mu_q$  with respect to the normal coordinate  $Q_k$  of the vibration is different from zero. The respective normal coordinate has to be associated with the vibrational quantum numbers  $m$  and  $n$  differing by 1.

## 2.2 Raman Spectroscopy

Raman spectroscopy is based on the inelastic scattering of photons with energy higher than the vibrational energy. The molecular system is irradiated with monochromatic light in the range of visible wavelength (400 - 750 nm). Most of the photons will be scattered elastically, this process is called Raylight scattering. A smaller amount of photons will be scattered inelastically and have energies reduced about the energy of a vibrational transition. This is the Stokes scattering, which is plotted relative to the incident light frequency. Also, excited vibrational states may relax to the vibrational ground state by the inelastic scattering resulting in a scattered photon of higher energy compared to the incident light, which is the Anti-Stokes scattering. A schematic overview for the different vibrational excitation processes is depicted in figure 2.1.

The occurrence and intensity of such vibrational transitions depend on the change of the polarisability  $\alpha$  with the molecules vibration  $Q_k$

$$I_{Raman} \propto \left| \frac{\partial \alpha}{\partial Q_k} \right|^2. \quad (2.5)$$

The incident radiation with frequency  $\nu_0$  is an oscillating electric field  $\vec{E}_0$ , which may induce a dipole  $\vec{\mu}_{ind}$  in the molecule depending on its polarisability  $\tilde{\alpha}$

$$\vec{\mu}_{ind} = \tilde{\alpha}(\nu) \cdot \vec{E}_0 \cos(2\pi\nu_0 t). \quad (2.6)$$

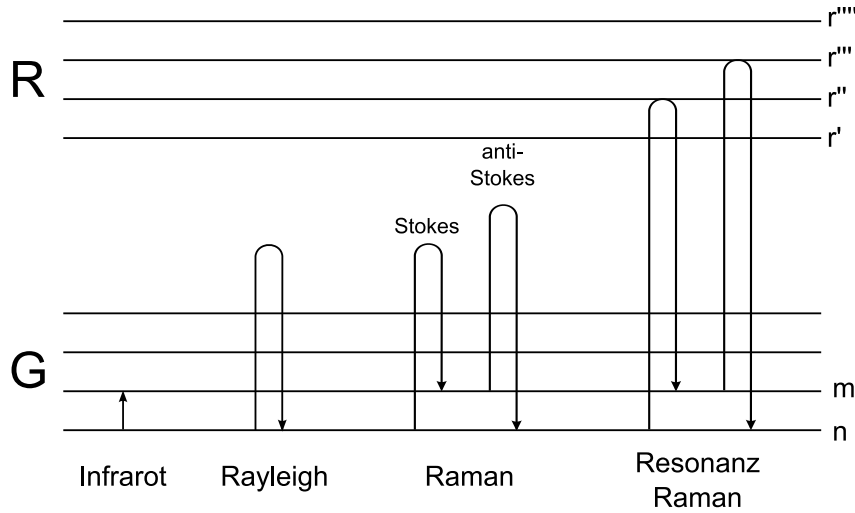


**Figure 2.1:** schematic overview of IR and Raman transitions; G = electronic ground state, R = electronic excited state; n,m,r = vibrational states

The intensity  $I_{mn}$  of a vibrational transition  $n \rightarrow m$  has to be described quantum mechanically by the transition probability according to equation 2.2. For the inelastic scattering of a photon the corresponding operator is the scattering polarisability tensor  $[\alpha_{\rho,\sigma}]_{mn}$  with  $\rho$  and  $\sigma = x, y, z$ . According to the dispersion theory of Kramers, Heisenberg and Dirac<sup>[20]</sup> the scattering polarisability tensor is given as

$$[\alpha_{\rho\sigma}]_{mn} = \frac{1}{\hbar} \sum_{R,r} \left( \frac{\langle mG | \mu_{\rho} | Rr \rangle \langle rR | \mu_{\sigma} | Gn \rangle}{\nu_{Rr} - \nu_{mn} - \nu_0 + i\Gamma_R} + \frac{\langle rR | \mu_{\sigma} | Gn \rangle \langle mG | \mu_{\rho} | Rr \rangle}{\nu_{Rr} - \nu_{mn} + \nu_0 + i\Gamma_R} \right) \quad (2.7)$$

with  $\mu_{\rho}$  and  $\mu_{\sigma}$  being the transition dipole moments in the corresponding  $x, y, z$  direction, the frequencies of a concerted electronic  $R$  and vibrational  $r$  transition  $\nu_{Rr}$ , of a pure  $n \rightarrow m$  vibrational transition  $\nu_{mn}$  and of the incident light  $\nu_0$ .  $G$  denotes the electronic ground state, whereas  $R$  refers to the excited electronic state.  $\Gamma_R$  is a damping constant which depends on the lifetime of the electronic transition state  $|R\rangle$ . Equation 2.7 describes the transition from the electronic and vibrational ground state to the excited state  $nG \rightarrow Rr$  and back  $rR \rightarrow Gm$  showing the dependency of a vibrational transition on all vibronic states.

**Resonance Raman enhancement** When the energy of the incident light  $h\nu_0$  is close to the energy of an electronic transition  $h\nu_{Rr}$ , or in other words, is in resonance with an electronic excited state, the first term in equation 2.7 increases. The value for the scattering polarisability tensor increases as well as the intensity of the vibrational transition that accompanies the electronic excitation. The vibrational transition is resonance enhanced. This effect is called the resonance Raman effect and is depicted in figure 2.1

For the resonance Raman effect the second term of equation 2.7 can then be neglected and

becomes

$$[\alpha_{\rho\sigma}]_{mn} = \frac{1}{\hbar} \sum_{R,r} \left( \frac{\langle nG|\mu_\rho|Rr\rangle \langle rR|\mu_\sigma|Gm\rangle}{\nu_{Rr} - \nu_{mn} - \nu_0 + i\Gamma_R} \right). \quad (2.8)$$

This relation depends on the electronic and nuclear coordinates. According to the Born-Oppenheimer approximation simplifications can be applied

$$\begin{aligned} \langle nG|\mu_\rho|Rr\rangle &= \langle nr\rangle \langle G|\mu_\rho|R\rangle = \langle nr\rangle \mu_{GR,\rho} \\ \langle rR|\mu_\sigma|Gm\rangle &= \langle rm\rangle \langle R|\mu_\sigma|G\rangle = \langle rm\rangle \mu_{GR,\sigma} \end{aligned}$$

and equation 2.8 becomes

$$[\alpha_{\rho\sigma}]_{mn} = \frac{1}{\hbar} \sum_{R,r} \left( \frac{\langle nr\rangle \langle rm\rangle \mu_{GR,\rho} \mu_{GR,\sigma}}{\nu_{Rr} - \nu_{mn} - \nu_0 + i\Gamma_R} \right). \quad (2.9)$$

The integrals  $\langle nr\rangle$  and  $\langle rm\rangle$  represent the Franck-Condon factors. They are the integrals over the products of the vibrational wavefunctions of the electronic ground  $n$  and  $m$  states and excited states  $r$ . They reflect the transition probability between two vibrational states and thus significantly influences the intensity of the resonance enhancement. The more the vibrational wavefunctions have the same symmetry or the stronger they overlap, the closer the Franck-Condon factor is to one. The less they overlap the closer the factor is to zero.

After Taylor series expansion with respect to the normal coordinates  $Q_k$ , the scattering polarisability tensor for the resonance enhancement can be expressed with the Albrecht terms  $A$  and  $B$  as

$$[\alpha_{\rho\sigma}]_{mn} = A_{\rho\sigma} + B_{\rho\sigma} \quad (2.10)$$

with

$$A_{\rho\sigma} = \frac{1}{\hbar} \sum_r \left( \frac{\langle nr\rangle \langle rm\rangle \mu_{GR,\rho}^0 \mu_{GR,\sigma}^0}{\nu_{Rr} - \nu_{mn} - \nu_0 + i\Gamma_R} \right) \quad (2.11)$$

and

$$B_{\rho\sigma} = \frac{1}{\hbar} \sum_r \left( \frac{\langle n|Q_k|r\rangle \langle rm\rangle \left( \frac{\partial \mu_{GR,\rho}^0}{\partial Q_k} \right)_0 \mu_{GR,\sigma}^0}{\nu_{Rr} - \nu_{mn} - \nu_0 + i\Gamma_R} \right) + \left( \frac{\langle nr\rangle \langle r|Q_k|m\rangle \left( \frac{\partial \mu_{GR,\sigma}^0}{\partial Q_k} \right)_0 \mu_{GR,\rho}^0}{\nu_{Rr} - \nu_{mn} - \nu_0 + i\Gamma_R} \right). \quad (2.12)$$

The larger the transition dipole moment  $\mu_{GR}$  the more dominant the A-term gets over the B-term. The enhancement then significantly depends on the overlap integral or the Franck-Condon factor of the vibrational wavefunctions as they go down as a product  $\langle nr\rangle \langle rm\rangle$  instead of a sum as in the B-term. When the electronic state is displaced relative to the ground state along an internal coordinate of the corresponding normal coordinate  $Q_k$ , than the integrals  $\langle nr\rangle$

and  $\langle rm \rangle$  are not overlapping completely and hence smaller than one but non-zero and the resonance enhancement increases. The electronic excited states are displaced when for instance electronic transitions occur into anti-bonding orbitals or charge is being transferred along with the excitation.

The B-term will gain dominance the more the electronic transition dipole moment changes along with the corresponding normal coordinate  $Q_k$ . This vibronic coupling enhancement may also increase the resonance Raman intensity even in the case of a weak resonant electronic transition.



# 3 Theoretical Background

## 3.1 Quantum Mechanics

Quantum mechanics are based on the Schrödinger Equation

$$\hat{H}\Psi_i = E_i\Psi_i. \quad (3.1)$$

$\Psi_i$  is the wave function of the system in state  $i$  and  $E_i$  is the respective energy.  $\hat{H}$  is the Hamiltonian, which, for the time independent case, is written as

$$\hat{H} = \hat{T}_N + \hat{T}_e + \hat{V}_{NN} + \hat{V}_{Ne} + \hat{V}_{ee}. \quad (3.2)$$

$\hat{T}_N$  and  $\hat{T}_e$  are operators for the kinetic energy of the nuclei and the electrons, respectively.  $\hat{V}_{NN}$ ,  $\hat{V}_{Ne}$  and  $\hat{V}_{ee}$  are operators for the potential energy of repulsive and attractive electrostatic interactions between the nuclei, the electrons and between each other.

Since nuclei of atoms have much more mass than the electrons, they move very slow compared to electrons. This is the basis of the Born Oppenheimer approximation where the positions of the nuclei are considered fixed. In this way the kinetic energy  $\hat{T}_N$  is zero and the potential energy of the nucleus-nucleus repulsion  $\hat{V}_{NN}$  stays constant. The Hamiltonian simplifies to

$$\hat{H} = \hat{T}_e + \hat{V}_{Ne} + \hat{V}_{ee} \quad (3.3)$$

$$= -\frac{\hbar}{2m_e}\nabla_i^2 - \sum_i \frac{Z_i e^2}{4\pi\epsilon_0 r_i} + \frac{1}{2} \sum_{i \neq j} \frac{e^2}{4\pi\epsilon_0 r_{ij}}. \quad (3.4)$$

In eq. 3.4  $\nabla_i^2$  is the Nabla Operator representing the differentiation with respect to the nuclei and electron coordinates in the Cartesian system,  $Z$  is the effective nuclear charge,  $e$  the elementary charge,  $\epsilon_0$  the vacuum permittivity,  $r_i$  the nucleus-electron distance and  $r_{ij}$  the distance between two electrons  $i$  and  $j$ , respectively. The potential energy  $\hat{V}_{NN}$  is added to the energy calculated by means of the electronic Schrödinger equation to obtain the total energy of the system.

### 3.1.1 Hartree Fock Method

An analytical solution of the electronic Schrödinger equation is only possible for a very small number of nuclei and electrons due to complicated interactions of all electrons with each other. Therefore the electronic Schrödinger equation must be solved numerically by different approx-

imation methods.

One approximation method is the Hartree-Fock-method named after their developers Douglas Rayner Hartree and Wladimir Alexandrowitsch Fock. Instead of using one wave function  $\Psi_0$  that depends on  $N$  electrons, they introduced the so called Slater-determinant  $\Xi_{SD}$ . The Slater-determinant is an asymmetrized product of  $N$  one-electron wave functions  $\chi_i(\vec{x}_i)$

$$\Psi_0 \approx \Xi_{SD} = \frac{1}{\sqrt{N!}} \begin{vmatrix} \chi_1(\vec{x}_1) & \chi_2(\vec{x}_1) & \cdots & \chi_N(\vec{x}_1) \\ \chi_1(\vec{x}_2) & \chi_2(\vec{x}_2) & \cdots & \chi_N(\vec{x}_2) \\ \vdots & \vdots & & \vdots \\ \chi_1(\vec{x}_N) & \chi_2(\vec{x}_N) & \cdots & \chi_N(\vec{x}_N) \end{vmatrix}. \quad (3.5)$$

These one-electron wave functions or spin orbitals  $\chi_i(\vec{x}_i)$  are composed of a spatial orbital for the electron and the information about its spin state ( $\alpha \uparrow$  or  $\beta \downarrow$ ) in the form of a spin function  $\sigma_i$ . The spatial orbital can be expressed as linear combination of the individual atomic orbitals. The Hartree Fock equation for a spin orbital  $\chi_i(\vec{x}_i)$  of an electron at the place  $\vec{x}_i$  is written as

$$\hat{f}_{i,HF} \chi_i(\vec{x}_i) = \varepsilon_i \chi_i(\vec{x}_i). \quad (3.6)$$

where  $\varepsilon_i$  is the energy for the considered orbital,  $\hat{f}_{i,HF}$  is the corresponding Fock operator<sup>[17]</sup>, which is defined as

$$\hat{f}_{i,HF} = \hat{h}_i + \sum_j^N (\hat{J}_j(\vec{x}_i) - \hat{K}_j(\vec{x}_i)). \quad (3.7)$$

It comprises three operators.  $\hat{h}_i$  is the Hamiltonian without the operator for the potential energy of the electron electron repulsion. This energy is included in the Coulomb operator  $\hat{J}_j$  for the individual spin orbital  $\chi_j(\vec{x}_i)$  and is applied for all spin orbitals. It is written in the following form:

$$\hat{J}_j(\vec{x}_i) \chi_i(\vec{x}_i) = \int |\chi_j(\vec{x}_2)|^2 \frac{Z_i e^2}{4\pi\epsilon_0 r_{12}} d(\vec{x}_2) \chi_i(\vec{x}_i). \quad (3.8)$$

Hence, the potential energy also depends on the probability  $|\chi_j(\vec{x}_2)|^2$  that an electron is located at  $\vec{x}_i$  in the spin orbital  $\chi_j$ . The exchange operator  $\hat{K}_j$  corrects the fact, that the Slater determinant is not antisymmetric in terms of the exchange of spin orbitals. It is defined as

$$\hat{K}_j(\vec{x}_i) \chi_i(\vec{x}_i) = \int \chi_j(\vec{x}_2) \frac{Z_i e^2}{4\pi\epsilon_0 r_{12}} \chi_i(\vec{x}_2) d(\vec{x}_2) \chi_i(\vec{x}_i). \quad (3.9)$$

All spin orbitals are orthonormal, so the contribution of the exchange energy becomes zero for electrons of opposite spin. Only in the case of two electrons with same spin the contribution is non-zero. But electrons of opposite spin are also not allowed to come too close to each other because of their charge. The Hartree Fock method neglects this so-called Coulomb correlation energy.

The Fock operator depends on all orbitals. An equation with such an operator can only be solved numerically, starting with an approximated expression of the orbitals. The Hartree Fock equation is then being solved for all spin orbitals  $\chi_i$ . This leads to an improved set of orbitals, which serve as starting point for a new iteration when solving the Hartree Fock equations with a new total energy. This procedure is repeated until the orbitals and the energy are constant within certain convergence criteria. This method is called self consistent field procedure (SCF). Orbitals obtained in this way are self-consistent.

Also the wave function written as the Slater determinant  $\Phi_{SD}$  is only an approximation to the exact one. Hence, the calculated energy  $|E^{HF}|$  is because of the variational principle always smaller than the real total energy  $|E_0|$  because of the variational principle. The difference is called correlation energy  $|E_C^{HF}|$

$$|E_0| - |E^{HF}| = |E_C^{HF}|. \quad (3.10)$$

### 3.1.2 Density Functional Theory

For systems with more atoms and even more electrons, in particular biological systems as analysed in this work, the Hartree Fock method becomes computationally expensive since it depends on  $4N$  variables ( $3N$  spatial and  $N$  spin variables). An alternative approach to calculate the total energy and other electronic properties of a molecular system has been developed by W. Kohn and L. J. Sham in 1965<sup>[18]</sup>. The density functional theory (DFT) introduces a Kohn-Sham operator that includes functions depending on the electron density  $\rho$ .

In analogy to the Hartree-Fock method a Slater determinant  $\Phi_{SD}$  is constructed, consisting of  $N$  Kohn-Sham orbitals  $\varphi_i$ :

$$\Psi_0 \approx \Phi_{SD} = \frac{1}{\sqrt{N!}} \begin{vmatrix} \varphi_1(\vec{x}_1) & \varphi_2(\vec{x}_1) & \cdots & \varphi_N(\vec{x}_1) \\ \varphi_1(\vec{x}_2) & \varphi_2(\vec{x}_2) & \cdots & \varphi_N(\vec{x}_2) \\ \vdots & \vdots & & \vdots \\ \varphi_1(\vec{x}_N) & \varphi_2(\vec{x}_N) & \cdots & \varphi_N(\vec{x}_N) \end{vmatrix}. \quad (3.11)$$

In contrast to the Hartree-Fock method these orbitals describe  $N$  non-interacting one-electron wave functions. The Kohn-Sham equation for one of the Kohn-Sham orbitals  $\varphi_i$  is written as

$$\hat{f}_{i,KS} \varphi_i(x_i) = \varepsilon_i \varphi_i(x_i) \quad (3.12)$$

with  $\hat{f}_{i,KS}$  being the one-electron Kohn-Sham operator, which consist of two terms:

$$\hat{f}_{i,KS} = \hat{T} + \hat{V}_{\text{eff},i}. \quad (3.13)$$

Due to the assumption of non interacting one-electron orbitals it is now possible to express the kinetic energy  $\hat{T}$  exactly as

$$\hat{T} = -\frac{\hbar^2}{2m_e} \nabla_i^2. \quad (3.14)$$

The effective potential  $\hat{V}_{\text{eff},i}$  connects the ideal non-interacting system and the real system with interacting electrons. It includes the Coulomb repulsion potential between two electrons  $\hat{V}_{ee}$ , the attractive interaction potential between nuclei and electrons  $\hat{V}_{Ne}$  (also external potential), and the exchange-correlation potential  $\hat{V}_{XC}$

$$\hat{V}_{\text{eff}} = \hat{V}_{ee} + \hat{V}_{Ne} + \hat{V}_{XC}. \quad (3.15)$$

Another important difference to the Hartree Fock method is the energy dependency on the electron density  $\rho$ . The effective potential becomes

$$\hat{V}_{\text{eff}} = \int \frac{\rho(r_j)}{|r_i - r_j|} dr_j + \hat{V}_{Ne} + \frac{\delta E_{XC}}{\delta \rho}. \quad (3.16)$$

The electron density is accessible via the sum of the squares of the Kohn-Sham orbitals  $\varphi_i$

$$\rho(r) = \sum_i^N |\varphi_i(r)|^2. \quad (3.17)$$

Hence, the effective potential depends on the electron density and consequently on each Kohn-Sham orbital  $\varphi_i$ . Like in the Hartree-Fock method the solution is only accessible in a self consistent way.

The development of accurate approximations and descriptions of the exchange correlation functional  $E_{XC}$  is the key target of the density functional theory, as the neglected contributions to the total energy are summed in this potential, e. g. self-interaction correction, exchange and correlation of the electron movements, which is the part of the kinetic energy, that is neglected by the assumption of non-interacting fermions. The latter contribution is completely neglected in the Hartree-Fock method. The better the approximation for this exchange correlation functional, the closer to the real ground state total energy is the energy calculated by the Kohn-Sham Approach would be .

Practically the exchange correlation functional  $E_{XC}$  is separated into an exchange and a correlation functional and there exist various approaches to describe them. Commonly used methods are the gradient corrected electron densities (**Generalized Gradient Approximation**) or the usage of the exact exchange energy from the Hartree Fock approach mixed into the DFT energy by applying empirical parameters.

The BP86 functional, applied to the biological system in this work, represents a GGA functional. It combines of the Becke88<sup>[3]</sup> correlation functional and the Perdew86 functional<sup>[33]</sup> for the exchange energy and is a so-called pure functional, which is well suited for metal containing molecular systems like the MBH studied in this work.

A popular example for a hybrid functional is the B3LYP functional. It combines the correlation functional Becke88<sup>[3]</sup> and the exchange functional LYP from Lee, Yang and Parr<sup>[25]</sup>. The 3 in B3LYP indicates the number of parameters used to mix the exact exchange energy obtained by the Hartree Fock method with the exchange energy computed with the DFT method.

## 3.2 Molecular Mechanics

Methods based on quantum mechanics are very accurate but are limited to quite small systems as they become computationally very expensive for larger systems such as enzymes, proteins and polymers. In these cases force field methods are more suitable approaches as electrons are ignored and energies are calculated only depending on the positions of the nuclei of the system which is possible because of the Born-Oppenheimer approximation. Molecular mechanics uses classical mechanics to describe simple interactions like the bond stretching, the angle bending or the dihedral torsion. Parameters developed for smaller systems can also be applied to similar larger systems. Among others, frequently used force fields are for example CHARMM (which is applied in this work), AMBER and GROMOS<sup>[8,43]</sup>.

### 3.2.1 Classical Force Fields

A simple expression for the composition of a force field to calculate the potential energy  $V$  as a function of the positions  $r$  of a  $N$  atomic system is

$$\begin{aligned}
 V(r^N) = & \sum_{bonds} \frac{k_i}{2} (l_i - l_{i,0})^2 \\
 & + \sum_{angles} \frac{k_i}{2} (\theta_i - \theta_{i,0})^2 \\
 & + \sum_{torsions} \frac{V_n}{2} (1 + \cos(n\chi - \gamma)) \\
 & + \sum_{improper} \frac{k_i}{2} (\omega_i - \omega_{i,0})^2 \\
 & + \sum_{i=1}^N \sum_{j=i+1}^N \left( 4\epsilon_{ij} \left[ \left( \frac{\sigma_{ij}}{r_{ij}} \right)^{12} - \left( \frac{\sigma_{ij}}{r_{ij}} \right)^6 \right] + \frac{q_i q_j}{4\pi\epsilon_0 r_{ij}} \right).
 \end{aligned}$$

The first term is the harmonic potential for bond interactions, which increases if the bond length  $l_i$  deviates from the referenced, empirical parameter  $l_{i,0}$  for this individual bond. The second term, again modelled by a harmonic potential, gives the energy for the angles of the  $N$  atomic system, when the angle  $\theta_i$  between three connected atoms deviates from a reference value. The third term describes the energy for a torsion around a dihedral bond by the Pitzer potential<sup>[35]</sup>. Alternative descriptions for the potential energy of a torsion motion exist<sup>[6]</sup>. The fourth term sums up over all energies arising from improper motions (or out of plane motions) again represented by a harmonic potential. The last term comprises the nonbonded

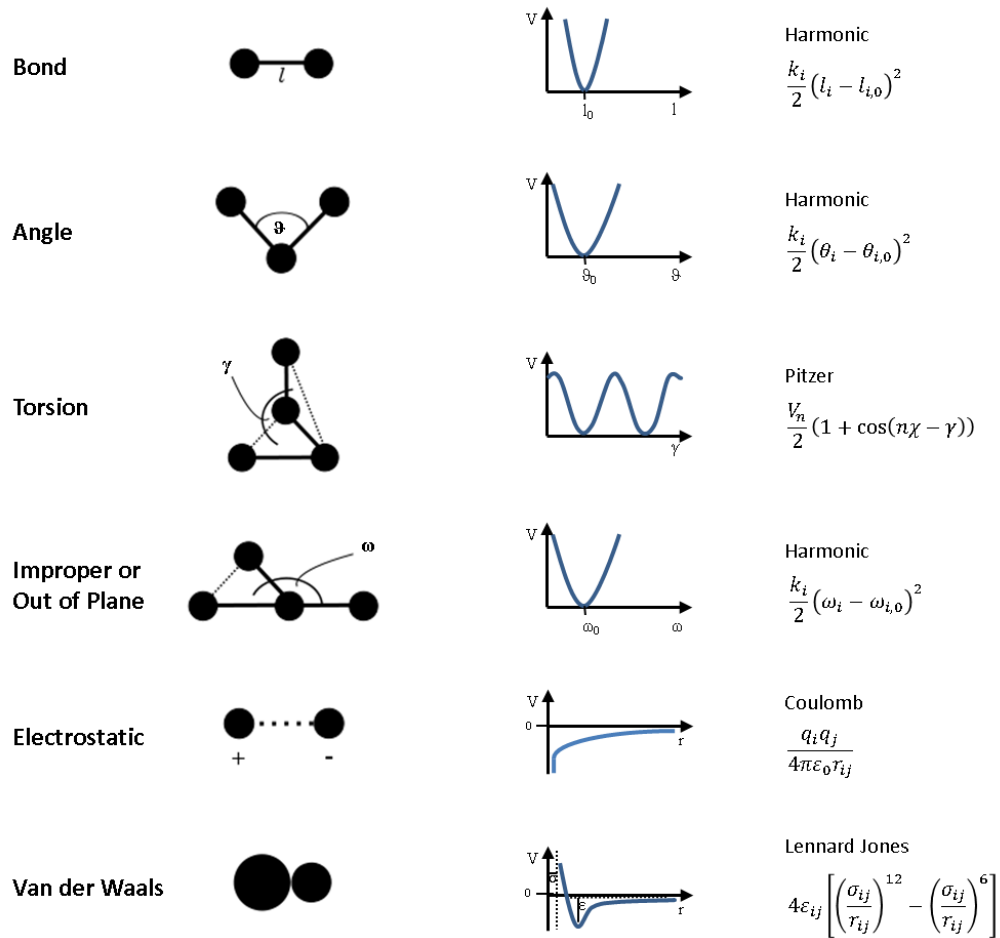


**Figure 3.1:** overview of molecular mechanical potentials

electrostatic and van der Waals interactions. The electrostatic interactions are usually modelled by a Coulomb potential, whereas the van der Waals interactions are described by a Lennard Jones potential. An overview of all interactions and potentials is depicted in figure 3.1.

### 3.2.2 Molecular Dynamics Simulation

To obtain thermodynamic properties of a system a statistic ensemble of the structure is required. One method for producing this structure ensemble is the Monte Carlo method. Replicants are generated randomly from the first structure. Well defined criteria (such as the Boltzmann factor) decide about the probability of existence for the new structure. The Monte Carlo method is a stochastic method. A major disadvantage is the missing time dependency.

In a second method -molecular dynamics simulations- replications are obtained by solving the differential equations from Newtons laws of motion

$$\frac{d^2 x_i}{dt^2} = \frac{F_{x_i}}{m_i} \quad (3.18)$$

with the force  $F$  on particle  $i$  in  $x$  direction and the mass  $m_i$ . This method is deterministic, meaning that the structure at any future time can be determined from the initial one. An analytical solution is not possible for an N-body system. However, a solution can be achieved by applying a finite difference method which is done by dividing the calculation into very small timesteps ( $10^{-15} - 10^{-14}$ s). There are different algorithms to calculate the positions and forces for the next timestep by combining forces, accelerations and positions from current and previous timesteps. The force is assumed to be constant during a timestep. The most commonly used algorithms are the Verlet, Velocity Verlet and the Leap Frog Method, shortly explained in the following.

In the Verlet method for the current timestep  $t$  positions  $x(t)$  and forces  $f(t)$  or accelerations  $a(t)$ , are available. To predict the atom positions for the next timestep  $t + \delta t$  the positions from the previous timestep  $t - \delta t$  are required, as shown in the following:

$$x(t + \delta t) = x(t) + \delta t v(t) + \frac{1}{2} \delta t^2 a(t) + \dots \quad (3.19)$$

$$x(t - \delta t) = x(t) - \delta t v(t) + \frac{1}{2} \delta t^2 a(t) - \dots \quad (3.20)$$

The combination of these two relations yields

$$x(t + \delta t) = 2x(t) - x(t - \delta t) + \delta t^2 a(t). \quad (3.21)$$

From the new positions  $x(t + \delta t)$  the new forces and accelerations can be calculated, and a new calculation cycle starts. Drawbacks are, the missing velocity, and the necessity to include positions from the previous step into the calculation. Thus, approximations need to be applied to guess the positions  $x(0 - \delta t)$  of the initial step.

In the velocity Verlet method<sup>[47]</sup> positions, forces and velocities the time  $(t + \delta t)$  are calculated in three steps. First, the velocity at a half timestep

$$v(t + \frac{1}{2} \delta t) = v(t) + \frac{1}{2} \delta t a(t) \quad (3.22)$$

with the current velocity and accelerations at time  $t$ . In the following step this half timestep velocity is used to calculate the new positions

$$x(t + \delta t) = x(t) + \delta t v(t) + \frac{1}{2} \delta t^2 a(t) \quad (3.23)$$

$$= x(t) + v(t + \frac{1}{2} \delta t) \delta t \quad (3.24)$$

from which the accelerations  $a(t + \delta t)$  (and forces, respectively) can be computed with the applied force field. The velocities for the next timestep are then determined in the third step

$$v(t + \delta t) = v(t) + \frac{1}{2} \delta t a(t) + \frac{1}{2} \delta t a(t + \delta t) \quad (3.25)$$

$$= v(t + \frac{1}{2} \delta t) + \frac{1}{2} \delta t a(t + \delta t) \quad (3.26)$$

The Leap Frog algorithm<sup>[16]</sup> makes use of half timesteps  $t + \frac{1}{2} \delta t$  as well. It computes the positions  $x(t + \delta t)$  for the next timestep by using the last half timestep of the velocities  $v(t -$

$\frac{1}{2}\delta t$ ). Because the velocities are not calculated at the actual timestep but are always half shifted, this method appears to have leap-frog character which is the reason for the algorithm's name. Velocities and positions are determined according to

$$x(t + \delta t) = x(t) + \delta t v(t + \frac{1}{2}\delta t) \quad (3.27)$$

$$v(t + \frac{1}{2}\delta t) = v(t - \frac{1}{2}\delta t) + \delta t a(t). \quad (3.28)$$

### Boundaries

Simulations over time are describing less molecules compared to real conditions. The average number of molecules in a molecular simulation is about 1000 to 1500 molecules including the solvent. As a consequence interactions with the boundaries of a molecular simulation setup are influencing the properties and hence lead to different results that do not correspond to reality when not handled by certain boundary conditions.

One solution is the definition of periodic boundary conditions. In the simplest way the system of interest is set up in a cubic box of solvent particles. This box is then replicated in every direction. The cubic box will have 6 face, 12 edge and 8 corner neighbouring replicated cubic boxes. A particle leaving the box on one side will enter the replicated box on the opposite site retaining all its properties. Beside the cubic box other cell symmetries such as the hexagonal prism or the rhombic dodecahedron exist. For all periodic cells it is important to define a solvent buffer zone that is large enough to prevent the replicated centre molecules from interacting with each other.

## 3.3 The combination of Quantum and Molecular Mechanics

A large system can be partitioned in at least two regions, one is treated quantum mechanically (QM) while the other one is treated with molecular mechanics (MM). For the study of structural, electronic and vibrational properties of a smaller part in a large system such as the active site of a protein, the combination of all advantages from quantum mechanics and from molecular mechanics is an efficient calculation method with respect to computation times. The quantum mechanical (QM) treated region is embedded in the molecular mechanically treated environment. This leads to more realistic results since the system is considered as a whole but only the interesting part of it is treated with quantum mechanics.

### 3.3.1 QM/MM partition

In a QM/MM calculation different regions have to be defined. First the region of interest, which should be treated quantum mechanically has to be identified. Often this QM region is the co-factor in an enzyme. The QM region is embedded in the MM region which is described by molecular mechanics. As the QM region is only influenced by nearby atoms, the surrounding MM region is defined up to a distance of usually 15 to 20 Å while the remaining outer part of

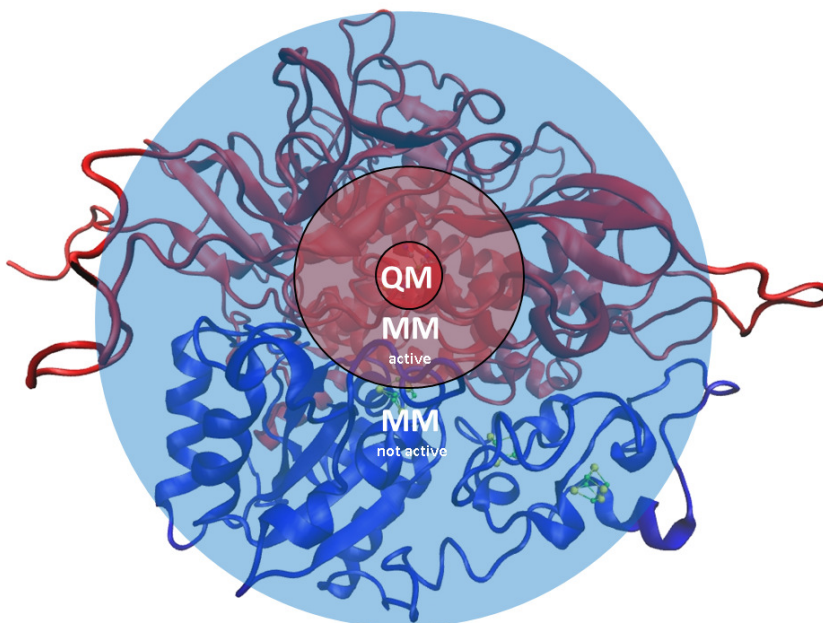


**Figure 3.2:** schematic example of the QM and MM region definitions of the hydrogenase protein solvated in water (light blue); the NiFe active site is the region of interest and therefore treated quantum mechanically

the system is not treated at all. Figure 3.2 shows a schematic example of the definition of the different regions in the hydrogenase protein.

### 3.3.2 Energy of the QM/MM system

Two schemes exist to compute energies within the QM/MM framework. One way to compute the total energy is the subtractive scheme (see equation 3.29). The energy for the total system is calculated on a molecular mechanical level and the energy for the QM region is added. Afterwards the energy for the QM region calculated on the molecular mechanical level is subtracted in order to avoid the double counting of the of the QM region energy:

$$E_{tot} = E_{MM}^{wholesystem} + E_{QM} - E_{MM}^{QMregion} \quad (3.29)$$

A major disadvantage of this approach is that MM parameters for the QM region need to be assigned. This can be difficult as many active sites or cofactors of a protein have an individual structure or include metals for which no empirical parameters exist yet. A further drawback is that the interaction between the QM region and the MM region is treated at MM level, which can lead to larger errors in the energy calculation.

Another and more frequently used scheme is the additional scheme, where an explicit coupling

term is added to the MM energy and the QM energy to calculate the total energy of the system

$$E_{tot} = E_{MM} + E_{QM} + E_{QM/MM}. \quad (3.30)$$

This coupling energy  $E_{QM/MM}$  accounts for electrostatic, van der Waals and bonded interactions at the boundary between QM and MM region

$$E_{QM/MM} = E_{QM/MM}^{el} + E_{QM/MM}^{vdW} + E_{QM/MM}^b. \quad (3.31)$$

**Electrostatic interactions** The first term in equation 3.31 is the electrostatic interaction between the QM and the MM region and can be assessed via several approaches, such as the mechanical embedding method, the electrostatic embedding or the polarized embedding scheme. In the mechanical embedding method, predefined point charges for QM atoms are used to calculate electrostatic interactions at MM level. One disadvantage is the static definition of the QM point charges which may change along a reaction path. Furthermore, these point charges accessed easily.

The electrostatic embedding of the QM region into a cloud of point charges representing the MM region is a frequently applied method. MM point charges are then included as one electron terms in the QM Hamiltonian. However, the MM charge distribution near the boundary region is not polarized by the QM region which is a drawback of this method.

The third method is called the polarized embedding scheme and overcomes this disadvantage. Several approaches exist to obtain a polarized MM charge distribution. One way is to calculate the charges of the MM atoms at the QM/MM boundary region quantum mechanically in the presence of the QM part. The new charges are then updated in the respective parameter and topology input files. Another way is a fully self-consistent definition where the polarizable MM model is integrated into the QM Hamiltonian. Charges act in both directions, from the MM region onto the QM region and vice versa.

**van der Waals interactions** The treatment of the short range van der Waals interactions is similar to the MM treatment, where the Lennard-Jones Potential is applied (see figure 3.1). The atoms of the QM part are described by parameters from related atom types from the MM part, and the energy is then calculated at MM level. Errors arising from van der Waals parameters that are not suitable for the individual QM atoms are one of this method's drawbacks. As van der Waals interactions are short range, these errors might be reduced by modifying the QM/MM boundary region to be more distant from the site of interest.

**bonded interactions** If the boundary region cuts through a covalent bond, interactions from the bonded parts count for the coupling energy. There are a few approaches on how to handle these covalent bonds cuts such as the localized-orbital scheme, where hybrid orbitals are placed at the border between the two subsystems. They simulate a saturated bond and are kept fix during the calculations.

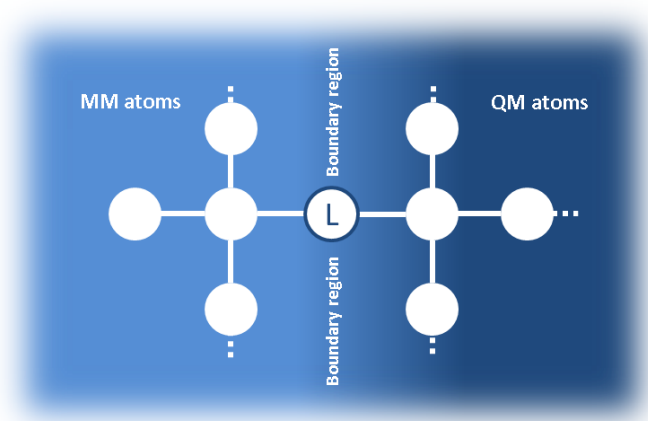


**Figure 3.3:** schematic picture of the link atom scheme

A further method is the boundary atom scheme, where the first atom of the MM part appear in the QM calculation to mimic a saturated bond. In the MM calculation it appears as a normal MM atom.

The third method is the link atom scheme which will be discussed in more detail as it has been used in this work. This method introduces an additional atom - the link atom - to saturate the broken covalent bond (see figure 3.3). Normally this is a hydrogen atom. The QM part is complete without any free bonds, and QM calculations can be performed. For calculations on the MM region, the link atom is omitted and the covalent bond between the boundary MM atom and the boundary QM atom is treated molecular mechanically. However, the presence of an additional atom causes errors such as overpolarization as a result of the close proximity to the MM boundary atom. In addition artificial additional degrees of freedom as well as a wrong chemical representation of the link atom lead to erroneous properties which have to be considered and removed, in particular when vibrational properties have to be calculated. This is achieved by correcting the Hessian matrix, which contains all force constants from the QM calculation (see section 4.1).

The corrected Hessian matrix  $H_{cor}$  is the Hessian of the QM fragment corrected for the QM/MM coupling and contains the second derivatives of the total energies  $E_{tot}$  with respect to the QM displacements  $r_{QM}$

$$\begin{aligned}
 H_{cor} &= \frac{\partial^2 E_{tot}}{\partial r^2} \\
 &= \frac{\partial^2}{\partial r^2} \left( E_{QM} + E_{QM/MM}^{el} + E_{QM/MM}^{vdW} + E_{QM/MM}^b + E_{QM/MM}^{link} \right) \\
 &= \frac{\partial^2}{\partial r^2} \left( E'_{QM} + E_{QM/MM}^{vdW} + E_{QM/MM}^b + E_{QM/MM}^{link} \right).
 \end{aligned}$$

Since the frequency calculation is performed in the presence of the point charges of the MM region according to the electrostatic embedding model, the QM charges are polarized by these point charges. Therefore the electrostatic interaction energy  $E_{QM/MM}^{el}$  is included in the energy

of the QM part  $E'_{QM}$ . The former equation can be further simplified as the second derivative of the QM energies in the presence of MM point charges  $E'_{QM}$  is the Hessian matrix  $H'_{QM}$  directly calculated by any quantum chemical computer package such as TURBOMOLE or GAUSSIAN09<sup>[1,10]</sup>

$$H_{cor} = H'_{QM} + \frac{\partial^2}{\partial r^2} \left( E_{QM/MM}^{vdW} + E_{QM/MM}^b + E_{QM/MM}^{link} \right). \quad (3.32)$$

Furthermore, the correction for additional link atoms is included in the Hessian matrix  $H_{QM/MM}^{link}$

$$H_{cor} = H'_{QM} + \frac{\partial^2}{\partial r^2} \left( E_{QM/MM}^{vdW} + E_{QM/MM}^b \right) + H_{QM/MM}^{link}. \quad (3.33)$$

Given that forces  $F^q(link)$  resulting from the link atom  $l$  only affect the directly bonded QM atom  $q$ , the correction for additional link atoms can be written as

$$\begin{aligned} H_{QM/MM}^{link} &= \frac{\partial F_i^q(link)}{\partial r_k^q} \\ &= \sum_j \alpha_{jk}^{q-l} \frac{\partial r_j^l}{\partial r_i^q} + \sum_j F_j^l \frac{\partial^2 r_j^l}{\partial r_k^q \partial r_i^q} \end{aligned}$$

with  $i, j$  and  $k$  being the indices running over all cartesian coordinates  $x, y$  and  $z$ , respectively, and  $\alpha_{jk}^{q-l}$  being the elements of the quantum mechanical Hessian matrix that describe the coupling between the link atom  $l$  bonded to the QM atom  $q$ <sup>[28]</sup>. In a next step the dimension of the Hessian matrix is reduced by removing the artificial degrees of freedom due to the additional link atoms by neglecting the coupling from the link atoms with other QM atoms that are not directly bonded to the link atom. This correction approach also neglects non-bonded interactions resulting from the different link bond compared to the real bond in the QM/MM system. Corrections terms for van der Waals and bonding interactions in eq. 3.33 are calculated analytically, based on the force field (e. g. CHARMM<sup>[6]</sup>) for the molecular mechanical region.

## 4 Data Analysis

### 4.1 Normal Mode Analysis

The following section is an introduction to normal mode analysis. It is mainly based on the books Wilson “Molecular Vibrations: The Theory of Infrared and Raman Vibrational Spectra”<sup>[51]</sup> and Siebert and Hildebrandt “Vibrational Spectroscopy in Life Science”<sup>[15]</sup>.

#### 4.1.1 Normal modes

When a molecule with  $N$  atoms is exposed to any form of energy it starts moving. It has  $3N$  degrees of freedom to move, this includes translational, rotational and vibrational movements. Taking into account only vibrations, three translational and three rotational (two in case of a linear molecule) degrees of freedom need to be subtracted resulting in  $3N - 6$  ( $3N - 5$ ) independent -or orthogonal in mathematical terms- vibrational motions, the normal modes. A normal mode is the concerted motion of all atoms with the same frequency, but with different amplitudes. The center of mass does not shift.

Molecular orbital structure optimizations provide a molecular structure with all atoms in a position of minimal potential energy. For example, the first derivative of the potential energy  $V$  with respect to the position of atom  $i$  in  $x$  direction is zero. Atom  $i$  is in its equilibrium position. The second derivative with respect to the  $x$  direction gives the force constant  $f_{x_i x_j}$ . It represents the change of the force in  $x$  direction when moving atom  $i$  in  $x$  direction.

$$\frac{\partial^2 V}{\partial x^2} = f_{x_i x_j} \quad (4.1)$$

From this example one can see that these force constants do not represent the force constants for individual bonds. Each atom is affected by the motion of all other atoms in the molecule via attractive and repulsive forces. This leads to  $3N \times 3N$  force constants  $f$  which can be written into the Hessian matrix  $\mathbf{F}$

$$\mathbf{F} = \begin{matrix} & 1 & \dots & N \\ \begin{matrix} 1 \\ \vdots \\ N \end{matrix} & \begin{pmatrix} \boxed{f_{11}} & & \boxed{f_{1N}} \\ & \ddots & \\ \boxed{f_{N1}} & & \boxed{f_{NN}} \end{pmatrix} \end{matrix} \quad (4.2)$$

with

$$\boxed{f_{11}} = \begin{pmatrix} f_{x_1x_1} & f_{x_1y_1} & f_{x_1z_1} \\ f_{y_1x_1} & f_{y_1y_1} & f_{y_1z_1} \\ f_{z_1x_1} & f_{z_1y_1} & f_{z_1z_1} \end{pmatrix}. \quad (4.3)$$

According to Hookes Law, the force  $F$  to restore a system that has been displaced about the distance  $x$  with respect to the initial position is

$$F = -fx. \quad (4.4)$$

where  $f$  is the force constant of the spring. Combination with Newtons Law of motion

$$F = ma. \quad (4.5)$$

with the mass  $m$  times its acceleration  $a$  yields

$$-fx = ma \quad (4.6)$$

$$0 = a + \frac{f}{m}x. \quad (4.7)$$

The acceleration  $a$  is the change of velocity with time, and the velocity is the change of distance  $x$  with time

$$0 = \frac{d^2x}{dt^2} + \frac{f}{m}x. \quad (4.8)$$

The first term on the right site represents the change of the kinetic energy  $T$  and the second the change of the potential energy  $V$ . Equation 4.8 is an ordinary differential equation. Assuming harmonic motion the solution for the displacement  $x$  with time is given by

$$x(t) = A \sin(2\pi vt). \quad (4.9)$$

$A$  is the amplitude of the motion and  $v$  is the frequency. The second derivative of equation 4.9

$$\begin{aligned} \frac{d^2x}{dt^2} &= -4\pi^2 v^2 \cdot A \sin(2\pi vt) \\ &= -4\pi^2 v^2 \cdot x \end{aligned}$$

is substituted to equation 4.8 to yield

$$0 = -4\pi^2 v^2 x + \frac{f}{m}x. \quad (4.10)$$

This equation can then be applied to all atoms and force constants in all directions x,y and z of the cartesian coordinates space which leads to 3N linearly dependent equations

$$\begin{aligned}
 -4\pi^2 v^2 \cdot m_1 x_1 &= -f_{x_1 x_1} x_1 - f_{x_1 y_1} y_1 - f_{x_1 z_1} z_1 \cdots - f_{x_1 x_N} x_N - f_{x_1 y_N} y_N - f_{x_1 z_N} z_N \\
 -4\pi^2 v^2 \cdot m_1 y_1 &= -f_{y_1 x_1} x_1 - f_{y_1 y_1} y_1 - f_{y_1 z_1} z_1 \cdots - f_{y_1 x_N} x_N - f_{y_1 y_N} y_N - f_{y_1 z_N} z_N \\
 -4\pi^2 v^2 \cdot m_1 z_1 &= -f_{z_1 x_1} x_1 - f_{z_1 y_1} y_1 - f_{z_1 z_1} z_1 \cdots - f_{z_1 x_N} x_N - f_{z_1 y_N} y_N - f_{z_1 z_N} z_N \\
 -4\pi^2 v^2 \cdot m_2 x_2 &= -f_{x_2 x_1} x_1 - f_{x_2 y_1} y_1 - f_{x_2 z_1} z_1 \cdots - f_{x_2 x_N} x_N - f_{x_2 y_N} y_N - f_{x_2 z_N} z_N \\
 &\vdots \\
 -4\pi^2 v^2 \cdot m_N z_N &= -f_{z_N x_1} x_1 - f_{z_N y_1} y_1 - f_{z_N z_1} z_1 \cdots - f_{z_N x_N} x_N - f_{z_N y_N} y_N - f_{z_N z_N} z_N
 \end{aligned}$$

Expressed in matrix form we obtain

$$-4\pi^2 v^2 \cdot \mathbf{m}_\alpha \cdot \mathbf{x}_{ij} \cdot \mathbf{y}_{ij} \cdot \mathbf{z}_{ij} = -\mathbf{F} \cdot \mathbf{x}_{ij} \cdot \mathbf{y}_{ij} \cdot \mathbf{z}_{ij} \quad (4.11)$$

with  $m_\alpha$  being the mass of atom  $\alpha$  and  $x_{ij}$ ,  $y_{ij}$  and  $z_{ij}$  being the displacements in the cartesian coordinate space. One can simplify equation 4.11 can be simplified by introducing mass-weighted cartesian displacement coordinates  $q_{ij}$  and force constants  $f_{ij}$

$$q_i = \sqrt{m_\alpha} \cdot x_i. \quad (4.12)$$

The expression 4.11 then has the following form

$$-4\pi^2 v^2 \cdot \mathbf{q}_{ij} = -\mathbf{f}_{ij} \cdot \mathbf{q}_{ij} \quad (4.13)$$

with the massweighted Hessian matrix  $\mathbf{f}_{ij}$ . This is an eigenvalue eigenvector equation that can be solved by many algorithms, leading to 3N solutions for  $\mathbf{v}$ . The eigenvalues represent the vibrations of the N atomic molecule which must be zero for the included translational and rotational motions. The eigenvectors represent the movements of the molecule in normal coordinates  $Q_k$  for each normal mode  $k$ .

### 4.1.2 Internal Coordinates

For large molecules, normal modes and normal coordinates are no longer illustrative for the description of a vibration. It becomes more useful to define internal coordinates  $S$ . Motions are described by changes in the internal configurations such as bond stretching, angle bending, torsions of dihedrals and out of plane motions. Moreover, the six (five in linear case) motions of rotation and translation that equal zero can be eliminated. The resulting set of  $t = 3N - 6$  ( $t = 3N - 5$ ) internal coordinates  $S_t$  are defined as

$$S_t = \sum_{\alpha=1}^N \vec{s}_{t\alpha} \cdot \vec{p}_\alpha. \quad (4.14)$$

In equation 4.14,  $\vec{\rho}_\alpha$  represents the displacement vector for atom  $\alpha$  along the three axes of the cartesian coordinate system.  $\vec{s}_{i\alpha}$  is a vector that characterizes the internal motion of atom  $\alpha$ . For the internal coordinate describing a bond stretching,  $\vec{s}_{i\alpha}$  is parallel to this bond. It is always chosen such that the increase of  $S_i$  is maximal.

The 3N-6 internal coordinates  $S_i$  are independent from each other. With a more complex

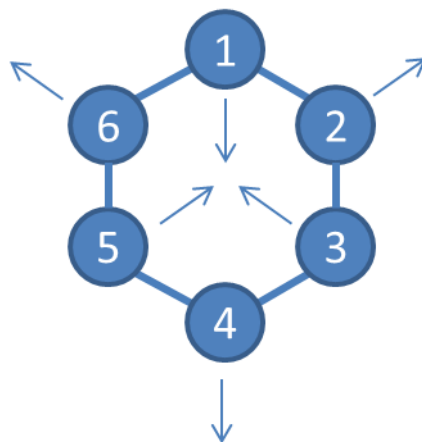


**Figure 4.1:** trigonal deformation of a six-membered ring; atoms 1, 3, 5 move inward while atoms 2, 4, and 6 move outward

system, also the definition of these coordinates gets more complicated. One has to consider symmetry and their concerted complex normal mode, which include more than four atoms at once. A good example for such a case is a six-ring. It exhibits at a certain energy a trigonal deformation mode, three atoms of the ring move outside while the other three move inside at the same time (see figure 4.1). This normal mode has a trigonal symmetry. The internal coordinate to describe this movement includes now six bending angles with different linear combination coefficients. Figure 4.2 represents the definition of such an internal coordinate for the normal mode analysis program GVA according to Pulay et al.<sup>[37]</sup>

So far, internal coordinates are independent from the masses of atoms involved in the movement. They are introduced in the G-Matrix. An element of the symmetric 3N-6 (3N-5 in linear

```
# definitions of internal coordinates
# >>>>>>> DIMENSION OF INTERNAL COORDINATE SPACE IS 3N-6! <<<<<<<<

#   type  index list      coflc      cnorm      c5ring      no.  fdiag
...
# TRIGONAL DEFORMATION 6-ring
k  bend  1  5  6  0      -1.00000000    0.00000000    0.00000000    x
    bend  6  4  5  0       1.00000000    0.00000000    0.00000000
    bend  5  3  4  0      -1.00000000    0.00000000    0.00000000
    bend  4  2  3  0       1.00000000    0.00000000    0.00000000
    bend  3  1  2  0      -1.00000000    0.00000000    0.00000000
    bend  2  6  1  0       1.00000000    0.00000000    0.00000000
...
*
```

**Figure 4.2:** definition in the GVA input file “rexinp“ for the trigonal deformation of a six ring

	calc. [cm-1]	exp. [cm-1]	IRint [km/mol]	Rint (rel.)	contribution
1	3849.32	-----	19.38	44.00	( 50.00%) ( 1)STRETCHING O-H1 ( 50.00%) ( 2)STRETCHING O-H2
2	3727.46	-----	1.69	100.00	( 49.96%) ( 1)STRETCHING O-H1 ( 49.96%) ( 2)STRETCHING O-H2
3	1713.16	-----	75.79	74.16	( 99.91%) ( 3)BENDING H-O-H

**Figure 4.3:** GVA output file “assign” for the vibrational spectrum of water

molecule case) G-matrix is defined as

$$G_{tt'} = \sum_{\alpha=1}^N \frac{1}{m_{\alpha}} \vec{s}_{t\alpha} \cdot \vec{s}_{t'\alpha}. \quad (4.15)$$

When expressed in internal coordinates the kinetic energy becomes

$$T = \frac{1}{2} \sum_{tt'} (G^{-1})_{tt'} \dot{S}_t \dot{S}'_t \quad (4.16)$$

and the potential energy

$$V = \frac{1}{2} \sum_{tt'} F_{tt'} \dot{S}_t \dot{S}'_t. \quad (4.17)$$

Newtons equations of motion lead to the solution

$$s_t = A_t \sin(2\pi\nu t). \quad (4.18)$$

The 3N-6 linear dependent equations can be expressed with matrix formalism as

$$|F - (G^{-1})4\pi^2\nu^2| = 0 \quad (4.19)$$

which is the  $FG$  matrix with  $t$  (3N-6 or 3N-5) solutions for  $\nu$ . Now one can compute the relative amplitudes of each internal coordinate  $A_t$  normalized to the potential energy given in equation 4.17. The contribution of the potential energy of every internal coordinate  $i$  to a normal mode is called the PED of a normal mode (potential energy distribution),

$$[PED]_{ij} = L_{ik} L_{ki}^{-1} \quad (4.20)$$

where  $L_{ij}$  represents the transformation matrix between normal coordinate  $k$  and internal coordinate  $i$ . An example generated from the program GVA is represented in figure 4.3.

Together with the description of normal modes in internal coordinates, the analysis of the normal modes of a complex molecule becomes illustrative and intuitiv. Using dipole moment and polarizability derivatives also infrared and relative Raman intensities are obtained with GVA.

## 4.2 Resonance Raman Approach

As explained in section 2.2, the Raman effect does not only depend on ground states properties but also on electronically excited states.

Under non-resonance conditions the Raman intensity  $I_Q$  for a normal mode  $Q$ , the frequency  $\nu_Q$  and the excitation frequency  $\nu_0$  can be computed according to the following equation<sup>[36]</sup>

$$I \propto \left(45(\alpha')^2 + 7(\gamma')^2\right) \frac{(\nu_0 - \nu_Q)^4}{\nu_Q \left(1 - \exp\left(-\frac{h\nu}{kT}\right)\right)}. \quad (4.21)$$

where  $\alpha'$  and  $\gamma'$  are the derivatives of the polarisability tensor and of the corresponding anisotropy, respectively with respect to the normal mode  $Q$ . Equation 4.21 is implemented in GVA<sup>[10]</sup> which reads the Hessian matrix (eq. 4.2),  $\alpha'$  and  $\gamma'$  from the output files of a quantum chemical calculation program such as GAUSSIAN or TURBOMOLE<sup>[1,10]</sup>.

**Calculation of resonance Raman intensities** Under resonant conditions the effect of vibronic coupling cannot be neglected. Several approaches to compute resonance Raman (RR) intensities exist which depend on the excited state displacement<sup>[50]</sup> (see section 2.2).

One method is the time dependent formalism developed by Heller et al.<sup>[14]</sup>. It depends on the time evolution after a vertical electronic transition. The semiempirical approach involves finding the local harmonic parameters on the excited state potential energy surface (PES) in order to calculate the excited state displacement  $\Delta_{GR}$  which is determined from the partial derivative of the electronic excited state energy  $E_R$  according to

$$\Delta_{GR} \approx -\frac{1}{\nu_k^2} \left( \frac{\partial E_R}{\partial Q_k} \right)_0 \quad (4.22)$$

where  $\nu_k$  is the vibrational frequency of the normal coordinate  $Q_k$  in the electronic ground state. The method developed by Peticolas and Rush<sup>[34]</sup> is an alternative approach to calculate resonance Raman intensities and includes the practical application of the Kramer Kronig transform theory<sup>[19,21]</sup> and is the combination of experiment and theory. The RR intensity  $I_k$  of a resonance enhanced normal mode  $Q_k$  with the frequency  $\nu_k$  is given by

$$I_k(\nu_0) = K \cdot \mu_{GR}^4 \cdot \frac{\Delta_k^2}{2} |\Omega(\nu_0) - \Omega(\nu_0 - \nu_k)|^2 \quad (4.23)$$

with  $\nu_0$  being the frequency of the incident light and the transition dipole moment of the electronic transition  $\mu_{GR}$ . The factor  $K$  is defined<sup>[40]</sup> as

$$K = \nu_0(\nu_0 - \nu_k)^3 \cdot \left( \frac{\sqrt{\nu_k}}{5.8065} \right)^2. \quad (4.24)$$

The frequency dependence of the scattering polarisability tensor  $\alpha$  in the A term in equation 2.11 can be obtained by measuring the electronic absorption curve by means of UV-vis

spectroscopy and the Kramers-Kronig relations. The electronic transition dipole moment  $\mu_{GR}$  and the excited state displacements  $\Delta_{GR}$  can be calculated quantum mechanically. Therefore electronic ground state and excited state geometry calculations are necessary, which are non-trivial. Furthermore, these calculations can only be performed for a single electronic transition. Calculation of excited state properties is very computationally demanding and constitutes a considerable drawback of these approaches.

**PEC weighted Raman intensities** To avoid this step, the *potential energy contribution (PEC) weighted Raman intensities approach* was developed. Calculated Raman intensities are scaled by the potential energy contribution (see section 4.1) of selected internal coordinates.

Depending on the wavelength of the laser light in a RR experiment one has to identify the electronic transition that can be responsible for the RR effect. Based on this transition a set of  $N$  internal coordinates that are affected by the electronic transition is chosen. The potential energy distribution, or in other words the composition of every normal mode is inspected. For modes that contain PEC of one or more of the selected internal coordinates, frequencies and Raman intensities are extracted with their corresponding PEC. In order to simulate resonance Raman intensities the calculated Raman intensity  $I_{calc,k}$  of the  $k$ 'th normal mode is rescaled according to

$$I_{scaled,k} = I_{calc,k} \cdot \left( \frac{\sum_{i=1}^N (1 + PEC_i)^2}{N} \right) \quad (4.25)$$

with  $N$  being the number of involved internal coordinates.

Table 4.1 shows an example of three normal modes  $k$  with the individual contribution of each internal coordinate to the corresponding potential energy distribution (PED). The internal co-

**Table 4.1:** simple example of the PEDs of the  $k$ 'th normal mode and its internal coordinate PEC

<b>k</b>	<b>1</b>		<b>2</b>		<b>3</b>	
	<b>int. coord.</b>	<b>PEC</b>	<b>int. coord.</b>	<b>PEC</b>	<b>int. coord.</b>	<b>PEC</b>
PED	IC a	5.00%	IC a	8.00%	IC a	6.00%
	IC b	10.00%	IC b	20.00%	IC b	15.00%
	IC c	8.00%	IC e	6.00%	IC d	12.00%
	IC d	9.00%	IC f	7.00%	IC f	7.00%

ordinates c and d have been assigned to the set of coordinates that are most likely affected by resonance enhancement, the corresponding entries are marked in blue. Hence, frequencies, Raman intensities and PECs of the chosen internal coordinates of normal mode  $k = 1$  and 3 would be extracted and rescaled, whereas normal mode  $k = 2$  would be neglected.

In addition to the advantageous combination of molecular dynamic simulations and QM/MM calculations a modified instantaneous normal mode analysis<sup>[29]</sup> is applied to obtain an averaged spectrum from an ensemble of slightly different structures and vibrational spectra.

To calculate the average spectrum it is necessary to group the normal modes by careful inspection as they are composed by quite complex movements of the cofactor. Intensity, frequency and mode composition have to be considered in a certain range. With lower frequency of a considered normal mode, the vibration gets more complex. In other words the description by individual internal coordinates becomes very complex. Hence, unambiguous identification of a specific normal mode is difficult, in particular in the low frequency region of a vibrational spectrum. As a consequence close lying but different normal modes with similar intensities might be averaged and distort the results. However, the benefit of including structural dynamics in the spectral data clearly compensates this drawback, especially when normal modes are clearly distinguishable.

**Application to MBH** Figure 4.4 depicts the results for each subsequent step of treating the calculated Raman spectra with the PEC weighted Raman intensities approach (from top to bottom).

An untreated Raman spectrum obtained by QM/MM calculation on the [NiFe] active site of the MBH and a corresponding experimental resonance Raman spectrum are shown in figure 4.4 A<sup>[45]</sup>. As the QM part of the structure optimized with QM/MM also included amino acid residues of the protein environment surrounding the active site, the corresponding vibrations contribute to the calculated spectrum. They may lead to erroneous assignments with the experimental bands of vibration.

The next step was the identification of internal coordinates that should contribute to the resonance enhancement. The experimental RR data (grey) was measured with an incident wavelength of 568 nm which lies in the energy range for metal to ligand charge transfers. Inspecting the structure of the [NiFe] active site, the Fe and the *CO* and *CN*<sup>-</sup> molecular orbitals with very similar energy levels are likely candidates for the metal to ligand charge transfer. Thus, normal modes involving vibrations of these atoms should be resonance enhanced. Accordingly, all normal modes without any contribution of the stretchings  $\nu(Fe - CO)$ ,  $\nu(Fe - CN)$  or bendings  $\delta(Fe - C - O)$ ,  $\delta(Fe - C - N)$  were omitted since their intensities are very small compared to the resonance enhanced vibrational modes. The resulting spectrum is depicted in the figure 4.4 B.

The Raman spectrum is computed for multiple “snapshots” of a MD simulation, i. e. for slightly different geometry optimized structures of the protein environment and the active site. In the next step, the processing described above was applied to all Raman spectra obtained by the combined MD simulation and QM/MM calculation approach. The resulting spectra are plotted figure 4.4 C. One spectrum -marked in red- exhibits large deviations in peak positions and intensities and was treated as an outlier, meaning that it was excluded from subsequent data treatment.

In the last step all individual Raman spectra were averaged as depicted in figure 4.4 D. This treatment integrates the dynamic fluctuations of the molecular structure into a single vibrational

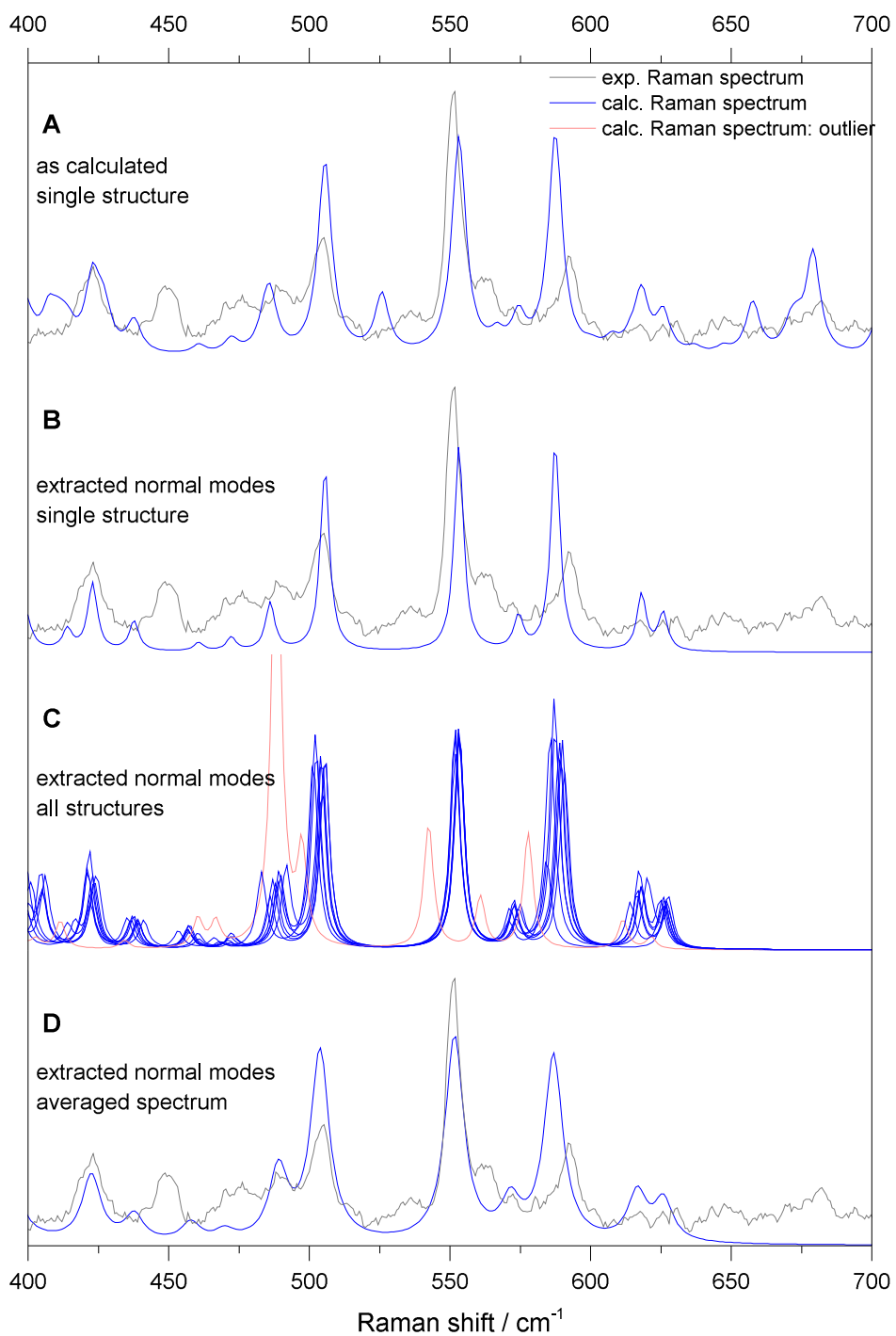


**Figure 4.4:** steps in generating a Raman average spectrum from several MD/QM/MM structures

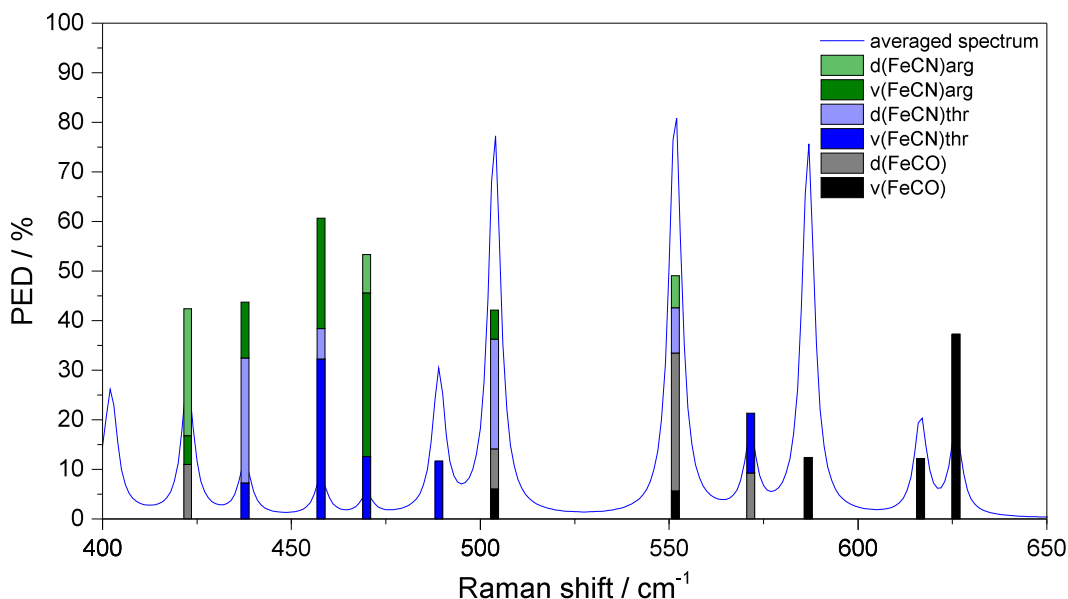


**Figure 4.5:** stacked column representation for the  $k$ 'th normal mode composition by individual internal coordinates; potential energy contributions are given in percent

spectrum, which corresponds much better to the real situation of the molecule and strongly justifies the comparison with experimental data. It emphasizes the importance of having more than one structure to compare with the experiment. An assignment to the outlier spectrum only would have led to the opinion, that the underlying model for the calculation is wrong. This is not true, when considering the results for other structures of the MD simulation trajectory of the same model.

Finally, the last step as explained in detail in the previous subsection 4.2 was applied to account for the individual resonance enhancement of the normal modes. Since the Raman spectrum is an average, also the PEC of the selected internal coordinates from each calculated Raman spectrum were averaged. Figure 4.5 shows the averaged but yet unweighted calculated Raman spectrum together with the averaged PECs of each internal coordinate that contains  $Fe - CO$  and  $Fe - CN$  vibrations and thus should experience resonance enhancement. For the active site of the hydrogenase the  $Fe - CO$  moiety seems to be involved in a vibronic excitation in particular. The iron is coordinated in an octahedral pattern, thus the d-orbitals split into three orbitals of  $t_{2g}$ -symmetry and two of  $e_g$ -symmetry. The  $CO$  and  $CN^-$  ligands exhibit a strong ligand field, thus, the six d-electrons occupy the  $t_{2g}$  orbitals forming the low spin species. The energy of the unoccupied  $\pi^*$  molecular orbitals of the  $CO$  and  $CN^-$  ligands is very close to these occupied  $t_{2g}$  orbitals of the iron, strong  $\pi$ -backbonding occurs. For incident light with the energy of this electronic  $\pi \rightarrow \pi^*$  transition into the anti-bonding molecular orbitals of the  $CO$  ligand,

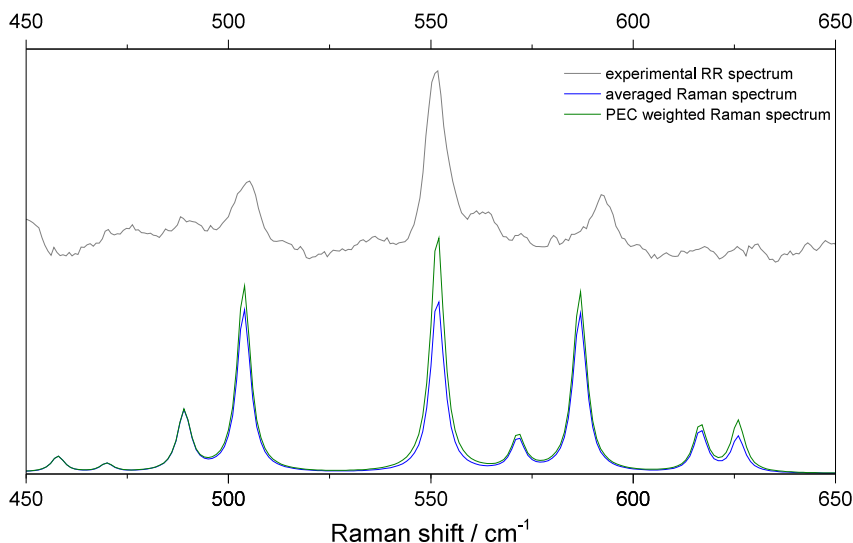


**Figure 4.6:** PEC weighted Raman intensities in comparison with unscaled averaged Raman spectrum and experimental resonance Raman spectrum

this excitation will be accompanied by a change in the bond properties and hence lead to a displacement of the electronic excited state along a normal mode  $k$  which has contributions of this bond. The product of the Franck-Condon factors in the A-term in equation 2.10 will turn non-zero and the resonance enhancement increases. Compared to the  $CN^-$  ligands, the energy level of the anti-bonding  $\pi^*$  molecular orbital of the  $CO$  ligand is closer to the occupied  $t_{2g}$  orbitals of the iron. Therefore, internal coordinates containing the stretching  $\nu(Fe - CO)$  and bending  $\delta(Fe - C - O)$  were used to weight the Raman intensities. Accordingly, equation 4.25 becomes

$$I_{scaled,k} = I_{calc,k} \cdot \left( \frac{(1 + PEC_{\nu})^2 + (1 + PEC_{\delta})^2}{2} \right). \quad (4.26)$$

and is applied to all normal modes. For modes without contributions of these internal coordinates  $I_{scaled}$  equals  $I_{calc}$ . The resulting PEC weighted Raman intensities are plotted in figure 4.6 and also summarized in table 4.2.

### 4.3 Correlation Analysis

The combination of MD simulations and QM/MM calculations does not only yield an averaged vibrational spectrum that corresponds better to real conditions. It also produces sets of structural information, variation of charges and varying frequencies for every normal mode. These data can be analysed for connections and dependencies and in this way indicate relations

**Table 4.2:** Overview of the calculated averaged wavenumbers and Raman intensities for the  $k$  normal modes with corresponding standard deviation  $\sigma$  and their scaled Raman intensities

$\text{cm}^{-1}_k$	$\sigma$	$I_k$	$\sigma$	$I_{k,\text{PEC weighted}}$
626	2	4,19	1	6,04
617	3	4,95	2	5,59
587	4	18,88	5	21,37
572	4	3,78	1	4,15
552	4	20,78	3	28,57
504	2	19,34	2	22,17
489	4	7,18	1	7,18
470	2	1,02	1	1,02
458	2	1,90	1	1,90
438	2	2,66	1	2,66
423	1	6,73	2	7,51
402	4	5,96	1	5,96

between properties, that where not obvious at first sight. To quantify these connections, correlation analysis of the gained data is the first choice.

A very common method to quantify the linear relation of two data sets  $x$  and  $y$  with  $n$  elements is the Pearson correlation  $\rho_{xy}$

$$\rho_{xy} = \frac{\sum_{k=1}^n (x_i - \bar{x})(y_i - \bar{y})}{\sqrt{\sum_{k=1}^n (x_i - \bar{x})^2} \sqrt{\sum_{k=1}^n (y_i - \bar{y})^2}}. \quad (4.27)$$

The numerator calculates the covariance of the data sets which is then normalized by the denominator which represents the standard deviations of each data set. Thus, the Pearson correlation coefficient  $\rho$  varies from -1 to +1. The less the data sets are linear correlated, the closer the correlation coefficient is to zero. A value of -1 represents perfect anti-proportional correlation, while a value of 1 shows perfect positive correlation.

Correlations different from a linear dependency such as circular or harmonic correlations can not be determined by this method, however, such nonlinear correlations are not expected by the data sets investigated in this work.

The Pearson correlation is very sensitive to outliers which can be handled by complementing the correlation coefficient with Spearmans rank correlation, although it is rather constructed to disentangle and find kinetic relationships, in other words to show correlations of monotonic character. The Spearman correlation coefficient is defined similar to the Pearson correlation coefficient. Instead of using the data sets themselves, Spearman's rank correlation sorts this

data sets and calculates the relationship of the corresponding ranks  $rx$  and  $ry$  according to

$$\rho_{xy} = \frac{\sum_{k=1}^n (rx_i - \bar{rx})(ry_i - \bar{ry})}{\sqrt{\sum_{k=1}^n (rx_i - \bar{rx})^2} \sqrt{\sum_{k=1}^n (ry_i - \bar{ry})^2}}. \quad (4.28)$$

By this method, outliers remain part of the population without decreasing the correlation for all other elements of the population. Pearson and Spearman's rank correlation coefficient should be considered in combination. If there are large deviations between the correlation values, there probably is an outlier which can be determined by visual inspection when data set  $x$  is plotted against data set  $y$ .

Once a correlation value is calculated the question about the statistical significance of this value is important. The smaller the sample size  $N$  that is to be correlated, the higher is the chance that this correlation value occurred by chance. For this purpose Student's  $t$ -value is calculated, which depends on the number of samples  $N$ . Deviations from the mean of a normally distributed population are  $t$  distributed <sup>[4]</sup>. Employing the formula from Steigers  $Z$ -test the  $t$ -value can be calculated with the corresponding Pearson correlation coefficient  $\rho_{xy}$  according to

$$t = \frac{\sqrt{N-2} \cdot \rho_{xy}}{\sqrt{1-\rho_{xy}^2}}. \quad (4.29)$$

This  $t$ -value can be extracted from a  $t$ -distribution table <sup>[38]</sup> to determine the probability that the correlation is a false positive, i. e. occurred by chance.

**Example:** Say the sample size  $N$  is 9 and the Pearson correlation coefficient equals 0.59. The corresponding  $t$ -value according to equation 4.29 is 1.911. Looking up in the  $t$ -distribution table in the row for a sample size of 9 (this column is often also named "degrees of freedom" or  $df$  which equals  $N-2$ , so in this case the row with the entry 7 would correspond to a sample size of 9) the  $t$ -value is between a tail probability of 5% and 2,5%. Thus, the probability that the correlation value of 0.59 for a sample size of 9 occurs randomly is between 5 and 2,5%.

During this work a program called "CorCoef" was written. It is the combination of a Fortran code "correlation.f" and a shell script "corcoef.sh". The corresponding source codes can be found in the appendix of this work. It calculates Pearson and Spearman correlation coefficients.



## **5 Insights into the structure of the active site of the O<sub>2</sub>-tolerant membrane bound [NiFe] hydrogenase of *R. eutropha* H16 by molecular modelling**

Before the structure of the reduced MBH from *Ralstonia eutropha* was available homology models of the enzyme were constructed using known structures of the standard hydrogenases *D. vulgaris* Miyazaki F<sup>[30]</sup> and *D. gigas*<sup>[49]</sup> as a templates. Infrared spectra were calculated on the QM/MM level of theory in combination with MD simulations for the wildtype and C81S mutant. The CO stretching mode was calculated to shift to higher wavenumbers for the mutant which reproduces the shift in the experimental data well. This finding confirms the validity of the constructed models and the previous suggestions of an active site arrangement similar to standard hydrogenases.<sup>[12,41,42]</sup> Furthermore, calculations on different QM/MM partition schemes showed the significant influence of amino acids that are hydrogen bonded to the inorganic CN<sup>-</sup> ligands on calculated IR frequencies. Another important conclusion was the necessity to integrate specific water molecules into the modelled structure. Their influence on the structure and hence calculated frequencies must not be neglected.

Structure alignments of the modelled and the x-ray crystallographic structure of the reduced MBH showed only minor differences at the active site structure confirming the homology model technique applied in this publication.

Cite this: DOI: 10.1039/c1cp21045a

www.rsc.org/pccp

## Insights into the structure of the active site of the O<sub>2</sub>-tolerant membrane bound [NiFe] hydrogenase of *R. eutropha* H16 by molecular modelling†

Yvonne Rippers,‡ Tillmann Utesch,‡ Peter Hildebrandt, Ingo Zebger and Maria Andrea Mroginski

Received 4th April 2011, Accepted 27th July 2011

DOI: 10.1039/c1cp21045a

**Structural models for the Ni-B state of the wild-type and C81S protein variant of the membrane-bound [NiFe] hydrogenase from *Ralstonia eutropha* H16 were derived by applying the homology model technique combined with molecular simulations and a hybrid quantum mechanical/molecular mechanical approach. The active site structure was assessed by comparing calculated and experimental IR spectra, confirming the view that the active site structure is very similar to those of anaerobic standard hydrogenases. In addition, the data suggest the presence of a water molecule in the second coordination sphere of the active centre.**

Hydrogenases are enzymes which catalyse the reversible heterolytic cleavage of molecular hydrogen. In the focus of our study are [NiFe] hydrogenases, in which the catalytic site is a bimetallic complex, with two Ni bound terminal cysteine residues, three exogenous diatomic inorganic ligands (one CO and two CN<sup>-</sup>) at the Fe atom, and two further cysteines bridging the two metal atoms.<sup>1</sup> Depending on the particular redox state another, different ligand may occupy an additional bridging position between Ni and Fe. Most members of this enzyme family are oxygen-sensitive and form under electron-deficient conditions with O<sub>2</sub> the so-called ‘unready inactive’ Ni<sub>u</sub>-A state, that requires a rather long time (up to several hours) for a reductive (re-)activation by molecular hydrogen, a property that impairs practical applications.<sup>1</sup> The membrane-bound [NiFe] hydrogenase (MBH) from *Ralstonia eutropha* H16 (*ReH16*), however, is capable of oxidizing hydrogen even at atmospheric oxygen levels. Under these conditions only the so-called ‘ready inactive’ Ni<sub>r</sub>-B state is formed which is rapidly reactivated on the (sub-)second time scale, while the Ni<sub>u</sub>-A state has never been observed for the wild type MBH.<sup>2,3</sup> Therefore, this enzyme appears to be a promising candidate in the field of biotechnological energy storage and conversion as an alternative to fossil fuels.<sup>4</sup> Ni<sub>r</sub>-B harbors a hydroxide in

the bridging position between Ni and Fe,<sup>5,6</sup> while a hydroperoxide is suggested to be the bridging ligand in Ni<sub>u</sub>-A.<sup>7</sup> These two states can be distinguished by IR spectroscopy which, in general, is a particularly instructive method for the identification of the various redox states involved in the catalytic cycle by probing the stretching modes of the CO and CN<sup>-</sup> ligands.<sup>8,9</sup>

So far, however, no crystallographic structures of oxygen tolerant [NiFe] hydrogenases have been reported, which would facilitate a more detailed investigation of the underlying reaction mechanism at the active site. In this work, we have constructed a homology model for the MBH from *ReH16* using the known three-dimensional (3D) structures of the standard [NiFe] hydrogenases as a template. The homology model was further refined by molecular dynamics (MD) simulations and quantum-mechanics/molecular mechanics (QM/MM) geometry optimizations of the active site, followed by the calculation of the IR spectra. Three structural models of the oxidized MBH in the Ni<sub>r</sub>-B state were generated: MBH wild type (*MBH* model), MBH wild type including a water molecule in the second coordination sphere of the [NiFe] center as detected in other 3D structures of oxygen-sensitive hydrogenases (*MBH-H<sub>2</sub>O* model) and the C81S variant MBH (*MBH-C81S-H<sub>2</sub>O* model) which also contains the extra water. The latter protein variant was chosen because the mutation induces a significant 8 cm<sup>-1</sup> shift of the CO stretching in the experimental IR spectrum.<sup>10</sup> Hence, the reproduction of a mutation-induced shift is considered as a more reliable criterion for the quality of the homology model in the active site than a comparison between the wild type MBH and the template enzyme *D. gigas* for which the frequency difference was only 2 cm<sup>-1</sup> and thus close to the experimental accuracy. The quality of the resulting structures was further evaluated via a Ramachandran plot analysis<sup>11</sup> (see Fig. S2 in the ESI†).

The far-reaching sequence identity between the template and the target of 44% leads to an initial model structure with a low overall root-mean-square deviation (with respect to the template) of 0.8 Å for the backbone atoms of both the small and the large subunit. This is particularly true for the environment of the bimetallic center, constituted by highly conserved amino acids. As a consequence, the active structure in the homology model is essentially the same as for the template. In this region only minor structural differences were observed due

Institut f. Chemie, Sekr. PC14, Technische Universität Berlin, Straße des 17. Juni 135, D-10623 Berlin, Germany.  
E-mail: andrea.mroginski@tu-berlin.de; Fax: +49 30 31421122;  
Tel: +49 30 31426403

† Electronic supplementary information (ESI) available. See DOI: 10.1039/c1cp21045a

‡ These authors contributed equally to the work and are listed alphabetically.

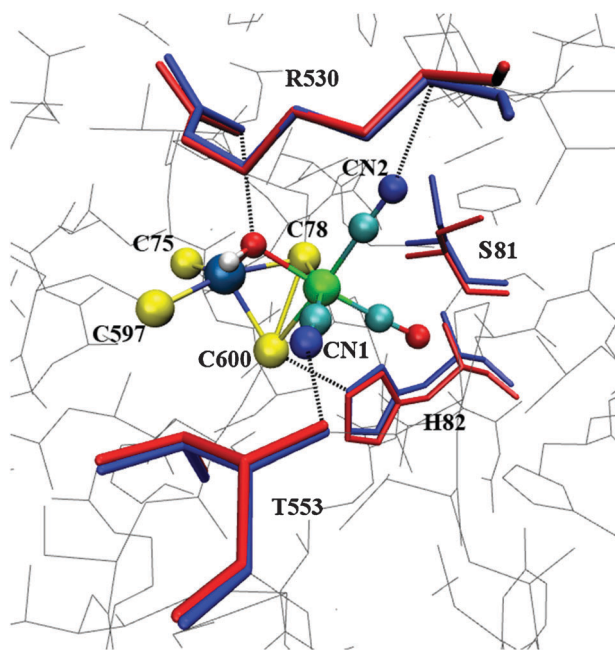


**Fig. 1** Active site structure of *MBH-C81S* including a water molecule in the second coordination sphere (not displayed for the sake of clarity) and the amino acids R530, T553, H82 and S81 in two conformations (blue and red). Dashed lines indicate hydrogen bonds. The atoms of the bimetallic centre are represented by balls (S, yellow; O, red; C, cyan; N, blue; H, white; Ni, dark blue; Fe, green). Grey lines represent the protein matrix; all amino acids are shown without hydrogen atoms.

to the replacement of threonine by a serine at position 553. Larger deviations in the homology models are noted in surface loop regions. In all three structural models, important secondary structure elements are conserved (see Fig. S3 in the ESI†).

As observed in standard hydrogenases, the active sites in all our calculated models are embedded in the protein forming coordinative bonds between the metals and cysteine residues. Furthermore, the bimetallic centre is stabilized by a hydrogen bond network including, among others, interactions between the cyanide ligands CN and CN2 to the backbone nitrogens of T553 and R530, respectively. Except for the *MBH* model stable hydrogen bonds are established between the OH<sup>-</sup> bridge and the side-chain nitrogen of R530. For all models only weaker hydrogen bonds are formed between the bridging sulfur of C78 or C600, respectively, and the N<sub>c</sub> of H82 located in the first coordination sphere, as described previously<sup>12</sup> (Fig. 1). It is interesting to note that the analysis of the MD trajectories for the *MBH-C81S-H<sub>2</sub>O* model reveals two distinct conformations associated with Ser81 (Fig. 1).

The active site optimized by QM/MM calculations is a very rigid construct reflected by very low standard deviations computed over the series of snapshots (see Table S3 in the ESI†). A comparison with the crystallographic structure of *D. gigas* (2FRV),<sup>13</sup> also harboring two CN<sup>-</sup> and one CO ligands, indicates a shortening of the Fe–OH<sup>-</sup>, the Ni–S(C78), the Ni–S(C597) and the Ni–S(C600) bonds in the optimized structure. The length of the Fe–CO bond is reduced from 1.87 Å in the crystallographic structure to around 1.72 Å in our model. The Fe–CN1 bond is very similar in length to

the crystallographic structure, while the Fe–CN2 bond is elongated to 1.90 Å in our model (2FRV: 1.67 Å). This comparison further supports the view of a standard hydrogenase-like catalytic centre in the MBH. Compared to previous theoretical calculations performed on the active site of *D. gigas* in the Ni–B state,<sup>14</sup> the differences in the crystallographic structures are reduced in the present model except for a slightly larger difference for the Ni–S(C533) and Ni–OH<sup>-</sup> bonds. Earlier theoretical models presented by Stein and Lubitz<sup>15</sup> display even higher differences, which might be related to the exclusion of the protein charge cloud (see Table S5 in the ESI†).

To validate the derived structural model of the catalytic centre IR spectra of the [NiFe] centre were computed (see Methods) and compared with the corresponding experimental data.<sup>10</sup> A similar procedure has been employed in the past for determining the structure of a guanosine triphosphate (GTP) ligand bound to a Ras protein.<sup>16</sup> Calculated spectra were obtained from 25 snapshots of the MD trajectory. The average frequencies and their standard deviations are listed in Table 1. The experimental IR spectrum in the region between 1890–2110 cm<sup>-1</sup> exclusively displays the stretching modes of the inorganic ligands with a prominent band at 1947 cm<sup>-1</sup> originating from the CO stretching vibration, and two weaker bands at 2080 cm<sup>-1</sup> and 2098 cm<sup>-1</sup> assigned to the asymmetric and symmetric CN stretching modes, respectively.<sup>2</sup> In the IR spectrum of the C81S MBH mutant, the CO stretching mode is shifted to higher wavenumbers by 8 cm<sup>-1</sup> whereas the CN stretching modes remain largely unchanged.<sup>10</sup>

In the *MBH* model consisting of a QM partition of 26 atoms (*vide infra*), analysis of the calculated spectra shows an overestimation of the vibrational frequencies of the CO and CN stretching modes,  $\nu(\text{CO})$  and  $\nu(\text{CN})$ , compared to the experimental values (Table 1). Incorporation of water adjacent to the [NiFe] centre significantly improves the estimated  $\nu(\text{CO})$  frequency, which is now predicted at 1950 cm<sup>-1</sup> and thus very close to the experimental value. However, the frequencies of the CN stretching modes are still overestimated. In presence of water, C81 is forced towards the CO ligand such that the CO–HS distance decreases from 6.4 Å in the *MBH* model to only 2.4 Å in the *MBH-H<sub>2</sub>O* model. A further improvement is achieved by enlarging the QM partition to 75 atoms, including R530, T553, and H82 which are involved in hydrogen bond interactions with the CN ligands and the OH bridging ligand. With this model, not only the CO stretching is very well reproduced but also the CN stretching modes are predicted at much lower frequencies such that they coincide distinguished with the experimental values. The difference between

**Table 1** Calculated and experimental frequencies (in cm<sup>-1</sup>) for the wild type MBH and the C81S mutant. The calculated average frequencies are accompanied by the standard deviations computed over 25 spectra

		$\nu(\text{CO})$	$\nu(\text{CN})_{\text{asym}}$	$\nu(\text{CN})_{\text{sym}}$
Exp.	MBH-WT	1947	2080	2098
Calc.	MBH (QM26)	1970 ± 4	2106 ± 4	2120 ± 4
	MBH-H <sub>2</sub> O (QM26)	1950 ± 5	2097 ± 6	2128 ± 5
	MBH-H <sub>2</sub> O (QM75)	1954 ± 5	2078 ± 4	2098 ± 3
Exp.	MBH-C81S	1955	2080	2097
Calc.	MBH-C81S-H <sub>2</sub> O (QM75)	1959 ± 8	2081 ± 12	2110 ± 5

the  $\nu(\text{CN})$  frequencies computed for the *MBH* and *MBH-H<sub>2</sub>O* models appear to be related to minor structural changes of the environment, such as the twisting of the R530 and the T553 side chains.

Also the IR spectra calculated for the *MBH-C81S-H<sub>2</sub>O* model exhibit a very good agreement with the experimental IR spectrum. The experimental frequency upshift of 8 cm<sup>-1</sup> compared to the WT protein is very well reproduced by the calculations. The good agreement also holds for the asymmetric CN stretching while only the symmetric CN stretching is overestimated by the calculations. The frequency upshift of the CO stretching can be explained as a consequence of the higher polarity of the serine side chain, which is represented by a larger negative point charge, reducing the backbonding from the iron and strengthening the CO bond (blue-shifted).<sup>8</sup> On the other hand, the CO stretching frequency calculated for the *MBH-C81S-H<sub>2</sub>O* model is lower by 10 cm<sup>-1</sup> compared to that of the *MBH* model lacking the internal water molecule. Thus, the comparison of the experimental and calculated spectra for the WT and C81S variants provides strong support for a water molecule close to the [NiFe] centre. Note that the variations of the CN stretching frequencies for the *MBH-C81S-H<sub>2</sub>O* model are larger than for the WT model, which is attributed to the fluctuations of the hydrogen bond network involving the CN<sup>-</sup> ligands.

For the *MBH-H<sub>2</sub>O* model and the *MBH-C81S-H<sub>2</sub>O* model, calculated potential energy distributions show that the asymmetric  $\nu(\text{CN})$  mode is dominated by the stretching of the CN1 ligand, while the symmetric  $\nu(\text{CN})$  mode mainly contains the stretching of the CN2 ligand. Interestingly, there is a change of the hydrogen bond network involving H82 and the bridging cysteines. For the WT *MBH*, the hydrogen bond is formed with the sulfur atom of C78 whereas for the C81S mutant, it is formed with the bridging sulfur atom from C600. Analysis of the 25 snapshot structures with their corresponding vibrational spectra shows that there is a linear correlation between the strength of this hydrogen bond and the  $\nu(\text{CO})$  frequency: a stronger hydrogen bond is reflected by an increase of the  $\nu(\text{CO})$  frequency.

In summary, the theoretical 3D structural models of the *MBH* show only minor structural rearrangements of the active site and its vicinity compared to standard hydrogenases. These results confirm previous suggestions<sup>2,3,24</sup> of a very similar catalytic centre in oxygen-tolerant and -sensitive [NiFe] hydrogenases, ruling out that the molecular origin of the oxygen-tolerance of *MBH* is related to a specific modification at the catalytic centre. The reliability of the present structural model for the active site of *MBH*, with a high similarity to oxygen-sensitive “standard” [NiFe] hydrogenases, is supported by the distinguished agreement between experimental and the QM/MM calculated IR spectra and specifically by the reproduction of the IR spectroscopic changes related to a single mutation of C81 to serine located in the second coordination sphere of the active site. In addition, these calculations indicate a water molecule close to C81, which influences the IR spectra. The present results constitute another example<sup>16</sup> where the combination of molecular modelling with a spectroscopic validation represents a valuable tool for the structural analysis of enzymes for which no crystal structures are available.

## Methods

### Homology modeling

The *MBH* homology models were constructed with Modeller v9.5<sup>17</sup> using the structures of the standard hydrogenases of *inter alia* *D. vulgaris* Miyazaki F<sup>18</sup> and *D. gigas*<sup>13</sup> as a template for the overall protein and the active site structure, respectively. Based on spectroscopic studies, the structure of the Ni-B state of the active site includes one CO, and two CN<sup>-</sup> ligands and an OH<sup>-</sup> bridging ligand.<sup>5,6</sup> In the *MBH-H<sub>2</sub>O* model, one water molecule was added adjacent to the active site. The C81S variant structure was constructed by replacing C81 by a serine followed by a short energy minimization run. Following the same procedure as for the *MBH-H<sub>2</sub>O* model, a water molecule was placed in the active site cavity of the C81S mutant. MD simulations were performed to relax and to equilibrate the three structural models in TIP3P water boxes.<sup>19</sup> The internal motions of the [NiFe] centre and the Fe-S clusters were strongly constrained during the MD simulations (see ESI 1†).

### Geometry optimization of the active site

25 snapshots were extracted from the MD trajectory. The respective geometries were optimized at the QM/MM level of theory by combining density functional theory (DFT) calculations using the BP86 functional with CHARMM22 force field. The QM part consists either of 26 atoms containing the bimetallic centre with Ni(III) and Fe(II), the exogenous ligands, and the side chains of the four coordinating cysteines, or of 75 atoms by including R530, T553, and H82. The 6-31g(d) basis set was applied for all atoms excluding Ni and Fe for which Ahlrichs triple-zeta polarization all electron basis set (TZVP) was employed.<sup>20</sup> Covalent bonds at the QM/MM border were cut and saturated by hydrogen link atoms. The coupling between QM and MM was computed using electrostatic embedding with a charge-shift scheme.<sup>21</sup> Final models were constructed by averaging over the 25 individual structures (see ESI 4†).

### Spectra calculation

IR spectra of the active site were calculated for each snapshot using the normal mode analysis approximation following the procedure described previously by Mrogiński *et al.*<sup>22</sup> The final IR spectra for each model were computed using the instantaneous normal mode analysis (INMA) approach.<sup>23</sup>

## Acknowledgements

We thank the DFG (Cluster of Excellence “UniCat”) for financial support and the “Norddeutscher Verbund für Hoch- und Höchstleistungsrechnen” (HLRN) for providing computer resources.

## Notes and references

- J. C. Fontecilla-Camps, A. Volbeda, C. Cavazza and Y. Nicolet, *Chem. Rev.*, 2007, **107**, 4273–4303.
- M. Saggi, I. Zebger, M. Ludwig, O. Lenz, B. Friedrich, P. Hildebrandt and F. Lendzian, *J. Biol. Chem.*, 2009, **284**, 16264–16276.
- O. Lenz, M. Ludwig, T. Schubert, I. Büstel, S. Ganskow, T. Goris, A. Schwarze and B. Friedrich, *ChemPhysChem*, 2010, **11**, 1107–1119.

- 4 K. A. Vincent, J. A. Cracknell, O. Lenz, I. Zebger, B. Friedrich and F. A. Armstrong, *Proc. Natl. Acad. Sci. U. S. A.*, 2005, **102**, 16951–16954.
- 5 A. J. Pierik, W. Roseboom, R. P. Happe, K. A. Bagley and S. P. J. Albracht, *J. Biol. Chem.*, 1999, **274**, 3331–3337.
- 6 M. van Gastel, M. Stein, M. Brecht, O. Schröder, F. Lenzian, R. Bittl, H. Ogata, Y. Higuchi and W. Lubitz, *J. Biol. Inorg. Chem.*, 2006, **11**, 41–51.
- 7 A. Volbeda, L. Martin, C. Cavazza, M. Matho, B. W. Faber, W. Roseboom, S. P. Albracht, E. Garcin, M. Rousset and J. C. Fontecilla-Camps, *J. Biol. Inorg. Chem.*, 2005, **10**, 239–249.
- 8 A. L. De Lacey, V. M. Fernandez, M. Rousset and R. Cammack, *Chem. Rev.*, 2007, **107**, 4304–4330.
- 9 M. E. Pandelia, H. Ogata and W. Lubitz, *ChemPhysChem*, 2010, **11**, 1127–1140.
- 10 M. Saggi, M. Ludwig, B. Friedrich, P. Hildebrandt, R. Bittl, F. Lenzian, O. Lenz and I. Zebger, *ChemPhysChem*, 2010, **11**, 1215–1224.
- 11 R. W. W. Hoof, G. Vriend, C. Sander and E. E. Abola, *Nature*, 1996, **381**, 272–272.
- 12 C. Stadler, A. L. de Lacey, Y. Montet, A. Volbeda, J. C. Fontecilla-Camps, J. C. Conesa and V. M. Fernandez, *Inorg. Chem.*, 2002, **41**, 4424–4434.
- 13 A. Volbeda, E. Garcin, C. Piras, A. L. de Lacey, V. M. Fernandez, E. C. Hatchikian, M. Frey and J. C. Fontecilla-Camps, *J. Am. Chem. Soc.*, 1996, **118**, 12989–12996.
- 14 P. Jayapal, M. Sundararajan, I. H. Hillier and N. A. Burton, *Phys. Chem. Chem. Phys.*, 2008, **10**, 4249–4257.
- 15 M. Stein and W. Lubitz, *Phys. Chem. Chem. Phys.*, 2001, **3**, 2668–2675.
- 16 M. Klähn, J. Schlitter and K. Gerwert, *Biophys. J.*, 2005, **88**, 3829–3844.
- 17 A. Sali and T. L. Blundell, *J. Mol. Biol.*, 1993, **234**, 779–815.
- 18 H. Ogata, S. Hirota, A. Nakahara, H. Komori, N. Shibata, T. Kato, K. Kano and Y. Higuchi, *Structure*, 2005, **13**, 1635–1642.
- 19 W. L. Jorgensen, J. Chandrasekhar, J. D. Madura, R. W. Impey and M. L. Klein, *J. Chem. Phys.*, 1983, **79**, 926–935.
- 20 F. Weigend and R. Ahlrichs, *Phys. Chem. Chem. Phys.*, 2005, **7**, 3297–3305.
- 21 D. Bakowies and W. Thiel, *J. Phys. Chem.*, 1996, **100**, 10580–10594.
- 22 M. A. Mroginiski, F. Mark, W. Thiel and P. Hildebrandt, *Biophys. J.*, 2007, **93**, 1885–1894.
- 23 M. Nonella, G. Mathias and P. Tavan, *J. Phys. Chem. A*, 2003, **107**, 8638–8647.
- 24 J. Fritsch, S. Löscher, O. Sanganas, E. Sieber, I. Zebger, M. Stein, M. Ludwig, A. L. De Lacey, H. Dau, B. Friedrich and O. Lenz, *Biochemistry*, 2011, **50**, 5858–5869.



## 6 Revealing the Absolute Configuration of the CO and CN<sup>-</sup> Ligands at the Active Site of a [NiFe] Hydrogenase

In 1997 Happe et al. used with <sup>13</sup>C and <sup>15</sup>N labeling experiments to prove that the active site of [NiFe] hydrogenases contains two CN<sup>-</sup> and one CO ligand at the iron<sup>[13]</sup>. On this basis de Lacey et al. suggested the CO ligand being in *trans*-position to the substrate binding site (see figure 1.2), whereas the two CN<sup>-</sup> ligands should be embedded in hydrophilic pockets allowing for hydrogen-bonding interactions<sup>[24]</sup>. In contrast to this widely accepted spatial arrangement, the x-ray crystal structure of the MBH from *Ralstonia eutropha* published in 2011 suggested a different structural configuration of the three inorganic ligands<sup>[12]</sup>.

In the following publication the active site configuration of the three inorganic ligands bound to the iron was investigated on the basis of three different models representing the three different possible configurations of the ligands. The combination of MD simulations and QM/MM vibrational calculations in comparison with experimental IR spectra confirmed the widely accepted *trans*-position of the CO ligand. Furthermore, this work pointed out the configurational problems of the x-ray crystallographic structure of the reduced MBH<sup>[12]</sup>.

Based on previous studies and reviews<sup>[13,22,24]</sup>, in this work the absolute configuration of the three inorganic ligands at the [NiFe] hydrogenase active site was unambiguously determined.

# Revealing the Absolute Configuration of the CO and CN<sup>-</sup> Ligands at the Active Site of a [NiFe] Hydrogenase

Yvonne Rippers, Marius Horch, Peter Hildebrandt, Ingo Zebger, and Maria Andrea Mroginski\*<sup>[a]</sup>

Combined molecular dynamics (MD) and quantum mechanical/molecular mechanical (QM/MM) calculations were performed on the crystal structure of the reduced membrane-bound [NiFe] hydrogenase (MBH) from *Ralstonia eutropha* to determine the absolute configuration of the CO and the two CN<sup>-</sup> ligands bound to the active-site iron of the enzyme. For

three models that include the CO ligand at different positions, often indistinguishable on the basis of the crystallographic data, we optimized the structures and calculated the ligand stretching frequencies. Comparison with the experimental IR data reveals that the CO ligand is in *trans* position to the substrate-binding site of the bimetallic [NiFe] cluster.

## 1. Introduction

Hydrogenases are metalloenzymes that catalyze the reversible heterolytic splitting of molecular hydrogen into protons and electrons.<sup>[1]</sup> Oxygen-tolerant hydrogenases, which are capable to cycle hydrogen under aerobic conditions, are promising candidates for the development of bioenergetic applications using hydrogen as a clean fuel.

Herein, we focus on so-called [NiFe] hydrogenases, whose active site harbors one iron and one nickel. These two metals are embedded in the protein matrix by two bridging cysteinyl thiolates between Ni and Fe, leaving a third bridging position for substrate or inhibitor binding. In addition, the Ni is coordinated by two further cysteinyl thiolates in terminal positions. Including the varying ligand at the third bridging site, a square pyramidal coordination sphere with the tip pointing towards one of the two bridging thiolates is formed at the Ni. The Fe is held in the low-spin Fe<sup>II</sup> configuration by the three bridging ligands, one carbonyl, and two cyanides.<sup>[2]</sup>

The present picture of the biologically unusual [NiFe] site of these enzymes evolved from a number of spectroscopic and crystallographic studies. In 1995, Volbeda et al. solved the first crystal structure of a [NiFe] hydrogenase from *Desulfovibrio gigas*, revealing three distinct regions of electron density close to the iron that were not attributable to the protein environment.<sup>[3]</sup> Considering the third bridging ligand and the bridging cysteinyl donors, these densities indicated an octahedral coordination sphere at the Fe (Figure 1). At the same time Bagley et al. discovered three absorption bands between 2100 and 1900 cm<sup>-1</sup> in the infrared (IR) spectrum of the [NiFe] hydrogenase from *Allochromatium vinosum*, one prominent low-frequency band and two less intense absorptions at higher wavenumbers. The exact band positions of all three bands appeared to be sensitive towards electron-density changes at the Ni, reflecting different redox states of the enzyme.<sup>[4]</sup> In 1996, Volbeda et al. related these three IR absorptions to the unassigned electron-density regions at the iron. In this context, they proposed the presence of CO and/or CN<sup>-</sup> ligands with the two

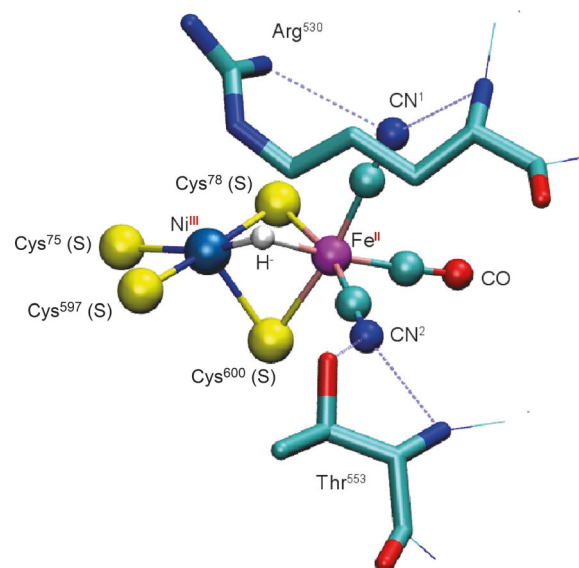


**Figure 1.** Three dimensional scheme of the active site in the Ni<sub>3</sub>-C state with the CO *trans* to the substrate-binding site, occupied with a hydride ligand. Color representations: cyan (C), blue (N), red (O).

low-intensity bands arising from stretching vibrations of a coupled oscillator,<sup>[5]</sup> as proven later by partial labeling experiments.<sup>[6]</sup> For such a scenario, the angle between the two equal oscillators can be roughly estimated from the absorbance ratio of the corresponding stretching bands,<sup>[7a-c]</sup> although this ap-

[a] Y. Rippers, M. Horch, Prof. P. Hildebrandt, Dr. I. Zebger, Prof. M. A. Mroginski  
Institut für Chemie  
Technische Universität Berlin  
Straße des 17. Juni 135, 10623 Berlin (Germany)  
Fax: (+49) 30-314-21122  
E-mail: andrea.mroginski@tu-berlin.de

Supporting information for this article is available on the WWW under <http://dx.doi.org/10.1002/cphc.201200562>.

proach has been discussed controversially.<sup>[8]</sup> In fact, for [NiFe] hydrogenases, the calculated angle resembled that between the electron densities of the ligands in position CN<sup>1</sup> and CN<sup>2</sup> (Figure 1) in the crystal structure from *Desulfovibrio gigas*, giving a first hint about the actual positions of the two equal ligands. In 1997, Happe et al. carried out <sup>15</sup>N and <sup>13</sup>C labeling experiments proving that the active site of [NiFe] hydrogenases contains indeed one CO and two CN<sup>-</sup> ligands.<sup>[9]</sup> In the same year, de Lacey et al. tentatively suggested the spatial arrangement for the three ligands based on the protein environment of the *Desulfovibrio gigas* hydrogenase. The authors proposed that the negatively charged CN<sup>-</sup> ligands are embedded in two hydrophilic pockets allowing for hydrogen-bonding interactions (Figure 1), while the CO ligand was proposed to be located in a hydrophobic region *trans* to the substrate bridging site.<sup>[10]</sup> Accordingly, this pattern is widely accepted and is also in line with the proposed role of the CO ligand on hydrogen binding and cleavage in the *trans* position.<sup>[11]</sup> However, CO and CN<sup>-</sup> are isoelectronic and, thus, a definite assignment by means of X-ray diffraction is not possible. Thus, the absolute configuration of the Fe site in [NiFe] hydrogenases, that is, the respective position of the diatomic ligands, is still elusive.

## 2. Results and Discussion

Using the membrane-bound [NiFe] hydrogenase from *Ralstonia eutropha* (MBH) as a model system, we present computational investigations on a recently published crystal structure of the reduced form (PDB entry: 3RGW)<sup>[12]</sup> in order to answer the question about the absolute configuration of the CO and CN<sup>-</sup> ligands. Calculations were performed by means of molecular dynamics (MD) simulations and a hybrid quantum mechanical/molecular mechanical (QM/MM) approach, as well as additional quantum mechanical (QM) computations on a [NiFe] model compound to achieve high comparability to the real system and best efficiency concerning computational costs.

Regarding the polarity of the local environment (pockets) of the inorganic ligands, the protein matrix of the active site of the MBH is similar to that of the *Desulfovibrio gigas* hydrogenase. One pocket, containing Leu<sup>533</sup>, is rather hydrophobic while the other two contain the hydrophilic side chains of Arg<sup>530</sup> and Thr<sup>553</sup>, respectively. These amino acids are able to form hydrogen bonds to the respective inorganic ligand in their vicinities. Here, Arg<sup>530</sup> can form hydrogen bonds both from its backbone amide and the guanidinium group. Likewise, Thr<sup>553</sup> is close enough such that hydrogen bonding is possible for the backbone amide and the hydroxyl side chain (Figure 1). To clarify the geometrical arrangement of the three diatomic ligands, we investigated three different models corresponding to the possible configuration isomers of the Fe site. In these models the CO ligand may either occupy the *trans* position with respect to the third bridging ligand (CO<sub>trans</sub>), or it may reside within the pockets containing Arg<sup>530</sup> (CO<sub>Arg</sub>) or Thr<sup>553</sup> (CO<sub>Thr</sub>). Notably, Fritsch and Scheerer et al. chose the CO<sub>Arg</sub> model for the crystal structure of the reduced MBH,<sup>[12]</sup> in contrast to the general assumption of a hydrophobic CO environment, that is, the CO<sub>trans</sub> model.

These three models were built using the crystal structure of the MBH in the Ni<sub>a</sub>-C state as the starting geometry. Ni<sub>a</sub>-C is the catalytically active form of the enzyme which harbors a hydride ligand in the third bridging position.<sup>[10]</sup> For each of the models several snapshots were extracted out of the MD simulation in order to sample conformational flexibility. The QM/MM-optimized snapshot structures were used for frequency calculations (see Computational Methods). This procedure, which considers fluctuations of the protein environment, provides mean values and standard deviations of the active site properties, which offer more realistic results for interpretation than single-point calculations.

### Structure

We compared the optimized geometries of the three configuration models with the crystal structure of the MBH. Table 1 shows structural parameters extracted from the latter and

**Table 1.** Experimental<sup>[12]</sup> and calculated QM/MM distances and the corresponding standard deviations [Å].

	Exp.	CO <sub>trans</sub>	CO <sub>Arg</sub>	CO <sub>Thr</sub>
Ni-Fe	2.59	2.58 ± 0.01	2.56 ± 0.01	2.56 ± 0.01
Fe-CO	1.90	1.74 ± 0.00	1.72 ± 0.01	1.71 ± 0.00
C-O	1.21	1.18 ± 0.00	1.19 ± 0.00	1.20 ± 0.00
Fe-CN <sup>2</sup>	1.90	1.87 ± 0.00	1.87 ± 0.00	1.90 ± 0.00
C-N <sup>2</sup>	1.16	1.19 ± 0.00	1.19 ± 0.00	1.18 ± 0.00
Fe-CN <sup>1</sup>	1.90	1.87 ± 0.00	1.90 ± 0.00	1.88 ± 0.00
C-N <sup>1</sup>	1.15	1.19 ± 0.00	1.19 ± 0.00	1.19 ± 0.00
Fe-S(Cys <sup>600</sup> )	2.24	2.33 ± 0.01	2.36 ± 0.01	2.32 ± 0.01
Fe-S(Cys <sup>78</sup> )	2.26	2.30 ± 0.01	2.29 ± 0.01	2.33 ± 0.01
Ni-S(Cys <sup>600</sup> )	2.37	2.33 ± 0.01	2.34 ± 0.00	2.34 ± 0.01
Ni-S(Cys <sup>78</sup> )	2.22	2.25 ± 0.01	2.26 ± 0.01	2.25 ± 0.01
Ni-S(Cys <sup>597</sup> )	2.19	2.20 ± 0.01	2.20 ± 0.01	2.21 ± 0.01
Ni-S(Cys <sup>75</sup> )	2.22	2.23 ± 0.00	2.23 ± 0.00	2.23 ± 0.00
N <sub>bb</sub> (R530)-OC/NC	2.85	3.12 ± 0.07	3.23 ± 0.08	3.11 ± 0.07
N <sub>guan</sub> (Arg <sup>530</sup> )-OC/NC	3.14	3.13 ± 0.06	3.32 ± 0.11	3.11 ± 0.05
N <sub>bb</sub> (Thr <sup>553</sup> )-OC/NC	3.05	3.03 ± 0.03	3.04 ± 0.03	3.12 ± 0.04
O(Thr <sup>553</sup> )-OC/NC	2.88	2.77 ± 0.01	2.76 ± 0.01	2.87 ± 0.02
N <sub>e</sub> (His <sup>82</sup> )-S(Cys <sup>600</sup> )	3.29	3.29 ± 0.03	3.36 ± 0.05	3.37 ± 0.05
N <sub>e</sub> (His <sup>82</sup> )-S(Cys <sup>78</sup> )	4.14	4.16 ± 0.07	4.16 ± 0.08	4.14 ± 0.08

mean values over ten snapshots with their standard deviations for all three Ni<sub>a</sub>-C state models. The calculated Ni-Fe distance of 2.58 Å for the CO<sub>trans</sub> model resembles the distance in the crystal structure very well, whereas the values of the other two models differ by about 0.03 Å.

The calculated distance between the Cys<sup>600</sup> and iron differs for all models from the crystal structure value, whereas the distance from N<sub>e</sub> of the strongly conserved His82 residue to the sulphur of Cys<sup>600</sup> is reproduced well for the CO<sub>trans</sub> model (Table 1).

For all models, the standard deviations for the hydrogen-bond distances of Arg<sup>530</sup> are slightly higher than other standard deviations. This is due to a higher flexibility of the long arginine side chain during the MD simulation, resulting in ten rather different snapshot geometries per model. Compared to the crystal structure, the calculated distance from the respec-

tive diatomic ligand (CO or CN<sup>-</sup>) to the backbone nitrogen of arginine is larger by 0.26 to 0.38 Å for all models. However, the distances to the guanidine group of Arg<sup>530</sup> fit well for the CO<sub>trans</sub> and CO<sub>Thr</sub> model, but differ by 0.18 Å for the CO<sub>Arg</sub> model.

Thus, from the structural point of view, deviations from the crystal structure are larger for the model with CO in the arginine pocket, whereas the experimental values are better reproduced by the CO<sub>trans</sub> and CO<sub>Thr</sub> models.

### IR Frequencies

For all models, QM/MM vibrational frequencies were calculated for each geometry-optimized snapshot and compared to experimental values observed for the MBH in the Ni<sub>a</sub>-C state.<sup>[13]</sup> Results in Table 2 show major differences between the three models. In particular, values for the CO stretching mode differ up to more than 100 cm<sup>-1</sup> for the CO<sub>Thr</sub> model from the experimentally observed frequency of 1957 cm<sup>-1</sup>.

Table 2. Standard deviations [cm <sup>-1</sup> ] for the active site of the MBH from <i>Ralstonia eutropha</i> in the Ni <sub>a</sub> -C state.							
Model	Method	$\nu(\text{CO})$	$ \Delta $	$\nu(\text{CN})_{\text{asym}}$	$ \Delta $	$\nu(\text{CN})_{\text{sym}}$	$ \Delta $
exp.	-	1957	-	2075	-	2097	-
CO <sub>trans</sub>	QM/MM	1954 ± 3	3	2058 ± 4	17	2082 ± 2	15
	QM	1922	25	2078	3	2090	7
CO <sub>Arg</sub>	QM/MM	1904 ± 20	53	2058 ± 4	17	2123 ± 2	26
	QM	1920	27	2081	6	2102	5
CO <sub>Thr</sub>	QM/MM	1840 ± 5	107	2082 ± 3	7	2128 ± 2	31
	QM	1916	41	2091	16	2104	7

As the CO ligand is a stronger  $\pi$  acceptor in comparison to the CN<sup>-</sup> ligands, its electronic structure and vibrational properties are more sensitive to electron-density changes at the Fe, resulting in different degrees of  $\pi$  backbonding into the antibonding  $\pi^*$  orbital of the CO ligand. Increased  $\pi$  backbonding weakens the CO bond and causes a low-frequency shift of the corresponding stretching mode.<sup>[14]</sup> Since the energy of the antibonding molecular orbital is lowered by hydrogen bonding, one may readily rationalize the following effects on the calculated CO stretching frequencies (see Table 2). In the CO<sub>Arg</sub> model, the CO ligand is embedded in a rather weak hydrogen-bond network. Consequently, the calculated stretching frequency of the CO ligand in this position is moderately lowered to 1904 cm<sup>-1</sup>. The lowest stretching frequency (1840 cm<sup>-1</sup>) is predicted for the CO ligand in the threonine pocket, which is in line with a stronger hydrogen bonding at this site. In the CO<sub>trans</sub> model, the CO ligand resides in a hydrophobic pocket without hydrogen-bonding donors. Accordingly, the computed CO stretching frequency of 1954 cm<sup>-1</sup> resembles the spectroscopically derived value with a deviation of only 3 cm<sup>-1</sup>, giving the best agreement with the experimental results. For the CO<sub>trans</sub> model, absolute stretching frequencies of the CN<sup>-</sup> ligands are underestimated by 15 to 17 cm<sup>-1</sup>. However, the experimentally obtained splitting of 22 cm<sup>-1</sup> is well reproduced

with a value of 24 cm<sup>-1</sup>. For the CO<sub>Arg</sub> and CO<sub>Thr</sub> the respective splitting between the CN stretching bands is increased by about 20 to 40 cm<sup>-1</sup>. While one of the calculated  $\nu(\text{CN})$  frequencies for the CO<sub>trans</sub> model is reproduced in the other two models, the predicted frequency for the second one is shifted to higher energy in the CO<sub>Arg</sub> and CO<sub>Thr</sub> models. Potential energy distribution (PED) calculations revealed that these  $\nu(\text{CN})$  modes are dominated by the stretching motions of the CN<sup>-</sup> ligand *trans* to the substrate-binding site and, thus, the observed higher frequencies are in line with the lack of hydrogen-bonding amino acids in this pocket.

In summary, the calculated frequencies for the CO<sub>trans</sub> model give the best fit to the experimental data, whereas the other two models can be ruled out on the basis of significant deviations.

To determine influences of the protein environment on vibrational properties of the diatomic ligands, we also performed QM calculations on a recently established model compound of the [NiFe] hydrogenase active site.<sup>[15]</sup> In these calculations, hydrogen bonding and other possible interactions with the protein matrix are not considered, thereby providing insights into metal-ligand bonding effects on the stretching frequencies of the diatomic ligands (Table 2). Differences between the individual configuration isomers are much less pronounced for this model compound compared to the QM/MM model of the MBH. Thus, the significant differences between the isomeric forms in the protein are indeed related to interactions of the ligands with the immediate molecular environment rather than to metal-ligand bonding effects.

### 3. Conclusions

As expected, theoretical results from QM-only and QM/MM calculations demonstrate the significant impact of the protein environment on vibrational properties and structural parameters of the active site in [NiFe] hydrogenases, as exemplified for the MBH from *Ralstonia eutropha*. In particular, calculated frequencies allow a clear discrimination between different possible configurations of the diatomic ligands coordinated to the iron. It has been shown that the CO<sub>trans</sub> model reproduces the experimental values while the other two configurations can be ruled out. In line with previous mechanistic proposals,<sup>[11]</sup> we thus suggest an arrangement of the inorganic ligands at the active site as depicted in Figure 1, that is, with the CO ligand *trans* to the substrate-binding site.

### Computational Methods

For the MD simulations, partial charges for the active site of the MBH were derived by electrostatic potential fits according to the Merz-Singh-Kollmann scheme.<sup>[16a,b]</sup> The quantum mechanical calculations were performed with GAUSSIAN 09<sup>[17]</sup> using the BP86 functional.<sup>[18a,b]</sup> The iron sulfur clusters were treated with the partial charges obtained by Teixeira et al.<sup>[19]</sup> The protonation of the protein side chains was set according a pH value of 7 and the protonation of the histidine residues was adjusted with respect to their specific environments. Subsequently, the protonated MBH was solvated in TIP3P water<sup>[20]</sup> using the VMD1.6<sup>[21]</sup> package. The system

was neutralized by adding sodium as well as chloride ions and was minimized, heated to 300 K and equilibrated in a 1 ns long MD simulation followed by a 1 ns long MD production run. All MD simulations were performed with NAMD 2.7<sup>[22]</sup> using the CHARMM 22 force field.<sup>[23]</sup> The system was handled under periodic boundary and NPT conditions facilitated by Langevin piston dynamics<sup>[24]</sup> with a cut-off of 12 Å for van der Waals interactions and short-range electrostatics. Long-range electrostatics interactions were calculated with the particle-mesh Ewald summation.<sup>[25]</sup> The time step was set to 2 fs. The active site and all iron sulfur clusters were treated as rigid bodies, as parameters for their internal motions were not available.

Out of the 1 ns long MD production run ten snapshots in a 100 ps interval were extracted in order to optimize the geometry and calculate the IR spectra for each snapshot on the QM/MM level of theory using a limited memory quasi-Newton L-BFGS algorithm with the modular program package ChemShell<sup>[26]</sup> and choosing a maximum-gradient component-convergence criterion of 0.0008.

Energies and gradients for the QM part were calculated with the TURBOMOLE 6.30 computational chemistry program. Density functional theory (DFT) calculations were carried out at the BP86<sup>[18a,b]</sup> level of theory using the 6–31 g(d) basis set for all atoms excluding nickel and iron for which Ahlrichs triple-zeta polarization all-electron basis set (TZVP) was employed.<sup>[27]</sup>

In a sphere with a radius of 20 Å around the iron of the active site, the protein was treated molecular mechanically (MM part). For the MM part, the empirical CHARMM22 MM force field<sup>[23]</sup> was employed.

Previous calculations on the active site in our group showed significant improvements of calculated spectra by including amino acids to the QM part that are able to form hydrogen bonds to the active site.<sup>[28]</sup> Thus, the QM part consisted of 83 atoms containing side chains of the four coordinating cysteines, Cys<sup>75</sup>, Cys<sup>78</sup>, Cys<sup>597</sup> and Cys<sup>600</sup>, and further residues, such as His<sup>82</sup>, Arg<sup>530</sup>, and Thr<sup>553</sup>, and the active site with a hydride anion in the third bridging position. Nickel and iron were in the oxidation state +III and +II, respectively. The overall charge of the QM part was –1 e with a multiplicity of M = 2.

Covalent bonds were cut at the QM/MM border and saturated by hydrogen-link atoms. The coupling between QM and MM was computed using the electrostatic embedding approach combined with the charge-shift scheme.<sup>[29]</sup>

Frequency calculations were carried out with GAUSSIAN 09.<sup>[17]</sup> Further degrees of freedom introduced by the addition of hydrogen atoms were projected out of the Hessian matrix before diagonalization.<sup>[30]</sup> IR spectra were calculated for each snapshot using the normal-mode analysis approximation following the procedure described by Mroginiski et al. in ref. [31].

For the QM-only calculations, the BP86 functional<sup>[18a,b]</sup> with the TZVP<sup>[27]</sup> basis set for metals and 6–31 g(d) basis set for all other atoms were applied. The initial coordinates were taken from the crystal structure of the standard hydrogenase from *Desulfovibrio gigas* including all four coordinating cysteine side chains and the active site (see Figure S1 in the Supporting Information). Positions of the alpha carbon atoms of the cysteines were kept fixed during geometry optimization. Frequency calculations were performed with Gaussian 09.<sup>[17]</sup>

## Acknowledgements

We thank the DFG (Cluster of Excellence “UniCat”) for financial supporting and the “Norddeutsche Verbund für Hoch- und Höchstleistungsrechnen” (HLRN) for providing computer resources.

**Keywords:** configuration determination · hydrogenase · IR spectroscopy · metalloenzymes · molecular modeling

- [1] P. M. Vignais, B. Billoud, *Chem. Rev.* **2007**, *107*, 4206.
- [2] J. C. Fontecilla-Camps, A. Volbeda, C. Cavazza, Y. Nicolet, *Chem. Rev.* **2007**, *107*, 4273.
- [3] A. Volbeda, M. H. Charon, C. Piras, E. C. Hatchikian, M. Frey, J. C. Fontecilla-Camps, *Nature* **1995**, *373*, 580.
- [4] K. A. Bagley, E. Duin, W. Roseboom, S. P. J. Albracht, W. H. Woodruff, *Biochemistry* **1995**, *34*, 5527.
- [5] A. Volbeda, E. Garcin, C. Piras, A. L. de Lacey, V. M. Fernandez, E. C. Hatchikian, M. Frey, J. C. Fontecilla-Camps, *J. Am. Chem. Soc.* **1996**, *118*, 12989.
- [6] A. J. Pierik, W. Roseboom, R. P. Happe, K. A. Bagley, S. P. J. Albracht, *J. Biol. Chem.* **1999**, *274*, 3331.
- [7] a) F. A. Cotton, G. Wilkinson, *Advanced Inorganic Chemistry*, Wiley Interscience, New York **1988**; b) B. Steele, *Q. Rev. Chem. Soc.* **1964**, *18*, 21; c) W. Beck, A. Melnikoff, R. Stahl, *Eur. J. Inorg. Chem.* **1966**, *99*, 3721.
- [8] T. L. Brown, D. J. Darensbourg, *Inorg. Chem.* **1967**, *6*, 971.
- [9] R. P. Happe, W. Roseboom, A. J. Pierik, S. P. J. Albracht, *Nature* **1997**, *385*, 126.
- [10] A. L. De Lacey, E. C. Hatchikian, A. Volbeda, M. Frey, J. C. Fontecilla-Camps, V. M. Fernandez, *J. Am. Chem. Soc.* **1997**, *119*, 7181.
- [11] G. J. Kubas, *Chem. Rev.* **2007**, *107*, 4152.
- [12] J. Fritsch, P. Scheerer, S. Frielingsdorf, S. Kroschinsky, B. Friedrich, O. Lenz, C. M. T. Spahn, *Nature* **2011**, *479*, 249.
- [13] M. Saggiu, I. Zebger, M. Ludwig, O. Lenz, B. Friedrich, P. Hildebrandt, F. Lendzian, *J. Biol. Chem.* **2009**, *284*, 16264.
- [14] K. Nakamoto, *Infrared and Raman Spectra of Inorganic and Coordination Compounds - Applications in Coordination, Organometallic and Bioinorganic Chemistry*, John Wiley and Sons, Inc., Hoboken, New Jersey, **2009**, 110–112.
- [15] M. Horch et al., *unpublished results*.
- [16] a) B. H. Besler, K. M. Merz Jr., *J. Comp. Chem.* **1990**, *11*, 431; b) U. C. Singh, P. A. Kollmann, *J. Comput. Chem.* **1984**, *5*, 129.
- [17] *Gaussian 09*, M. J. Frisch, G. W. Trucks, H. B. Schlegel, G. E. Scuseria, M. A. Robb, J. R. Cheeseman, G. Scalmani, V. Barone, B. Mennucci, G. A. Petersson, H. Nakatsuji, M. Caricato, X. Li, H. P. Hratchian, A. F. Izmaylov, J. Bloino, G. Zheng, J. L. Sonnenberg, M. Hada, M. Ehara, K. Toyota, R. Fukuda, J. Hasegawa, M. Ishida, T. Nakajima, Y. Honda, O. Kitao, H. Nakai, T. Vreven, J. A. Montgomery, Jr., J. E. Peralta, F. Ogliaro, M. Bearpark, J. J. Heyd, E. Brothers, K. N. Kudin, V. N. Staroverov, R. Kobayashi, J. Normand, K. Raghavachari, A. Rendell, J. C. Burant, S. S. Iyengar, J. Tomasi, M. Cossi, N. Rega, J. M. Millam, M. Klene, J. E. Knox, J. B. Cross, V. Bakken, C. Adamo, J. Jaramillo, R. Gomperts, R. E. Stratmann, O. Yazyev, A. J. Austin, R. Cammi, C. Pomelli, J. W. Ochterski, R. L. Martin, K. Morokuma, V. G. Zakrzewski, G. A. Voth, P. Salvador, J. J. Dannenberg, S. Dapprich, A. D. Daniels, Ö. Farkas, J. B. Foresman, J. V. Ortiz, J. Cioslowski, D. J. Fox, Gaussian, Inc., Wallingford CT **2009**.
- [18] a) A. D. Becke, *Phys. Rev. A* **1988**, *38*, 3098–3100; b) J. P. Perdew, *Phys. Rev. B* **1986**, *33*, 8822.
- [19] V. H. Teixeira, A. M. Baptista, C. M. Soares, *Biophys. J.* **2006**, *91*, 2035.
- [20] W. L. Jorgensen, J. Chandrasekhar, J. D. Madura, R. W. Impey, M. L. Klein, *J. Chem. Phys.* **1983**, *79*, 926.
- [21] W. Humphrey, A. Dalke, K. Schulten, *J. Molec. Graphics* **1996**, *14*, 33–38.
- [22] J. C. Phillips, R. Braun, W. Wang, J. Gumbart, E. Tajkhorshid, E. Villa, C. Chipot, R. D. Skeel, L. Kale, K. Schulten, *J. Comput. Chem.* **2005**, *26*, 1781.
- [23] A. D. MacKerell, D. Bashford, M. Bellott, R. L. Dunbrack, J. D. Evanseck, M. J. Field, S. Fischer, J. Gao, H. Guo, S. Ha, D. Joseph-McCarthy, L. Kuchnir, K. Kuczera, F. T. Lau, C. Mattos, S. Michnick, T. Ngo, D. T. Nguyen, B. Prodhom, W. E. Reiher, B. Roux, M. Schlenkrich, J. C. Smith, R. Stote, J.

- Straub, M. Watanabe, J. Wiórkiewicz-Kuczera, D. Yin, M. Karplus, *J. Phys. Chem. B* **1998**, *102*, 3586.
- [24] S. E. Feller, Y. H. Zhang, R. W. Pastor, B. R. Brooks, *J. Chem. Phys.* **1995**, *103*, 4613.
- [25] T. Darden, D. York, L. Pedersen, *J. Chem. Phys.* **1993**, *98*, 10089.
- [26] P. Sherwood, A. H. de Vries, M. F. Guest, G. Schreckenbach, C. R. A. Catlow, S. A. French, A. A. Sokol, S. T. Bromley, W. Thiel, A. J. Turner, S. Billeter, F. Terstegen, S. Thiel, J. Kendrick, S. C. Rogers, J. Casci, M. Watson, F. King, E. Karlsen, M. Sjovoll, A. Fahmi, A. Schaefer, C. J. Lenartz, *Mol. Struct. Theochem* **2003**, *632*, 1.
- [27] F. Weigend, R. Ahlrichs, *Phys. Chem. Chem. Phys.* **2005**, *7*, 3297.
- [28] Y. Rippers, T. Utesch, P. Hildebrandt, I. Zebger, M. A. Mroginiski, *Phys. Chem. Chem. Phys.* **2011**, *13*, 16146.
- [29] D. Bakowies, W. Thiel, *J. Phys. Chem.* **1996**, *100*, 10580.
- [30] Q. Cui, M. Karplus, *J. Chem. Phys.* **2000**, *112*, 1133.
- [31] M. A. Mroginiski, F. Mark, W. Thiel, P. Hildebrandt, *Biophys. J.* **2007**, *93*, 1885.

---

Received: July 11, 2012

Published online on September 3, 2012

---

## 7 Resonance Raman Spectroscopy as a Tool to Monitor the Active Site of Hydrogenases

Based on the refined crystal structure of the reduced MBH<sup>[39]</sup>, calculations of vibrational properties using a combined QM/MM and MD simulations approach different reduced and light induced states of the active site (see figure 1.3) were performed for and compared to experimental resonance Raman (RR) data. The results demonstrated that the RR spectroscopical technique is well-suited to probe active site signals as alternative to IR spectroscopy. In this work the *PEC weighted Raman intensities approach* (see section 4.2) was successfully applied to determine the origin of resonance enhanced active site signals. By complementing RR spectroscopy with theoretical calculations and <sup>13</sup>C labeling experiments a light induced state could be identified. For the light induced Ni-L state and the reduced Ni-SR state the underlying structural model suggests that one of the terminal cysteine residues is protonated. This finding confirms a structure previously proposed by Brecht et al.<sup>[5]</sup> and has recently been proven by subatomic resolution protein crystallography<sup>[32]</sup>.

# Resonance Raman Spectroscopy as a Tool to Monitor the Active Site of Hydrogenases\*\*

Elisabeth Siebert, Marius Horch,\* Yvonne Rippers, Johannes Fritsch, Stefan Frielingsdorf, Oliver Lenz, Francisco Velazquez Escobar, Friedrich Siebert, Lars Paasche, Uwe Kuhlmann, Friedhelm Lenzian, Maria-Andrea Mroginski, Ingo Zebger,\* and Peter Hildebrandt\*

In memory of Gernot Renger

[NiFe] hydrogenases are key enzymes in the hydrogen metabolism in many microorganisms and oxidize molecular hydrogen reversibly at a heterobimetallic active site. The released electrons are usually transferred through three iron–sulfur clusters to the physiological redox partner.<sup>[1,2]</sup> The catalytic center has two metal ions Ni and Fe, which are bridged by two cysteinyl thiolates. Two further are bound to the Ni while the Fe is additionally coordinated by three diatomic ligands: one CO and two CN<sup>-</sup>.<sup>[3]</sup> Different redox states of the bimetallic center are largely defined by the oxidation state of the Ni and the chemical nature of an additional ligand at a third bridging position between the two metals, which serves as the cleavage site for hydrogen.<sup>[4,5]</sup>

Elucidating fundamental processes of microbial energy conversion is essential to promote biotechnological applications of hydrogen as a clean fuel.<sup>[6]</sup> In this respect, a comprehensive understanding of the catalytic mechanism of hydrogenase requires the characterization of the active site structure of the species involved. Electron paramagnetic resonance (EPR) and infrared (IR) spectroscopy are well-established techniques for probing the various states of the catalytic cycle.<sup>[4,5]</sup> However, both methods are associated with inherent limitations. EPR spectroscopy is restricted to paramagnetic Ni states, whereas information about the active site Fe (Fe<sup>II</sup>, *S* = 0) is largely inaccessible. IR spectroscopy probes all states of the active site by exploring the stretching vibrations of the diatomic ligands of the Fe. Thereby, it senses variations of the electron density distribution in the bimetallic complex, albeit without immediate insight into the

structure of the [NiFe] center. In this respect, resonance Raman (RR) spectroscopy may be a powerful complementary technique as it allows the vibrational modes that involve the metal ions to be probed selectively, and thus, directly reflects the structural and electronic properties of the [NiFe] site.<sup>[7]</sup>

Herein we demonstrate, for the first time, the capability of RR spectroscopy to provide novel insights into the active site structure of a [NiFe] hydrogenase within a concerted experimental and theoretical approach. In view of the availability of crystal structure data and previous in-depth IR and EPR spectroscopic studies, we have chosen the oxygen-tolerant membrane-bound hydrogenase (MBH) from *Ralstonia eutropha* H16 (*Re*) as a model system.<sup>[8,9]</sup>

RR spectra of H<sub>2</sub>-reduced MBH, measured with a 458 nm excitation at 79 K, display distinct vibrational bands between 400 and 650 cm<sup>-1</sup> (Figure 1A, black line), whereas comparable signals are not observed in the spectrum of the oxidized, as-isolated (untreated) enzyme. The monitored bands appear in the spectral range characteristic of Fe–CO/CN stretching and bending modes,<sup>[10]</sup> as also reported for hydrogenase model compounds.<sup>[11–13]</sup> Contributions from iron–sulfur cluster modes can be excluded as they are lower in frequency and, owing to the resonance enhancement through S→Fe charge-transfer transitions, primarily detectable in the oxidized states.<sup>[14]</sup> These conclusions are supported by Raman spectra calculated for the active site of the MBH by means of a hybrid quantum mechanical/molecular mechanical (QM/MM) model that was recently constructed on the basis of a computationally refined crystal structure of reduced MBH (for computational details, see the Supporting Information S15).<sup>[2,15]</sup> In these calculations, RR intensities were approximated according to the contribution of Fe–CO coordinates to the potential energy distribution (PED) of individual modes to mimic the resonance enhancement by the metal–ligand charge-transfer transition. Indeed, spectra calculated for various states of the active site display distinct bands between 400 and 650 cm<sup>-1</sup>, that is, in the range of the experimental RR bands (see Figure 1). Both the vibrational assignment and the assumption that an Fe→CO charge-transfer electronic transition is the origin for the resonance enhancement of these bands is confirmed by the RR spectrum of <sup>13</sup>C-labeled H<sub>2</sub>-reduced MBH (Figure 1A, red line), which displays distinct isotopic shifts for all major bands, as predicted by the QM/MM calculations (Figure 1B–D, red lines). Only small isotopic shifts, on the order of 1 cm<sup>-1</sup>, are observed upon

[\*] E. Siebert,<sup>[†]</sup> M. Horch,<sup>[†]</sup> Y. Rippers,<sup>[†]</sup> F. Velazquez Escobar, Prof. Dr. F. Siebert, L. Paasche, Dr. U. Kuhlmann, Dr. F. Lenzian, Prof. Dr. M. A. Mroginski, Dr. I. Zebger, Prof. Dr. P. Hildebrandt Technische Universität Berlin, Institut für Chemie, Sekr. PC14 Strasse des 17. Juni 135, 10623 Berlin (Germany)  
E-mail: marius.horch@gmx.de  
ingo.zebger@tu-berlin.de  
hildebrandt@chem.tu-berlin.de

Dr. J. Fritsch, Dr. S. Frielingsdorf, Prof. Dr. O. Lenz Institut für Biologie/Mikrobiologie, Humboldt Universität zu Berlin Chausseestrasse 117, 10115 Berlin (Germany)

[†] These authors contributed equally to this work.

[\*\*] Financial support by the DFG (Cluster of Excellence “UniCat”), Senat Berlin (“Nachhaltige Chemie”).

Supporting information for this article is available on the WWW under <http://dx.doi.org/10.1002/anie.201209732>.

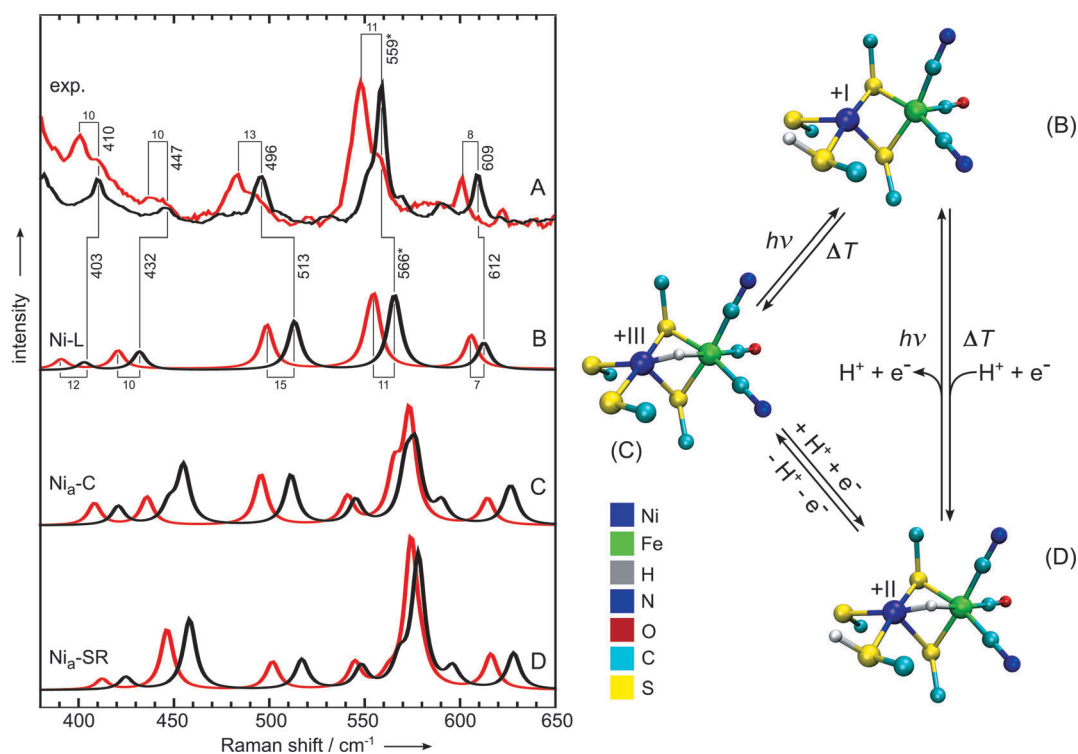


**Figure 1.** Left panel: A) Experimental RR spectra of  $\text{H}_2$ -reduced MBH, obtained with a 458 nm excitation, and calculated Raman spectra of the [NiFe] active site for B) Ni-L, C)  $\text{Ni}_a\text{-C}$ , and D)  $\text{Ni}_a\text{-SR}$ . Black trace non-labeled species; red trace  $^{13}\text{C}$ -labeled species. Bands marked with an asterisk are related to the superposition of two closely adjacent normal modes (see Table 1) and, thus, the corresponding isotopic shifts are deduced from the apparent band maxima. Right panel: active site structure models of B) Ni-L, C)  $\text{Ni}_a\text{-C}$ , and D)  $\text{Ni}_a\text{-SR}$ .

$^{15}\text{N}$  labeling, which is in line with the calculations (see Table 1). Based on these findings, the bands observed in the RR spectrum can be evidentially assigned to bending and stretching modes of the  $\{\text{Fe}(\text{CO})(\text{CN}^-)_2\}$  moiety as also proposed in a recent nuclear resonance vibrational spectroscopy (NRVS) study.<sup>[16]</sup>

Like most other hydrogenases,  $\text{H}_2$ -reduced MBH has a mixture of catalytically active redox species as detected by IR spectroscopy:<sup>[17]</sup>  $\text{Ni}_a\text{-C}$  is the paramagnetic ( $\text{Ni}^{\text{III}}$ ,  $S = 1/2$ ) key intermediate in hydrogen cycling of [NiFe] hydrogenases, carrying a hydride ligand at the third bridging site between the two metals.<sup>[18]</sup> In contrast, the fully reduced  $\text{Ni}_a\text{-SR}$  state,

**Table 1:** Experimental frequencies and isotopic shifts of the active site modes of  $\text{H}_2$ -reduced MBH and calculated values for Ni-L,  $\text{Ni}_a\text{-C}$ , and  $\text{Ni}_a\text{-SR}$  (in  $\text{cm}^{-1}$ ).<sup>[a]</sup>

Normal mode description <sup>[b]</sup> (Ni-L)	Experiment						Calculated								
	$^{12}\text{C}$ , $^{14}\text{N}$	$\Delta^{13}\text{C}$	$\Delta^{15}\text{N}$	$^{12}\text{C}$ , $^{14}\text{N}$	Ni-L $\Delta^{13}\text{C}$	$\Delta^{15}\text{N}$	$^{12}\text{C}$ , $^{14}\text{N}$	$\text{Ni}_a\text{-C}$ $\Delta^{13}\text{C}$	$\Delta^{15}\text{N}$	$^{12}\text{C}$ , $^{14}\text{N}$	$\text{Ni}_a\text{-SR}$ $\Delta^{13}\text{C}$	$\Delta^{15}\text{N}$			
$\delta(\text{Fe-C-O/N})$	410	-10	-1	403	-12	-2	421	-12	-2	425	-12	-2			
$\delta(\text{Fe-C-N}_{\text{Arg}})$ $\nu(\text{Fe-CN}_{\text{Arg}})$	447	-10	-1	432	-11	-3	447	-12	-4	458	-12	-2			
							455	-	-						
$\delta(\text{Fe-C-N}_{\text{Thr}})$ $\nu(\text{Fe-CO})$	496	-13	-1	513	-14	-1	511	-16	-2	517	-15	-2			
							552	-10	n.a. <sup>[c]</sup>				-	-	-
$\delta(\text{Fe-C-O})$ $\nu(\text{Fe-CO})$	559	-11	-1	565	-10	-1	572	-6	-1	568	-5	0			
							567	-3	-1				578	-4	-1
							568	n.a. <sup>[c]</sup>	0				-	-	-
$\nu(\text{Fe-CO})$	609	-8	0	612	-7	-1	625	-	-	628	-12	0			
							628	-13	-1				628	-12	0

which most likely carries the hydride ligand as well,<sup>[4]</sup> is EPR-silent ( $\text{Ni}^{\text{II}}$ ,  $S=0$ ). This species consists of up to three sub-states, which presumably differ in their protonation and spin state or their interaction with the protein environment.<sup>[4,5]</sup>

In principle, both  $\text{Ni}_a\text{-C}$  and  $\text{Ni}_a\text{-SR}$  may contribute to the RR spectrum. At low temperatures, however, irradiation of  $\text{Ni}_a\text{-C}$  with visible light, such as the Raman probe beam at 458 nm, may cause dissociation of the bridging hydride,<sup>[18]</sup> thereby forming the so-called Ni-L state ( $\text{Ni}^{\text{I}}$ ,  $S=1/2$ ), another potentially active intermediate, which also includes up to three sub-states.<sup>[18]</sup> To mimic the conditions of the RR experiments, we have recorded low-temperature IR and EPR spectra in the dark and under constant irradiation at 460 and 455 nm, respectively. The observed signals in the “light-

ever, RR spectra recorded under both conditions were found to be identical in terms of band frequencies and intensities (see Figure SI6), indicating that equal amounts of the same redox state are probed under both conditions. This situation suggests that equilibria between all the reduced states are altered in favor of the detected species during the RR experiment, which is best explained by an efficient photo-conversion into the Ni-L state caused by the Raman probe beam. Indeed, the RR signals vanish if the temperature is raised above 200 K, in line with the previously reported thermal decay of Ni-L.<sup>[4]</sup> Thus, we conclude that the RR spectra of  $\text{H}_2$ -reduced MBH solely reflect the Ni-L state whereas the resonance enhancement of the  $\text{Ni}_a\text{-C}$  and  $\text{Ni}_a\text{-SR}$  species is too weak to give rise to detectable RR signals at 458 nm.

Further support for this assignment is derived from the comparison with Raman spectra calculated for different redox, spin, and protonation states of the active site. The calculated spectra of most of these species differ substantially from the experimental spectrum and, thus, a more detailed inspection is restricted to the calculated spectra of the  $\text{Ni}_a\text{-C}$ , Ni-L, and  $\text{Ni}_a\text{-SR}$  states. For the Ni-L and  $\text{Ni}_a\text{-SR}$  states protonation at the Cys597 sulfur is assumed (Figure 1 B–D). Consistent with the calculations for all three species (see Supporting Information), the strongest band in the experimental spectrum ( $559\text{ cm}^{-1}$ ) reflects two closely spaced modes of predominant Fe–CO bending and stretching character. However, only calculations for Ni-L reproduce both the experimental frequency and the  $^{13}\text{C}$  isotopic shift ( $\Delta\nu$ ) very well, whereas the calculations for  $\text{Ni}_a\text{-C}$  and  $\text{Ni}_a\text{-SR}$  over- and underestimate the frequency and the isotopic shift, respectively. Also the prominent Fe–CO stretching mode, observed at  $609\text{ cm}^{-1}$  ( $\Delta\nu = -8\text{ cm}^{-1}$ ) in the experimental spectrum, is in good agreement with that calculated for Ni-L ( $612\text{ cm}^{-1}$ ,  $\Delta\nu = -7\text{ cm}^{-1}$ ), in contrast to the distinctly overestimated values for  $\text{Ni}_a\text{-C}$  and  $\text{Ni}_a\text{-SR}$ . The calculated spectra of Ni-L also provide the best agreement for the Fe–CN bending (and stretching) modes in the RR spectrum below  $550\text{ cm}^{-1}$ . Thus, the comparison with the calculated spectra confirms that RR spectroscopy exclusively probes the Ni-L state under the experimental conditions employed. Note that the good agreement with the spectrum calculated for Ni-L only refers to the species with a protonated Cys597 (see Supporting Information), thereby giving the first experimental indication of the previously proposed protonation of a terminal cysteine ligand in the active site of [NiFe] hydrogenases.<sup>[20]</sup>

According to the above observations, the amount of Ni-L probed by RR spectroscopy is independent of the initial  $\text{Ni}_a\text{-C}/\text{Ni}_a\text{-SR}$  ratio. Since  $\text{Ni}_a\text{-C}$  is in equilibrium with  $\text{Ni}_a\text{-SR}$ , photoconversion of  $\text{Ni}_a\text{-C}$  could cause a depletion of the  $\text{Ni}_a\text{-SR}$  state if the thermal  $\text{Ni}_a\text{-SR} \rightarrow \text{Ni}_a\text{-C}$  redox transition took place at 79 K. However, this transition can be excluded since the “light-minus-dark” IR difference spectrum in Figure 2 does not display any negative signals arising from  $\text{Ni}_a\text{-SR}$ . Moreover, this thermal reaction would result in an overall increase in paramagnetic species upon irradiation, which is not observed in the corresponding EPR difference spectrum (see Figure 2). Thus, we conclude that there is a yet unknown

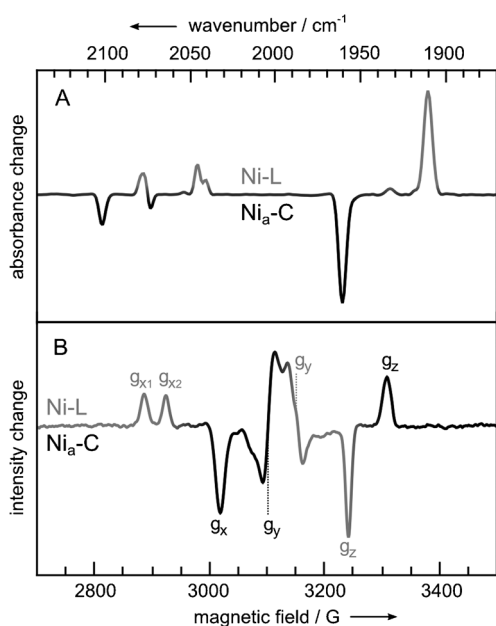


**Figure 2.** Light-induced low temperature difference spectra “light-minus-dark” of  $\text{H}_2$ -reduced MBH, obtained by A) IR and B) EPR spectroscopy. The black signals refer to  $\text{Ni}_a\text{-C}$  and light gray signals refer to Ni-L.

minus-dark” difference spectra (Figure 2) can be assigned on the basis of previous studies:<sup>[17,19]</sup> CO/CN stretching vibrations and g-tensor components displayed in gray, represent the fraction of the enzyme in the Ni-L state formed at the expense of the  $\text{Ni}_a\text{-C}$  state (black), as indicated by the inverse sign of the spectroscopic features. These findings show an essentially complete  $\text{Ni}_a\text{-C} \rightarrow \text{Ni-L}$  conversion, thereby excluding a contribution of the  $\text{Ni}_a\text{-C}$  state to the RR spectrum shown in Figure 1 A.

The spectroscopic experiments on the MBH were further extended to different reducing conditions (see Supporting information). IR spectroscopy indicates that the contribution of  $\text{Ni}_a\text{-C}$  strongly increases at the expense of  $\text{Ni}_a\text{-SR}$ , if the fraction of  $\text{H}_2$  in the gas mixture is decreased from 100 to 5%, reflecting the higher reduction potential of  $\text{Ni}_a\text{-C}$ .<sup>[17]</sup> How-

direct photochemical reaction from Ni<sub>a</sub>-SR to Ni-L that becomes an efficient reaction channel only under high photon flux, for example during the RR experiments.

In conclusion, we have presented the first RR spectroscopic characterization of the active site of a [NiFe] hydrogenase, thereby introducing a novel technique that might also be applied to the characterization of [Fe] and [FeFe] hydrogenases. Herein, RR spectroscopy was shown to provide valuable structural and mechanistic insights by directly probing Fe–CO/CN vibrational modes which reflect bonding properties of the catalytic center that are considered to be key parameters in the hydrogen cycling of hydrogenases.<sup>[21]</sup> Although these Fe–ligand modes are also detectable in NRVS experiments,<sup>[16]</sup> this experimentally more demanding technique suffers from a significantly lower spectral resolution that prevents an identification of specific states of the active site. Conversely, RR spectroscopy allows for an unambiguous redox-state assignment and, thus, a specific characterization of individual species. In concert with complementary spectroscopic and advanced theoretical methods, this technique also provides valuable information on subtle but important details of the active site. This includes first experimental indications for the presence of a protonated terminal cysteine residue at the active site in the Ni-L state and the possibility of a direct photoconversion of Ni<sub>a</sub>-SR into Ni-L. Thus, this integrated approach is capable of elucidating structural and electronic details beyond the level of crystallographic data.<sup>[15]</sup>

Received: December 5, 2012

Revised: January 22, 2013

**Keywords:** [NiFe] hydrogenase · biocatalysis · EPR spectroscopy · IR spectroscopy · resonance Raman spectroscopy

- [1] A. Volbeda, M. H. Charon, C. Piras, E. C. Hatchikian, M. Frey, J. C. Fontecilla-Camps, *Nature* **1995**, 373, 580–587.  
 [2] J. Fritsch, P. Scheerer, S. Frielingsdorf, S. Kroschinsky, B. Friedrich, O. Lenz, C. M. T. Spahn, *Nature* **2011**, 479, 249–252.

- [3] R. P. Happe, W. Roseboom, A. J. Pierik, S. P. Albracht, K. A. Bagley, *Nature* **1997**, 385, 126.  
 [4] W. Lubitz, E. Reijerse, G. M. van Gestel, *Chem. Rev.* **2007**, 107, 4331–4365.  
 [5] A. L. de Lacey, V. M. Fernandez, M. Rousset, R. Cammack, *Chem. Rev.* **2007**, 107, 4304–4330.  
 [6] R. Mertens, A. Liese, *Curr. Opin. Biotechnol.* **2004**, 15, 343–348.  
 [7] T. G. Spiro, R. S. Czernuszewicz, *Methods Enzymol.* **1995**, 246, 416–460.  
 [8] T. Goris, A. F. Wait, M. Saggi, J. Fritsch, N. Heidary, M. Stein, I. Zebger, F. Lenzian, F. A. Armstrong, B. Friedrich, O. Lenz, *Nat. Chem. Biol.* **2011**, 7, 310–318.  
 [9] K. A. Vincent, J. A. Cracknell, O. Lenz, I. Zebger, B. Friedrich, F. A. Armstrong, *Proc. Natl. Acad. Sci. USA* **2005**, 102, 16951–16954.  
 [10] K. Nakamoto, *Infrared and Raman Spectra of Inorganic and Coordination Compounds—Applications in Coordination, Organometallic, and Bioinorganic Chemistry*, 6th ed., Wiley, Hoboken, **2009**.  
 [11] H. S. Shafaat, K. Weber, T. Petrenko, F. Neese, W. Lubitz, *Inorg. Chem.* **2012**, 51, 11787–11797.  
 [12] M. G. Galinato, C. M. Whaley, N. Lehnert, *Inorg. Chem.* **2010**, 49, 3201–3215.  
 [13] C. J. Stromberg, C. L. Kohnhorst, G. A. Van Meter, E. A. Rakowski, B. C. Caplins, T. A. Gutowski, J. L. Mehalko, E. J. Heilweil, *Vib. Spectrosc.* **2011**, 56, 219–227.  
 [14] T. G. Spiro, R. S. Czernuszewicz, S. Han in *Biological Applications of Raman Spectroscopy*, Vol. 3, (Ed.: T. G. Spiro), Wiley, New York, **1988**, pp. 523–553.  
 [15] Y. Rippers, M. Horch, P. Hildebrandt, I. Zebger, M. A. Mroginski, *ChemPhysChem* **2012**, 13, 3852–3856.  
 [16] S. Kamali, H. Wang, D. Mitra, H. Ogata, W. Lubitz, B. C. Manor, T. B. Rauchfuss, D. Byrne, V. Bonnefoy, F. E. Jenney, M. W. W. Adams, Y. Yoda, E. Alp, J. Zhao, S. P. Cramer, *Angew. Chem.* **2013**, 125, 752–756; *Angew. Chem. Int. Ed.* **2013**, 52, 724–728.  
 [17] M. Saggi, I. Zebger, M. Ludwig, O. Lenz, B. Friedrich, P. Hildebrandt, F. Lenzian, *J. Biol. Chem.* **2009**, 284, 16264–16276.  
 [18] M. Brecht, G. M. van, T. Buhrke, B. Friedrich, W. Lubitz, *J. Am. Chem. Soc.* **2003**, 125, 13075–13083.  
 [19] M. E. Pandelia, P. Infossi, M. Stein, M. T. Giudici-Ortoni, W. Lubitz, *Chem. Commun.* **2012**, 48, 823–825.  
 [20] C. Fichtner, M. van Gestel, W. Lubitz, *Phys. Chem. Chem. Phys.* **2003**, 5, 5507–5513.  
 [21] G. J. Kubas, *Chem. Rev.* **2007**, 107, 4152–4205.



## **8 Resonance Raman Spectroscopic Analysis of the [NiFe] Active Site and the Proximal [4Fe-3S] Cluster of an O<sub>2</sub>-tolerant Membrane-bound Hydrogenase in the Crystalline State**

In this work the same approach used in the previous publication about RR spectra experiments and computations<sup>[44]</sup> was employed to study the active site states of the oxidized MBH based on the oxidized x-ray crystallographic structure of this enzyme<sup>[9]</sup> published in 2014. In addition vibrational calculations were performed on the proximal cluster of the superoxidized MBH. Comprehensive statistical analysis of Raman spectra recorded at varying conditions enabled the identification of different components which could be assigned to different enzyme states and cofactors of the MBH by means of QM/MM calculated Raman spectra. The work confirmed the presence of a hydroxyl ligand at the iron sulfur cluster which had also been detected in the crystal structure of the oxidized enzyme<sup>[9]</sup>. Furthermore, active site signals could be assigned to the  $Ni_a - S$  active state (see figure 1.3) of the MBH.

# Resonance Raman Spectroscopic Analysis of the [NiFe] Active Site and the Proximal [4Fe-3S] Cluster of an O<sub>2</sub>-Tolerant Membrane-Bound Hydrogenase in the Crystalline State

Elisabeth Siebert,<sup>†,‡</sup> Yvonne Rippers,<sup>†,‡</sup> Stefan Frielingsdorf,<sup>†</sup> Johannes Fritsch,<sup>†</sup> Andrea Schmidt,<sup>¶</sup> Jacqueline Kalms,<sup>¶</sup> Sagie Katz,<sup>†</sup> Oliver Lenz,<sup>†</sup> Patrick Scheerer,<sup>¶</sup> Lars Paasche,<sup>†</sup> Vladimir Pelmeshnikov,<sup>§</sup> Uwe Kuhlmann,<sup>†</sup> Maria Andrea Mroginski,<sup>†</sup> Ingo Zebger,<sup>\*,†</sup> and Peter Hildebrandt<sup>\*,†</sup>

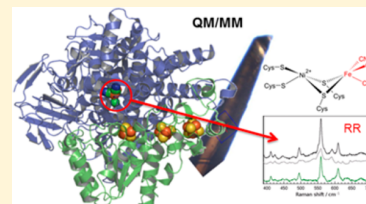
<sup>†</sup>Technische Universität Berlin, Institut für Chemie, Sekr. PC14, Straße des 17. Juni 135, D-10623 Berlin, Germany

<sup>¶</sup>Charité – Universitätsmedizin Berlin, Institut für Medizinische Physik und Biophysik (CC2), Group Protein X-ray Crystallography and Signal Transduction, Charitéplatz 1, D-10117 Berlin, Germany

<sup>§</sup>Technische Universität Berlin, Institut für Chemie, Sekr. C7, Straße des 17. Juni 135, D-10623 Berlin, Germany

## S Supporting Information

**ABSTRACT:** We have applied resonance Raman (RR) spectroscopy on single protein crystals of the O<sub>2</sub>-tolerant membrane-bound [NiFe] hydrogenase (MBH from *Ralstonia eutropha*) which catalyzes the splitting of H<sub>2</sub> into protons and electrons. RR spectra taken from 65 MBH samples in different redox states were analyzed in terms of the respective component spectra of the active site and the unprecedented proximal [4Fe-3S] cluster using a combination of statistical methods and global fitting procedures. These component spectra of the individual cofactors were compared with calculated spectra obtained by quantum mechanics/molecular mechanics (QM/MM) methods. Thus, the recently discovered hydroxyl-coordination of one iron in the [4Fe-3S] cluster was confirmed. Infrared (IR) microscopy of oxidized MBH crystals revealed the [NiFe] active site to be in the Ni<sub>i</sub>-B [Ni(III)] and Ni<sub>i</sub>-S [Ni(II)] states, whereas RR measurements of these crystals uncovered the Ni<sub>a</sub>-S [Ni(II)] state as the main spectral component, suggesting its in situ formation via photodissociation of the assumed bridging hydroxyl or water ligand. On the basis of QM/MM calculations, individual band frequencies could be correlated with structural parameters for the Ni<sub>a</sub>-S state as well as for the Ni-L state, which is formed upon photodissociation of the bridging hydride of H<sub>2</sub>-reduced active site states.



## INTRODUCTION

Functioning of many redox enzymes is based on fine-tuned interaction between various cofactors that serve either as catalytic centers or electron-transfer components. The complex interplay between the different cofactors requires an optimized spatial arrangement and a specifically adapted protein environment required for the adjustment of individual redox potentials. A prominent example of a redox enzyme with multiple metal cofactors is [NiFe] hydrogenase, which catalyzes the reversible cleavage of dihydrogen into protons and electrons.<sup>1–4</sup> Particularly the oxygen-tolerant representatives of this enzyme family, such as the membrane-bound [NiFe] hydrogenase (MBH) from *Ralstonia eutropha*, have been the focus of intense research for several decades because they contain an unprecedented metal cofactor complement and show great promise for application in hydrogen conversion technologies.<sup>3</sup> However, a comprehensive understanding of the reaction mechanism has yet to be achieved.

The MBH is a heterodimeric protein, consisting of a large subunit (HoxG), harboring the [NiFe] active site, and a small subunit (HoxK), which contains three iron–sulfur (FeS) clusters constituting an electron relay that channels electrons from and to the active site.<sup>5,6</sup> The active site is composed of Ni

and Fe ions coordinated by four cysteine residues, with two of them bridging the two metals (Figure 1). The third bridging position is usually occupied by a hydride during catalysis or a hydroxyl group in the inactive oxidized enzyme.<sup>4</sup> In addition, two CN<sup>−</sup> and one CO ligands are coordinated to the Fe site.

For a long time, it has been thought that the three FeS clusters function solely as a unidirectional electron relay. More recently it has been shown that the FeS cluster located ~11 Å proximal to the [NiFe] site in MBH differs from the standard cubic [4Fe-4S] clusters found in anaerobically working enzymes.<sup>5–8</sup> The [4Fe-3S] core of the proximal cluster is coordinated by six instead of four cysteines, which allows the cluster to mediate two redox transitions at physiological potentials instead of only one performed by conventional cubic [4Fe-4S] clusters. This feature plays a critical role in rapid reactivation of the oxidized [NiFe] site under H<sub>2</sub>-turnover conditions.<sup>3,9–12</sup>

**Special Issue:** Wolfgang Lubitz Festschrift

**Received:** April 29, 2015

**Revised:** June 22, 2015

**Published:** July 23, 2015

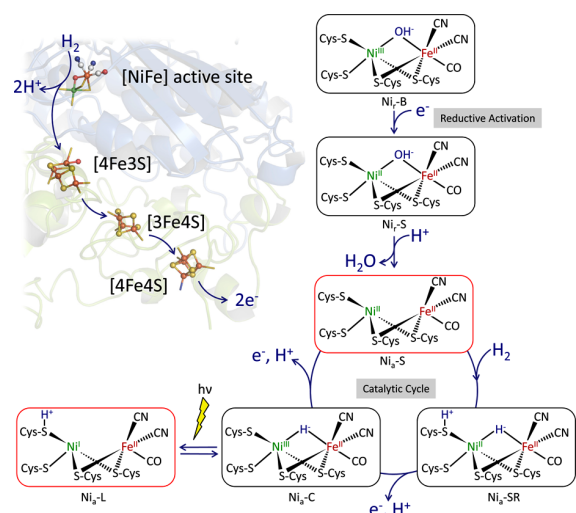


**Figure 1.** Cofactor arrangement and active site states of *R. eutropha* MBH. The large subunit (pale blue) harbors the [NiFe] active site, and the small subunit (pale green) carries three different FeS clusters. Relevant [NiFe] active site configurations are depicted schematically. The RR-active  $\text{Ni}_a\text{-L}$  and  $\text{Ni}_a\text{-S}$  states are highlighted with red boxes.

To advance our understanding of the interplay between the MBH cofactors during catalysis, crystallographic analyses need to be accompanied by spectroscopic and theoretical investigations. This applies in particular to those states of the enzyme that are so far not accessible to protein X-ray crystallography. Resonance Raman (RR) spectroscopy is an efficient tool here because it directly probes metal–ligand bonding and provides new valuable insights into structural and mechanistic details of cofactors.<sup>13,14</sup>

Only recently, the RR technique has been successfully applied to [NiFe] hydrogenases. Despite a low resonance enhancement, RR bands of modes including Fe–CO and Fe–OH coordinates have been observed for the  $\text{H}_2$ -reduced [NiFe] center and the superoxidized  $[\text{4Fe-3S}]^{5+}$  cluster of the MBH, respectively.<sup>6,15</sup> The corresponding Fe–CO and Fe–CN modes were identified also for the oxidized and reduced [NiFe] active site of the regulatory hydrogenase (RH) from *R. eutropha*.<sup>16</sup> All these modes are located in the same frequency range between 450 and 650  $\text{cm}^{-1}$ , and this holds true for all detectable redox states of the active site. This spectral region is well-separated from that of the much more RR-active Fe–S stretching modes of FeS clusters ( $<420 \text{ cm}^{-1}$ ) and, importantly, contains marker bands of all catalytically relevant cofactors of the MBH and [NiFe] hydrogenases in general.<sup>6,15–17</sup>

In continuation of our previous studies, we have now focused on the RR spectroscopic analysis of the MBH. For this enzyme, appropriate protein crystals are available, which provided the basis for the methodological approach of the present work. The main objective was to disentangle the key spectral region between 450 and 650  $\text{cm}^{-1}$  in terms of contributions of the different redox states of both the [NiFe] active site and the novel [4Fe-3S] cluster. The study was carried out with MBH crystals grown either aerobically or under a  $\text{H}_2$ -containing atmosphere, representing the first comprehensive RR spectroscopic analysis of hydrogenase crystals. The approach offers the unique advantage that the individual cofactor spectra (component spectra) derived from the analysis originate from the same states to which the crystallographic models refer and

which serve as the basis for advanced theoretical methods. The comparison of experimental RR spectra with calculated spectra, obtained by quantum mechanics/molecular mechanics (QM/MM) hybrid methods, allows for a reliable determination of the structure and electronic configuration of various cofactor states and may further support a structural refinement of the crystallographic models.<sup>15</sup>

## MATERIALS AND METHODS

**Materials.** Purification of the heterodimeric MBH from *R. eutropha* H16 has been described previously.<sup>10,18</sup> The crystals were grown either in ambient air or under reducing conditions (in a glovebox filled with a  $\text{H}_2/\text{N}_2$  mixture), as reported previously.<sup>5,6</sup> In addition, samples were investigated that were first reduced with  $\text{H}_2$  and then reoxidized by incubation with air. Typical dimensions of single crystals were ca.  $1.4 \times 0.3 \times 0.3 \text{ mm}^3$ .

**Infrared Microscopy.** Infrared (IR) spectra of oxidized MBH crystals were measured using a Bruker Tensor 27 FT-IR spectrometer connected to a Hyperion 2000 IR microscope equipped with a 20 $\times$  attenuated total reflection (ATR) objective that is optimized for a circular probe area with a diameter of 100  $\mu\text{m}$ . The position of the crystalline sample was aligned to the center of the ATR element using the visible mode of the microscope. The sample, which was placed on a Peltier-cooled brass plate for temperature control (8  $^\circ\text{C}$ ), was continuously purged with water-saturated  $\text{N}_2$  precooled at 5  $^\circ\text{C}$ . Contact between the sample and the ATR surface was controlled via an internal pressure sensor and monitored on the basis of the amide I and II band intensities in the spectrum. This setup allowed long-term IR measurements on one single MBH crystal for at least 3 days.

**Resonance Raman Spectroscopy.** RR spectra were measured using a confocal Raman spectrometer (LabRam HR-800, Jobin Yvon) coupled to a liquid nitrogen cooled charge-coupled device (CCD). The spectral resolution was limited by the wavenumber increments per pixel of the CCD camera, corresponding to ca. 0.8, 1.0, and 1.3  $\text{cm}^{-1}$  for excitation wavelengths at 568, 514, and 458 nm, respectively. The laser beam (Kr or Ar ion laser) was focused on the sample surface by a Nikon 20 $\times$  objective with a working distance of 20.5 mm and a numeric aperture of 0.35. The laser power at the sample was set to 1–2 mW, and the sample temperature was kept at 79 K using a Linkam THMS600 freezing microscope stage. Accumulation times were 120–300 s, with up to 30 repetitions. The  $c$ -axis of the MBH crystals was always aligned parallel to the electric field vector of the laser beam with a spot size of ca. 4  $\mu\text{m}$ .

**Data Analysis.** Subtractions of linear baselines and numerical integrations of the measured RR spectra were carried out with GNU Octave. As an additional calibration check, we used the 274  $\text{cm}^{-1}$  of ice as an internal reference. Baseline subtraction, band fitting, and component analyses were performed with homemade software. For the statistical analyses, the calibrated and background-corrected spectra were normalized to the area between 325 and 375  $\text{cm}^{-1}$ .

At the positions of 19 bands between 380 and 640  $\text{cm}^{-1}$  and the phenylalanine band at 1005.0  $\text{cm}^{-1}$ , the integral in the limits of  $\pm 1 \text{ cm}^{-1}$  at each selected wavenumber was calculated numerically with GNU Octave. The cross-correlation between all pairs of the selected wavenumbers (variables) of the resulting 65  $\times$  20 matrix is described by Spearman's rank correlation coefficients,  $\rho_S$ , in a 20  $\times$  20 matrix. We chose to

determine Spearman's rank correlation coefficient,  $\rho_S$ , in contrast to the widely used Pearson's rank correlation coefficient because  $\rho_S$  is a parameter-free measure of how well the statistical relation between two variables (wavenumbers) can be described by a monotonic but not necessarily linear function. A value for  $\rho_S = 1$  implies a strictly monotonically increasing function describing the relation between two highly correlated variables (wavenumbers), whereas a value of  $\rho_S = 0$  corresponds to noncorrelated variables.

In practice, these limiting cases are not observed because intensities at the selected wavenumbers are associated with errors due to the overlap of adjacent bands as well as to variations in the baseline corrections and signal-to-noise ratios among the individual spectra. As a consequence, variables with a  $\rho_S$  of down to 0.5 may be considered as yet moderately correlated.

**Quantum Mechanics/Molecular Mechanics Calculations.** The QM/MM calculations followed the same protocol as described previously for the H<sub>2</sub>-reduced MBH.<sup>15</sup> Here we have used the coordinates of the oxidized enzyme (PDB entry 4IUC)<sup>5,6</sup> and prepared the protein for subsequent energy minimization by addition of protons and hydrogens. After a 5 ns molecular dynamics (MD) equilibration, QM/MM calculations were carried out on 10 different snapshots taken from the MD production run. Depending on the metal center of interest, two QM/MM partitions were defined. The first QM/MM partition embodies the proximal [4Fe-3S] cluster including the six cysteine residues coordinated to the irons, the His229 in the vicinity of Fe1, as well as two water molecules located within a 5 Å distance from the cluster. The QM region of the second QM/MM partition includes the Ni-Fe active site containing the side chains of the Cys75, Cys78, Cys597, and Cys600 coordinated to the Fe and the neighboring Arg530, Thr553, and His82 residues (see Figure S2). In the QM setup, the BP86 functional and the 6-31g(d) basis set were used for all atoms except the Ni and Fe transition metals, for which the TZVP basis set was employed. The proximal [4Fe-3S] cluster was modeled with the broken symmetry (BS) state BS12 as suggested in previous density functional theory calculations on this cluster.<sup>6,19</sup> BS12 corresponds to a spin state where the local spin of the Fe1 and Fe2 sites is oriented oppositely to the total spin of the cluster, which is  $S = 1/2$  in the [4Fe-3S]<sup>3+</sup> superoxidized state.<sup>8</sup> The MM part was treated using the CHARMM 22 force field. The QM/MM geometry optimizations involved all atoms contained in a 15 Å sphere centered at the Fe atom of the active site and at Fe1 atom of the proximal cluster, respectively. The normal modes of vibration of the QM regions were computed following the strategy published by Mrogiński et al. without scaling of the calculated frequencies.<sup>20</sup>

## RESULTS AND DISCUSSION

Most of the IR and RR spectroscopic experiments were carried out with crystals of as-isolated (superoxidized), heterodimeric MBH, to which also the QM/MM calculations refer. For statistical purposes and to compare the crystal-derived data with data obtained with enzyme in solution, RR spectra were taken from as-purified MBH. Further measurements were carried out with crystals of H<sub>2</sub>-reduced MBH.

**Infrared Spectroscopy of MBH Crystals.** The specific state of the [NiFe] center is most conveniently determined on the basis of the CO and CN stretching frequencies of the diatomic ligands bound to the Fe, which can readily be probed

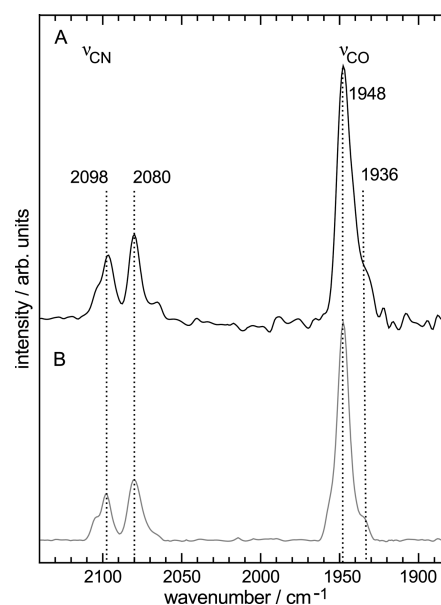


**Figure 2.** Comparison of the IR spectra of *R. eutropha* MBH in its as-isolated, superoxidized form recorded (A) from a single crystal and (B) in solution. The spectral region between 2140 and 1880 cm<sup>-1</sup>, which is characteristic for the stretching modes of the CN<sup>-</sup> and CO ligands bound to Fe of the active site, is shown. Both spectra reveal comparable relative band intensities for the Ni<sub>i</sub>-B state as the main component (2098 cm<sup>-1</sup>, 2080 cm<sup>-1</sup> [ $\nu(\text{C}\equiv\text{N})$ ], and 1948 cm<sup>-1</sup> [ $\nu(\text{C}\equiv\text{O})$ ]) and minor contributions of a Ni(II) redox state (CO absorption at 1936 cm<sup>-1</sup>).

by IR spectroscopy.<sup>2</sup> In this work, we employed for the first time IR microscopy to probe the ligand stretching modes in a single hydrogenase crystal, which could be also analyzed by RR spectroscopy (vide infra). A representative example is shown in Figure 2A, revealing essentially the same spectrum as for the as-isolated (superoxidized) enzyme in solution (Figure 2B). In view of the good agreement of the two spectra, crystallization artifacts such as packing defects seem to have no effect on the architecture and reactivity of the catalytic center. In addition, both spectra show a comparable ratio of two redox states as confirmed by quantitative analysis based on the integral absorbance of the CO stretching. The major fraction, which amounts to 83% and 90% in the crystalline and solution state, respectively, can be attributed to the Ni<sub>i</sub>-B state, in which a hydroxyl ligand bridges the Ni(III) and the Fe(II) ion (Figure 1).<sup>6</sup> The minor contribution originates from an electron paramagnetic resonance-silent Ni(II) species, which has been already observed in previous studies on the MBH.<sup>9,18</sup> According to previous suggestions,<sup>21</sup> it might be a “ready” species (Ni<sub>i</sub>-S) with either a hydroxyl or a water molecule in the bridging position. An alternative assignment might be a structure with an open coordination site between Fe(II) and Ni(II), designated as “active” Ni<sub>i</sub>-S state (Figure 1). This state is supposed to be a central intermediate of the catalytic cycle capable of binding H<sub>2</sub> and O<sub>2</sub> in a competitive manner.<sup>10,11</sup> However, the formation of a Ni<sub>i</sub>-S species would be in line with the presumed reactivity of the Ni<sub>i</sub>-S state toward O<sub>2</sub> and the two crystal structures (PDB entries 4IUB and 4IUC) of superoxidized MBH, which indicate full occupancy of the bridging position by an oxygen species.<sup>6</sup> We consider therefore the assignment to a Ni<sub>i</sub>-S species as rather likely.

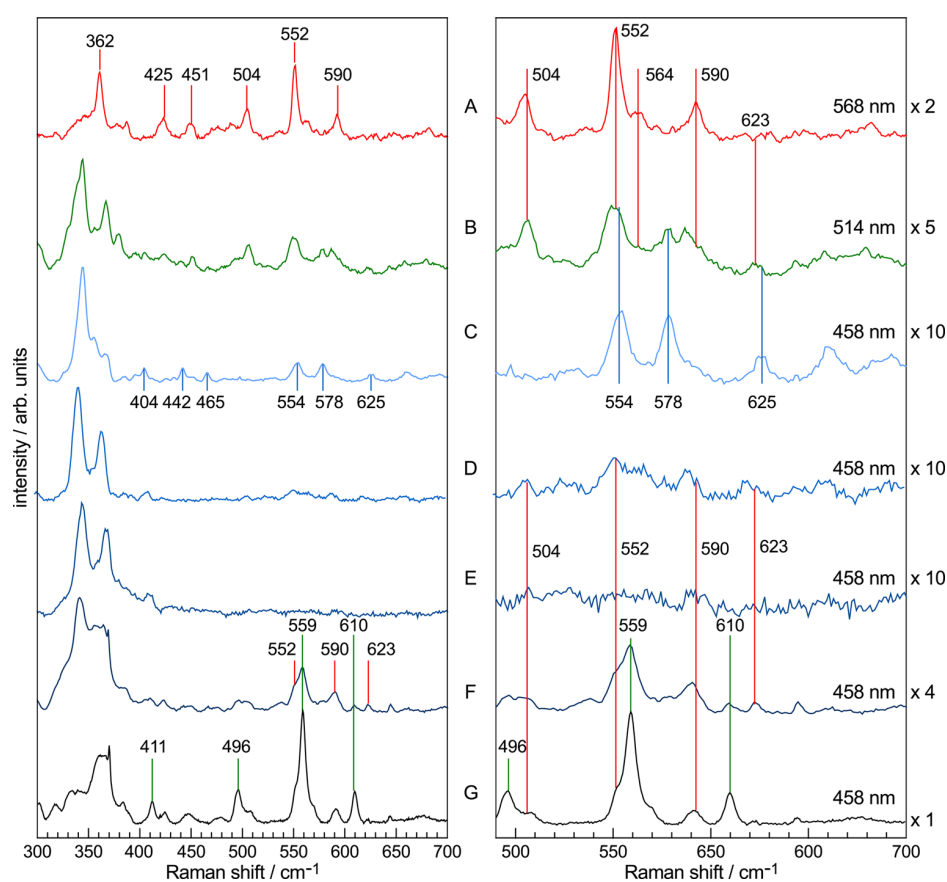


**Figure 3.** Experimental RR spectra of single crystals of as-isolated *R. eutropha* MBH, measured at excitation wavelength of (A) 568, (B) 514, and (C) 458 nm. The spectral region between 490 and 700  $\text{cm}^{-1}$  is expanded by the use of different intensity scaling factors indicated in the right panel to illustrate the effect of the excitation wavelength on selected bands. Traces D, E, and F represent spectra obtained with 458 nm excitation from other crystals but originating from the same protein preparation, demonstrating inherent spectral variations. Trace G shows a spectrum of a  $\text{H}_2$ -reduced single MBH crystal for comparison.<sup>15</sup>

**Resonance Raman Spectroscopy of MBH Crystals.** The RR spectra of oxidized MBH crystals, measured with 458 nm excitation, are dominated by bands between 300 and 400  $\text{cm}^{-1}$ , primarily due to Fe–S stretching modes originating from the FeS clusters (Figure 3). The Fe–CO and Fe–CN modes of the [NiFe] active site are expected to be in the range between 400 and 700  $\text{cm}^{-1}$ , which also contains the Fe–OH modes of the [4Fe-3S] cluster.<sup>6,22</sup> To discriminate between the vibrational bands originating from different cofactors, RR spectra were recorded at different excitation wavelengths, taking advantage of the cofactor-specific electronic transitions that control the enhancement of the Raman bands. Specifically, oxidized FeS clusters display charge-transfer transitions between 400 and 500 nm,<sup>13</sup> whereas electronic transitions associated with the Fe–CN or Fe–CO entities are expected to take place at longer wavelengths.<sup>17,22–24</sup> Accordingly, we note substantial differences in the vibrational band patterns of the spectra measured at 458 and 568 nm (Figure 3). The latter spectrum (Figure 3A) displays distinct bands at 362, 425, 451, 504, 552, 564, and 590  $\text{cm}^{-1}$ , whereas upon decreasing the excitation wavelength, the intensities of these bands decrease (e.g., 514 nm; Figure 3B) until they can hardly be detected anymore at 458 nm (Figure 3C). Thus, this set of bands cannot originate from the FeS clusters but is likely to originate from the [NiFe] active site of the MBH, preliminarily denoted as Ni-X. Conversely, the distinct bands at 404, 442, 465, 554, 578, and 625  $\text{cm}^{-1}$  of the

458 nm spectrum contribute only weakly to the 514 nm spectrum and cannot be detected upon 568 nm excitation. This suggests an assignment of the latter set of bands to another species. On the basis of previously detected Fe–OH vibrations at 554 and 578  $\text{cm}^{-1}$ , we assign these vibrational modes to the [4Fe-3S] cluster.<sup>6</sup>

However, particularly the spectra obtained with 458 nm excitation display considerable variations, even when comparing crystals of the same MBH preparation (Figure 3C–E). The bands at 554 and 578  $\text{cm}^{-1}$  in spectrum C are not visible in spectra D and E, and in spectrum E, essentially no bands can be detected in the region between 490 and 700  $\text{cm}^{-1}$ . These changes are accompanied by spectral alterations in the lower-frequency region between 300 and 400  $\text{cm}^{-1}$ , implying that they are at least partly related to the FeS clusters. In fact, crystallographic analysis of the as-isolated MBH revealed that the Fe1 coordination site for the hydroxyl ligand of the [4Fe-3S] cluster has only partial occupation in each crystal.<sup>6</sup> The hydroxyl-free [4Fe-3S] cluster species do not contribute to the RR spectrum between 490 and 700  $\text{cm}^{-1}$  but give rise to modified signals in the Fe–S stretching region due to the change in the Fe1 coordination sphere (see Figure 3E). Also, other cofactors, including the [NiFe] active site, may reside in different electronic (and ligation) states as a consequence of subtle deviations in sample preparation and handling, e.g., photoinduced processes due to the excitation laser beam. Thus,

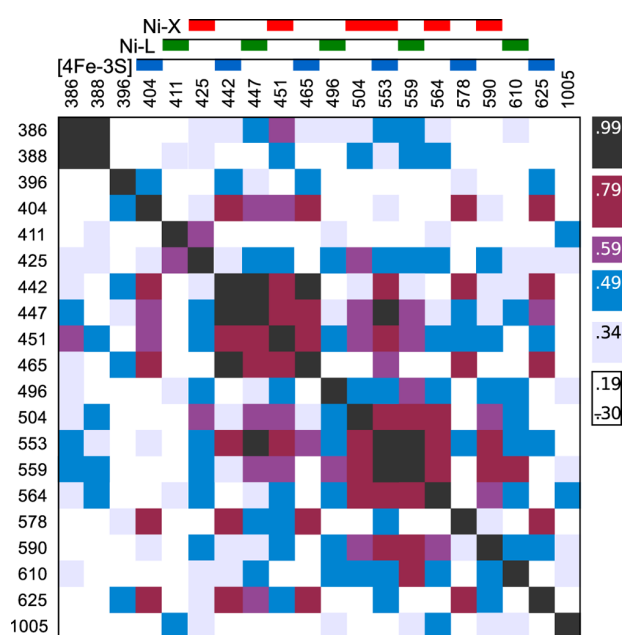


**Figure 4.** Graphical illustration of the calculated Spearman's rank (cross) correlation coefficients between the intensities at selected band positions in the RR spectra of the *R. eutropha* MBH recorded with a 458 nm excitation. Vibrational modes belonging to the [4Fe-3S] cluster, Ni-L, and Ni-X components are labeled at the top of the figure in blue, green, and red, respectively.

even crystals of the as-isolated MBH seem to contain minor contributions from the Ni-L state, recently detected to be photochemically formed in RR experiments of H<sub>2</sub>-reduced MBH crystals.<sup>15</sup> This raises the question of the origin of the electrons required for the corresponding reduction of the as-isolated MBH. One source might be ferricyanide, which is used for full oxidation of the MBH in the course of the purification process, and, in some cases, for crystal preparation. Ferricyanide is known to be easily photodecomposed, leading to products that could induce the reduction of the [NiFe] active site.<sup>25</sup> Indeed, the weak features at 559 and 610 cm<sup>-1</sup> observed for crystals of as-isolated MBH (Figure 3F) presumably result from small contributions of the Ni-L state as evident from the comparison with the RR spectrum of an H<sub>2</sub>-reduced MBH crystal (Figure 3G).<sup>15</sup> In summary, at least three redox species contribute to the RR spectra of oxidized MBH crystals, namely, (1) the superoxidized [4Fe-3S] cluster including the Fe1-bound OH<sup>-</sup> ligand; (2) the photochemically generated Ni-L state, which was detected in only a few samples;<sup>15</sup> and (3) an active site species Ni-X (see below), of yet unknown electronic configuration.

A relatively pure RR spectrum at 458 nm excitation can be directly measured only for the Ni-L species (Figure 3G), whereas only a few bands can be unambiguously assigned to the other two species (vide supra). It is therefore not possible to derive the entire component spectra of the OH<sup>-</sup> harboring [4Fe-3S] cluster and Ni-X solely on the basis of the wavelength-dependent RR spectra. This is because the RR cross sections do not vary uniformly with the excitation line for all bands of a cofactor. For instance, the intensity ratio of the bands at 552 and 504 cm<sup>-1</sup> of Ni-X is ca. 2.0 at 568 nm (Figure 3A), but it drops to nearly 1.0 at 514 nm (Figure 3B).

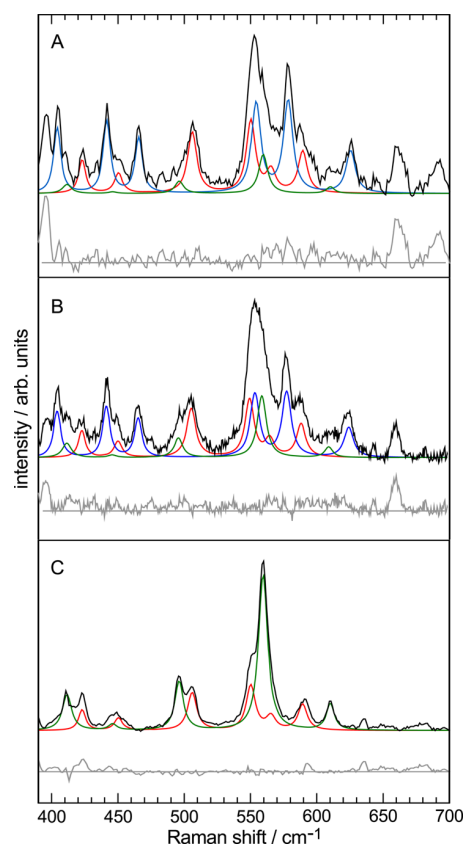


**Figure 5.** Selection of RR spectra of *R. eutropha* MBH crystals, measured with 458 nm excitation. The spectra include the individual component spectra of Ni-X (red), Ni-L (green), and [4Fe-3S] (blue). The residuals (gray) display unassigned bands at 649 and 660 cm<sup>-1</sup> not included in the component spectra. The spectra in traces A and B were obtained from an incompletely reoxidized sample and an as-isolated sample oxidized with additional ferricyanide, whereas trace C shows a spectrum of an incompletely reduced sample, all exhibiting the expected superposition of the reduced and oxidized component of the [NiFe] active site.

### Statistical Analysis of the Resonance Raman Spectra.

To sort out the bands originating from the various cofactors and to identify potential bands derived from the protein matrix, we employed a statistical approach to analyze the RR spectra obtained at 458 nm excitation from a total of 65 samples. The samples included MBH crystals and MBH in solution in the as-isolated and H<sub>2</sub>-reduced states. In this way, spectral contributions from the superoxidized [4Fe-3S] cluster and the active site states Ni-L and Ni-X can be evaluated at the same excitation wavelength. The objective of the statistical approach was to determine correlations between the various bands in the experimental spectra. Because at a given excitation line all bands originating from the same cofactor constitute constant intensity ratios with respect to each other, they are strongly correlated, corresponding to a theoretical cross correlation coefficient of  $\rho_S = 1$ . Conversely, bands originating from different cofactors should, in principle, display no correlation ( $\rho_S = 0$ ).

Upon inspection of the experimental spectra, 19 positions were selected in the range between 380 to 650 cm<sup>-1</sup>, representing bands that were found in several but not necessarily all spectra. Furthermore, we included the position

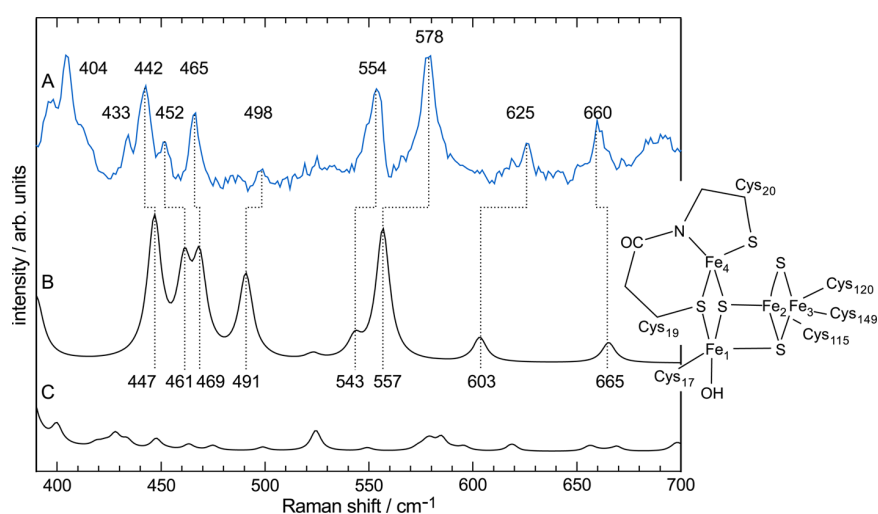


**Figure 6.** (A) Complete component spectrum of the [4Fe-3S] cluster, derived by mutual subtraction of experimental RR spectra measured at 458 nm, compared to the calculated spectrum with (B) and without (C) a bound hydroxyl ligand at Fe1. A simplified structural model of the [4Fe-3S] cluster is shown on the right-hand side.

**Table 1. Experimental RR Bands and Calculated Modes of the [4Fe-3S] Cluster of the MBH**

calcd <sup>a</sup>					exptl <sup>b</sup>			
$\nu$ (cm <sup>-1</sup> )	$I_{rel}$	PED (%) <sup>c</sup>	$\Delta^{18O/16O}$	$\Delta D/H$	$\nu$ (cm <sup>-1</sup> )	$I_{rel}$	$\Delta^{18O/16O}$	$\Delta D/H$
665(2)	16	15 $\nu C-S(19)$	0	0	660	m	0	0
603(3)	16	43 $\nu C-S(19)$	0	0	625	w	0	0
557(7)	96	62 $\nu Fe-OH$	-20	-17	578	vs	-7 <sup>c</sup>	-15
543(5)	16	21 $\nu Fe-OH$	-11	-9	554	s	-22 <sup>c</sup>	-8
		16 $\nu Fe-N$						
		9 $\nu C-S(19)$						
523(4)	4	8 $\nu Fe-OH$	-3	-1	n.d. <sup>c</sup>	n.d. <sup>c</sup>	n.d. <sup>c</sup>	n.d. <sup>c</sup>
491(6)	60	31 $\tau Fe-O$	-3	0	498	vw	0	0
469(4)	64	23 $\tau Fe-O$	-1	0	465	m	0	0
461(5)	60	14 $\tau Fe-O$	-1	0	451	w	0	0
447(4)	100	29 $\tau Fe-O$	-1	0	442	s	0	0

<sup>a</sup>Calculated frequencies include the values for the snapshot-to-snapshot variations in parentheses; relative intensities,  $I_{rel}$ , refer to the most intense mode in this region ( $=100$ ); C-S(19) refers to the C-S stretching coordinate in Cys19; PED, potential energy distribution. <sup>b</sup>Experimental RR band intensities are qualitatively grouped into very strong (vs), strong (s), medium (m), weak (w), and very weak (vw). <sup>c</sup>The stretching and torsional coordinates of individual bonds are denoted by  $\nu$  and  $\tau$ , respectively; n.d., experimentally not detectable.

at 1005 cm<sup>-1</sup> that refers to a phenylalanine mode of the protein matrix. For all these positions, the normalized integrated intensities were determined within an interval of  $\pm 1$  cm<sup>-1</sup> and arranged in a 65  $\times$  20 matrix. The cross-correlations between the intensity of all band pairs of the selected wavenumbers were then described by Spearman's rank correlation coefficient  $\rho_S$  in a 20  $\times$  20 matrix (Figure 4).<sup>26</sup> Cross correlations between closely spaced bands ( $\Delta\nu < 4$  cm<sup>-1</sup>) were not considered because of the mutual perturbation of the intensity at the peak maxima.

The analysis shown in Figure 4 reveals that none of the selected bands is correlated with the phenylalanine mode at 1005 cm<sup>-1</sup>, implying that all other bands considered in the analysis must originate from the various states of the individual cofactors. The bands at 404, 442, 465, and 578 cm<sup>-1</sup> with  $\rho_S > 0.5$  constitute one group that can be readily attributed to the [4Fe-3S] cluster, which is in line with previous results on crystalline MBH.<sup>6</sup> Furthermore, the 625 cm<sup>-1</sup> band seems to belong to this species as well ( $\rho_S = 0.67$ ), though it interferes with a nearby broad band at 623 cm<sup>-1</sup> of yet unknown origin (Figure 3). Two further groups were identified on the basis of

the  $\rho_S$  values. One group, including bands at 447, 495, 559, and 610 cm<sup>-1</sup>, is readily attributed to the Ni-L state, whereas the other group involving the bands at 504, 564, and 590 cm<sup>-1</sup> corresponds to the Ni-X state. As judged by the visual inspection of the spectra in Figure 3A, the latter group also includes the band at 552 cm<sup>-1</sup>, although the corresponding correlation coefficient is below 0.5. This low  $\rho_S$  value, however, is most likely a result of the overlap with a Ni-L-related band at 559 cm<sup>-1</sup> and a band at 554 cm<sup>-1</sup> assigned to the [4Fe-3S] cluster (vide infra).

**Component Spectra of the Cofactor States and Spectra Calculation.** Based on the assignments derived from the statistical analysis and wavelength-dependent measurements, component spectra of the three species [4Fe-3S] cluster, Ni-X, and Ni-L were constructed. Experimental RR spectra that were dominated by only one of these components served as a starting point to generate initial component spectra by conventional band fitting using Lorentzian functions. The initial component spectra were then iteratively refined to achieve a satisfactory global fit to all experimental spectra. Selected examples are shown in Figure 5. The respective

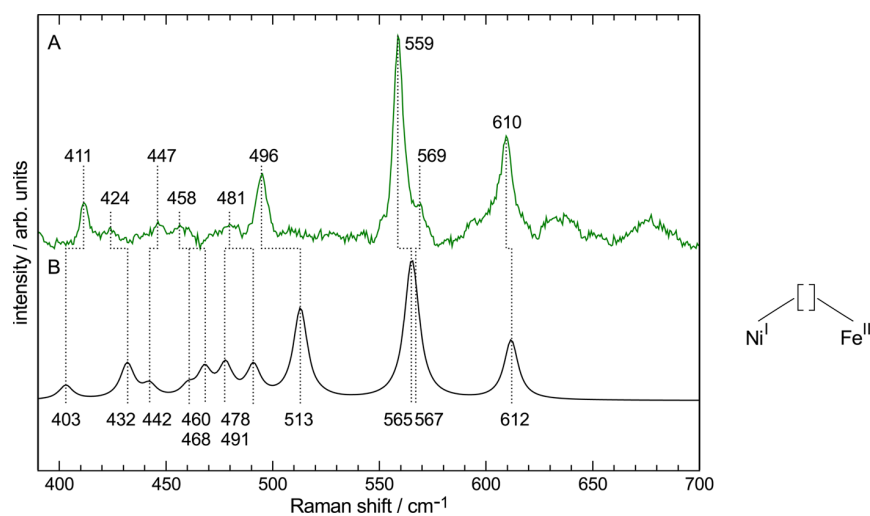


**Figure 7.** (A) Complete component spectrum of the Ni-L state, derived by mutual subtraction of experimental RR spectra measured at 458 nm, compared to the calculated spectrum (black).

**Table 2. Experimental RR Bands and Calculated Modes of the Ni-L State of the MBH and RH from *R. eutropha***

MBH				RH			
calcd <sup>a</sup>				exptl <sup>b</sup>			
$\nu$ (cm <sup>-1</sup> )	$I_{\text{rel}}$	PED (%) <sup>d</sup>	$\Delta^{13}\text{C}/^{12}\text{C}$	$\nu$ (cm <sup>-1</sup> )	$I_{\text{rel}}$	$\Delta^{13}\text{C}/^{12}\text{C}$	exptl <sup>c</sup>
612(2)	50	37 $\nu\text{Fe-CO}$	-7	610	s	-10	602 w
567(1)	25	31 $\nu\text{Fe-CO}$ 8 $\nu\text{Fe-CN}$	-15	569	w	-14	563 m
565(2)	100	25 $\nu\text{Fe-CO}$ 15 $\delta\text{Fe-CN}$ 8 $\delta\text{Fe-CO}$	-10	559	vs	-14	556 vs
513(2)	81	11 $\nu\text{Fe-CO}$ 25 $\delta\text{Fe-CO}$	-14	530	w	-11	503 w
491(3)	25	13 $\nu\text{Fe-CN}$	-6	496	m	-13	
478(2)	25	24 $\nu\text{Fe-CN}$ 7 $\delta\text{Fe-OH}$	-7	481	vw		
468(5)	25	24 $\nu\text{Fe-CN}$	-5	458	w		446 w
460(2)	6	47 $\nu\text{Fe-CN}$	-7				
442(2)	13	20 $\nu\text{Fe-CN}$ 8 $\delta\text{Fe-CO}$	-13	445	s	-10	
432(1)	31	13 $\nu\text{Fe-CN}$ 29 $\delta\text{Fe-CN}$ 15 $\delta\text{Fe-CO}$	-11	424	w		426 m
403(2)	13	6 $\nu\text{Fe-CN}$ 29 $\delta\text{Fe-CN}$	-12	410	m		416 m

<sup>a</sup>Calculated frequencies include the values for the snapshot-to-snapshot variations in parentheses; relative intensities,  $I_{\text{rel}}$ , refer to the most intense mode in this region (=100); PED, potential energy distribution. <sup>b</sup>Experimental RR band intensities are qualitatively grouped into very strong (vs), strong (s), medium (m), weak (w), and very weak (vw); <sup>c</sup>Taken from Horch et al.<sup>16</sup> <sup>d</sup>Stretching and bending coordinates are denoted by  $\nu$  and  $\delta$ , respectively.

residuals display deviations from the noise level essentially only at the positions of those few bands that remained unassigned and were not included in the component spectra. Thus, the component spectra do not correspond to the complete spectra of the cofactors. However, because each component spectrum comprises the most characteristic bands of the respective cofactor, the component analysis provides a reliable determination of the relative spectral weights of the cofactors in the experimental spectra that involve overlapping contributions of the individual species. Once these spectral weights for the

various measurements are known, the complete spectra can be evaluated by mutual subtraction from the experimental spectra.

In the following, these complete component spectra will be used for the structural assignment by comparison with the calculated Raman spectra. The calculated spectra, which were obtained by QM/MM as described previously,<sup>15</sup> represent an average of 10 snapshots taken during the MD simulation process after precedent equilibration. To relate experimental and predicted bands, the most important criteria were the frequency match (taking into account an accuracy for the calculated frequencies of ca.  $\Delta\nu = \pm 10 \text{ cm}^{-1}$  inherent to the

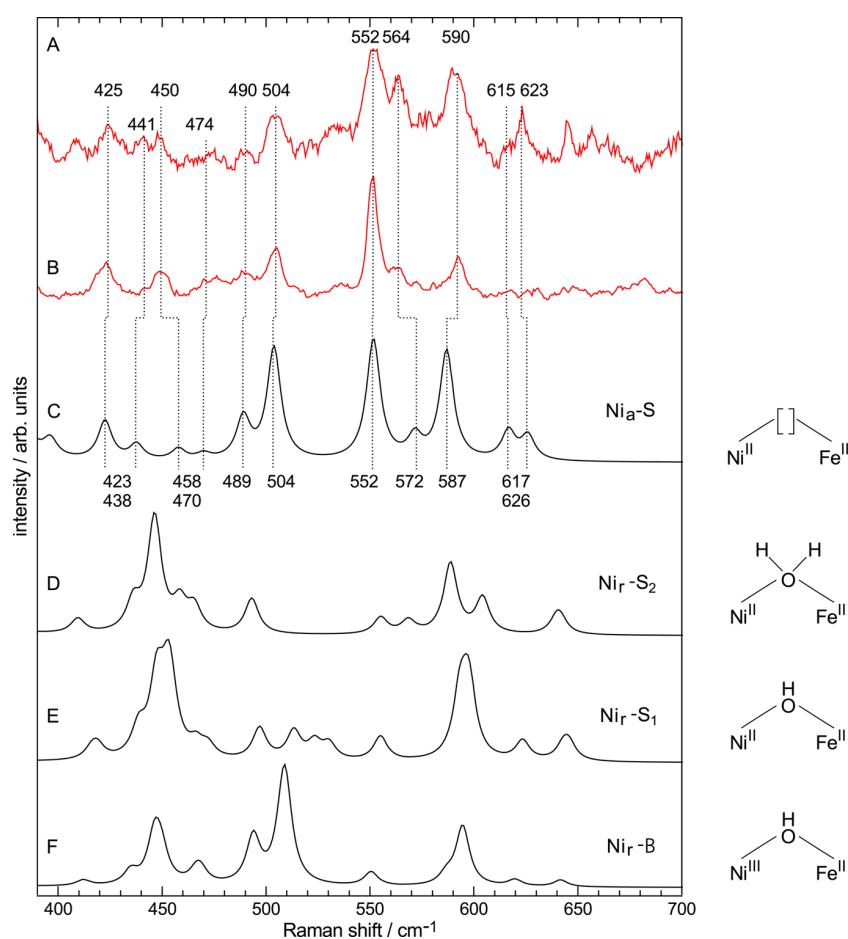


**Figure 8.** (A) Complete component spectrum of the  $[\text{NiFe}]_2$  state, derived by mutual subtraction of experimental RR spectra measured at 458 nm; (B) experimental RR spectrum, obtained from an as-isolated MBH crystal with 568 nm excitation (see Figure 2A); and (C–F) calculated spectra for different oxidation states of Ni and ligation pattern of the dinuclear center (see simplified structures on the right). Only the spectrum calculated for the  $\text{Ni}_a\text{-S}$  state agrees with the experimental spectra.

QM method) and the reproduction of the isotopic shifts. Calculated Raman intensities are expected to provide only a qualitative description for the experimental RR intensities.

While the band assignment is based on the average of 10 calculated snapshot spectra, the individual snapshot spectra were used to identify correlations between the individual modes of the cofactors and specific structural parameters by following a previously published procedure.<sup>27,28</sup> The underlying assumption of this approach is that the character of the modes (potential energy distribution, PED) does not alter significantly from snapshot to snapshot. This prerequisite is fulfilled for the  $[\text{NiFe}]$  center but not for the  $[\text{4Fe-3S}]$  cluster as discussed below.

**Proximal  $[\text{4Fe-3S}]$  Cluster.** The QM model of the  $[\text{4Fe-3S}]$  cluster in the superoxidized state consists of four iron and three inorganic sulfur atoms from the FeS cluster core (Figure 6 and Figure S1). This cluster is coordinated by six cysteine residues (Cys 17, 19, 20, 115, 120, and 149), and the Fe1 carries a hydroxyl group hydrogen bonded to His229, which itself is protonated on  $\text{N}_\tau$ .<sup>6</sup> MD-based structural refinements with alternative protonation states afforded larger deviations from the crystal structure. A special feature of the superoxidized  $[\text{4Fe-3S}]$  cluster is the bond between Fe4 and the backbone nitrogen of Cys20. This bond and two conserved water

molecules in the vicinity of the cluster were also considered in this QM model.

A comparison with the experimental spectrum (i.e., the complete component spectrum) of the  $[\text{4Fe-3S}]$  cluster revealed a satisfactory agreement with a root-mean-square-deviation (rmsd) of  $12.8 \text{ cm}^{-1}$ , which is close to the intrinsic frequency uncertainty of the QM method (ca.  $\Delta\nu = \pm 10 \text{ cm}^{-1}$ ) (Figure 6, Table 1). However, there are some notable deviations that mainly refer to the modes including the Fe–OH stretching coordinates predicted to be at  $543$  and  $557 \text{ cm}^{-1}$ . In a previous study, an experimental RR band of medium intensity at  $578 \text{ cm}^{-1}$  was found to display significant D/H and  $^{18}\text{O}/^{16}\text{O}$  isotopic shifts.<sup>6</sup> Inspection of the RR difference spectra presented in the previous study reveal that also the broad feature at  $554 \text{ cm}^{-1}$  varies upon D/H and  $^{18}\text{O}/^{16}\text{O}$  exchange. Thus, the modes at  $554$  and  $578 \text{ cm}^{-1}$  may tentatively be assigned to the two calculated modes with the most significant Fe–OH stretching character at  $543$  and  $557 \text{ cm}^{-1}$ , respectively (Table 1). However, this assignment is in conflict with calculated the  $^{18}\text{O}/^{16}\text{O}$  shifts that are predicted to be larger for the  $557 \text{ cm}^{-1}$  than for the  $543 \text{ cm}^{-1}$  mode ( $20$  and  $11 \text{ cm}^{-1}$ , respectively), which is in contrast to the experimental data ( $7$  and  $23 \text{ cm}^{-1}$  for the bands at  $578$  and  $554 \text{ cm}^{-1}$ , respectively). We attribute these discrepancies in part to the intrinsic error

**Table 3. Experimental RR Bands and Calculated Modes of the Ni<sub>a</sub>-S State of the MBH and RH from *R. eutropha***

MBH				RH		
calcd <sup>a</sup>		exptl <sup>b</sup>		exptl <sup>c</sup>		
$\nu$ (cm <sup>-1</sup> )	$I_{\text{rel}}$	$\nu$ (cm <sup>-1</sup> )	$I_{\text{rel}}$	$\nu$ (cm <sup>-1</sup> )	$I_{\text{rel}}$	
626(2)	19	37 $\nu$ Fe–CO	623	m		
617(3)	24	12 $\nu$ Fe–CO	615	w	600	w
587(4)	90	12 $\nu$ Fe–CO	590	s		
572(4)	19	6 $\nu$ Fe–CO	564	m	563	m
		9 $\delta$ Fe–CO				
552(4)	100	28 $\delta$ Fe–CO	552	vs	553	vs
		16 $\delta$ Fe–CN				
		6 $\nu$ Fe–CO				
		12 $\nu$ Fe–S(600)				
503(2)	90	8 $\delta$ Fe–CO	504	m	490	m
		22 $\delta$ Fe–CN				
		6 $\nu$ Fe–CO				
		6 $\nu$ Fe–CN				
489(4)	33	12 $\nu$ Fe–CN	490	w		
470(2)	5	46 $\nu$ Fe–CN	474	w		
		8 $\delta$ Fe–CN				
458(2)	10	55 $\nu$ Fe–CN	448	m		
		6 $\delta$ Fe–CN				
438(2)	10	19 $\nu$ Fe–CN	441	w		
		25 $\delta$ Fe–CN				
423(1)	5	6 $\nu$ Fe–CN	425	w	417	w
		26 $\delta$ Fe–CN				
		11 $\delta$ Fe–CO				

<sup>a</sup>Calculated frequencies include the values for the snapshot-to-snapshot variations in parentheses; relative intensities,  $I_{\text{rel}}$  refer to the most intense mode in this region (=100); C–S(600) refers to the C–S stretching coordinate in Cys600; PED, potential energy distribution. <sup>b</sup>Experimental RR band intensities are qualitatively grouped into very strong (vs), strong (s), medium (m), weak (w), and very weak (vw); <sup>c</sup>Taken from Horch et al.<sup>16</sup> <sup>d</sup>Stretching and bending coordinates are denoted by  $\nu$  and  $\delta$ , respectively.

associated with the PED for closely spaced modes. In addition, the calculated modes at 557 and 603 cm<sup>-1</sup>, which are dominated by the Fe–OH and C–S stretching (Cys19) coordinates, respectively, show quite substantial frequency deviations (ca. + 20 cm<sup>-1</sup>) with respect to their experimental counterparts. These deviations may reflect shortcomings of the theoretical method in adequately describing hydrogen-bonded systems involving fluctuating water molecules. This may also be the reason why the PEDs of the modes involving the OH coordinates vary relatively strongly from snapshot to snapshot (Table 1). Therefore, clear correlations between vibrational modes and specific structural parameters can hardly be identified for this cofactor. In fact, such deficiencies are not observed for the [NiFe] center, which does not contain water molecules (vide infra). Note that for the [4Fe-3S] cluster lacking the hydroxyl ligand only very weak bands are predicted in the region between 400 and 700 cm<sup>-1</sup>, consistent with the experimental findings (vide supra).

**[NiFe] Active Site.** As shown previously, the RR spectrum of the H<sub>2</sub>-reduced [NiFe] active site almost exclusively represents the Ni-L state, which is formed photochemically in the course of the RR experiment (Figure 1).<sup>15</sup> The QM model for the Ni-L state of the [NiFe] active site includes the [NiFe] center, the CN<sup>-</sup> and CO ligands, and the coordinating cysteine residues (75, 78, 597, and 600), with Cys597 being

protonated.<sup>15</sup> Furthermore, the model comprises the adjacent amino acids Arg530, Thr553, and His82 (Figure S2). Taking into account that the resonance enhancement is derived from the Fe → CO metal-to-ligand charge-transfer transition, Raman intensities of the individual modes were scaled according to the contributions from the Fe–CO stretching and bending coordinates as described previously.<sup>15</sup> Here, this approximation was extended to the respective Fe–CN coordinates in view of the recent RR-based identification of the Fe–CN containing modes of the regulatory hydrogenase from *R. eutropha*.<sup>16</sup> The calculated spectrum and <sup>13</sup>C/<sup>12</sup>C isotopic shifts are in very good agreement with the experimental RR data, corresponding to a rmsd of 7.3 cm<sup>-1</sup> (Figure 7, Figure S3, Table 2). Even the very weak bands at 530 and 447 cm<sup>-1</sup> can be assigned on the basis of their distinct <sup>13</sup>C/<sup>12</sup>C isotopic shifts, which are in line with the calculations for the reduced crystals (Figure S3, Table 2). The remaining calculated modes at 491, 478, 468, 460, and 432 cm<sup>-1</sup> are correlated with experimental bands solely based on the frequency match, although the assignments are not unambiguous in each case because of close band spacing and the very low RR intensity slightly above the signal-to-noise level.

For the higher oxidized states of the active site, the same QM partition was employed, and the calculations were carried out for different bridging ligands and Ni oxidation states, i.e., for the Ni<sub>r</sub>-B state with Ni(III) and a bridging hydroxyl ligand, the corresponding Ni(II) species Ni<sub>r</sub>-S(I) and Ni<sub>r</sub>-S(II) carrying a water molecule, and finally the Ni<sub>a</sub>-S state without a ligand in the bridging position. In all of these states, the Fe remains in the oxidation state II. In addition, also structures of light-induced intermediate states, which have been suggested by Pandelia et al.,<sup>29</sup> were considered. However, these configurations turned out to be unstable because they converge to Ni<sub>r</sub>-B or Ni<sub>r</sub>-S during the QM/MM optimization. Figure 8 compares the various calculated spectra with the component spectrum obtained at 458 nm and the RR spectrum directly measured at 568 nm, where only the Raman bands of the oxidized active site are enhanced. Clearly, the best agreement with the experimental spectra is achieved by the spectrum calculated for Ni<sub>a</sub>-S, which nicely reproduces the three-banded pattern between 552 and 590 cm<sup>-1</sup> in the experimental spectra and also correctly predicts the doublet at 615 and 623 cm<sup>-1</sup> detectable only at 458 nm. In general, the different relative enhancements of individual bands upon excitation at 458 and 568 nm support these assignments. Thus, most of the bands observed below 500 cm<sup>-1</sup> can be readily correlated with calculated modes, and only few uncertainties remain due to low band intensities. For the assignments in Figure 8 and Table 3, the rmsd is only 4.4 cm<sup>-1</sup>. In contrast, the calculated spectra of all other configurations provide an inferior description of the experimental spectra. This is also true for the IR-detectable Ni<sub>r</sub>-B state, representing the main component (ca. 85%) of the oxidized samples prior to the RR measurements (Figure 2), and the less abundant Ni<sub>r</sub>-S states (ca. 15%).

In the O<sub>2</sub>-sensitive [NiFe] hydrogenase of *Desulfovibrio vulgaris* Miyazaki F, the Ni<sub>r</sub>-S state was shown to undergo light-induced reactions at 40 K, with an efficiency that increases by a factor of 2 from 458 to 568 nm.<sup>29</sup> This wavelength dependence of the photoconversion matches the present results inasmuch as a substantially more intense RR spectrum was obtained at 568 nm than at 458 nm excitation (Figure 3). However, the photoproducts proposed by the authors, such as a Ni(II)-SL state with a hydroxyl ligand only coordinated to the Ni, were

Table 4. Correlations between RR Bands of the Ni-L and Ni<sub>s</sub>-S States of MBH with Structural Parameters of the Active Sites

exptl	marker bands of Ni-L (cm <sup>-1</sup> )			marker bands of Ni <sub>s</sub> -S (cm <sup>-1</sup> )					
	612	567	565	513	626	587	572	552	504
PED <sup>a</sup>	37 $\nu$ Fe-CO	31 $\nu$ Fe-CO 8 $\nu$ Fe-CN	25 $\nu$ Fe-CO 15 $\delta$ Fe-CN 8 $\delta$ Fe-CO	11 $\nu$ Fe-CO 25 $\delta$ Fe-CO	37 $\nu$ Fe-CO	12 $\nu$ Fe-CO	6 $\nu$ Fe-CO 9 $\delta$ Fe-CO	28 $\delta$ Fe-CO 16 $\delta$ Fe-CN 6 $\nu$ Fe-CO 12 $\nu$ Fe-S(600)	8 $\delta$ Fe-CO 22 $\delta$ Fe-CN 6 $\nu$ Fe-CO 6 $\nu$ Fe-CN
structural parameters									
Ni-SS97 <sup>b</sup>			negative	negative					negative
Ni-S600 <sup>b</sup>					negative				
Fe-S600 <sup>b</sup>						negative		negative	
Fe-Ni <sup>b</sup>		negative	negative	positive		negative			
Fe-CN <sup>b</sup>				negative					
C-O <sup>b</sup>	negative								
SS97-H <sup>b</sup>	positive	positive	positive	positive					
S78-Ni-S75 <sup>c</sup>	negative								
Ni-S600-Fe <sup>c</sup>				positive					
Fe-C-O <sup>c</sup>					positive				
Fe-C-N <sup>c</sup>					negative				negative
NC:Fe-CO <sup>c</sup>			negative	negative					

<sup>a</sup>PED (potential energy distribution) of the calculated modes; contributions of the stretching ( $\nu$ ) and bending coordinates ( $\delta$ ) are given in percentages. <sup>b</sup>Bond distances. <sup>c</sup>Bond angles. The correlations are classified as "positive" or "negative". Further abbreviations: S(597), S(600), S(78), and S(75) refer to the S atom of the respective Cys residues.

discarded in this study because of their instability in the QM/MM calculations (vide supra). Instead, the comparison of the experimental and the calculated spectra strongly favors the assignment to the Ni<sub>a</sub>-S state, whereas the Ni<sub>r</sub>-B and Ni<sub>r</sub>-S states are obviously not RR-active. This conclusion further implies that in the RR experiments the high photon flux of the probe laser causes the dissociation of the hydroxyl or water ligand from the bridging position of either the Ni<sub>r</sub>-B or Ni<sub>r</sub>-S state.

Photoconversion of the Ni<sub>r</sub>-B state requires both the Ni(III)-to-Ni(II) reduction and the removal of the hydroxyl ligand from the bridging position. It might be that both events are caused by the probe laser, although the Ni(III) state was found to be largely photostable in a previous study on the [NiFe] hydrogenase of *D. vulgaris* Miyazaki F.<sup>30,31</sup> However, there are indications for an increased photolability of Ni<sub>r</sub>-B in O<sub>2</sub>-tolerant hydrogenases. For the [NiFe] hydrogenase I of *Aquifex aeolius*, for instance, light-induced reactivation of the enzyme has been detected under turnover conditions at high potentials, which was tentatively explained by photoinduced hydroxyl ligand removal from Ni<sub>r</sub>-B to afford the Ni<sub>a</sub>-S state.<sup>32</sup> Such a process might in principle also take place in MBH during the RR experiments. Moreover, locally enriched ferricyanide present in some of the MBH crystals may further enhance the photodissociation of Ni<sub>r</sub>-B, even yielding the reduced Ni-L species (vide supra).

The photoconversion from the Ni<sub>r</sub>-S to the Ni<sub>a</sub>-S state, in contrast, solely requires the laser-induced dissociation of the bridging ligand, whereby the oxidation state of the Ni(II) remains unchanged. Thus, the 15–20% fraction of Ni<sub>a</sub>-S in as-isolated MBH is the most plausible origin for the Ni<sub>a</sub>-S state detected in the RR experiments. Note that the RR spectra solely reflect the existence of RR-active states and do not allow conclusions about the quantitative distribution among the various active site states in the samples.

**Identification of Structure-Sensitive Marker Bands of the [NiFe] Active Site.** The Ni-L and Ni<sub>a</sub>-S states giving rise to the RR spectra displayed in Figures 7 and 8 possess the same ligation pattern. The position of the exchangeable bridging ligand is not occupied, but the states differ by the oxidation state of the Ni and protonation state of one of the terminal cysteine(s). Thus, the differences between the RR spectra of Ni-L and Ni<sub>a</sub>-S reflect the different charge distribution in the [NiFe] center and the consequences on its geometry. These structural differences between the two states are likely to be relatively small because the vibrational band patterns of Ni-L and Ni<sub>a</sub>-S are quite similar. In both states, the most prominent bands originate from modes including the Fe–CO stretching and bending coordinates, thereby confirming earlier conclusions that resonance enhancement is mainly derived from a Fe–CO charge-transfer transition.<sup>15</sup> In addition, the weaker Fe–CN stretching and bending modes can be monitored and assigned by this spectroscopic technique.

However, the correlations between the individual mode frequencies with specific structural parameters of the catalytic center, which were derived from the snapshot calculations (vide supra), are different for Ni-L and Ni<sub>a</sub>-S. The most striking difference is the complementarity of the correlations, i.e., those structural parameters that are correlated with vibrational modes of Ni-L do not vary with the modes of Ni<sub>a</sub>-S and vice versa (Table 4). In addition, for the Ni<sub>a</sub>-S state, the number of notable correlations is much smaller than for Ni-L. Except for the Ni–S(Cys600) distance, the vibrational modes of Ni<sub>a</sub>-S

correlated with structural parameters of the ligation sphere of the Fe, displaying negative correlation coefficients with the Fe–C–N bond angle and the Fe–S(Cys600) distance and positive ones with the Fe–C–O bond angle.

The correlations in the Ni-L state comprise coordinates of the entire active site. They involve negative correlations with C–O, Fe–CN, and Ni–S(Cys600) bond distances and NC–Fe–CO and S(78)–Ni–S(75) bond angles, as well as positive correlations with S(597)–H and Fe–Ni bond distances and the Ni–S(600)–Fe bond angle. Interestingly, in both states, the correlations refer to coordinates that provide only small contributions to the respective normal modes. Conversely, there is no correlation of Ni-L and Ni<sub>a</sub>-S with the Fe–CO bond distance, although the Fe–CO stretching coordinate represents the main contribution to the modes under consideration.

It is now tempting to extend these correlations to other [NiFe] hydrogenases that have the same primary coordination shell but different amino acids in the immediate surroundings. As an example, we refer to the regulatory [NiFe] hydrogenase from *R. eutropha* for which the same states were recently probed by RR spectroscopy.<sup>16</sup> Despite the overall similarities in the band patterns, most of the bands are found at lower frequencies, partly by more than 20 cm<sup>-1</sup>, for the regulatory hydrogenase (Tables 2 and 3). This would correspond, for instance, to larger Fe–CN bond lengths and greater Fe–C–N bond angles in the Ni-L and Ni<sub>a</sub>-S states, respectively. Whether or not these correlations are of general applicability awaits to be investigated on the basis of further structural and spectroscopic data on related [NiFe] hydrogenases. Such an enlargement of the experimental data set may allow for extending the correlations to structural parameters of the surrounding protein. Thus, the Raman bands of the [NiFe] site as well as the CO and CN stretching modes probed by IR spectroscopy may turn out to be generally applicable spectral markers for monitoring structural details of the active sites of [NiFe] hydrogenases. In this way, the present study may contribute to the elucidation of the molecular mechanism of the catalytic process.

## ■ ASSOCIATED CONTENT

### 📄 Supporting Information

The Supporting Information is available free of charge on the ACS Publications website at DOI: 10.1021/acs.jpcc.5b04119.

Graphical presentations of the QM/MM structural models of the cofactors and experimental RR spectra of the Ni-L state. (PDF)

## ■ AUTHOR INFORMATION

### Corresponding Authors

\*Technische Universität Berlin, Institut für Chemie, Sekr. PC14, Straße des 17. Juni 135, D-10623 Berlin, Germany. E-mail: hildebrandt@chem.tu-berlin.de. Tel. +49-30-314-21419.

\*Technische Universität Berlin, Institut für Chemie, Sekr. PC14, Straße des 17. Juni 135, D-10623 Berlin, Germany. E-mail: ingo.zebger@tu-berlin.de. Tel. +49-30-314-26727.

### Author Contributions

‡E.S. and Y.R.: Equal contribution to the work.

### Notes

The authors declare no competing financial interest.

## ACKNOWLEDGMENTS

The work was supported by the cluster of excellence “Unifying Concepts in Catalysis”, funded by the Deutsche Forschungsgemeinschaft.

## REFERENCES

- (1) Lubitz, W.; Reijerse, E.; van Gastel, M. [NiFe] and [FeFe] Hydrogenases Studied by Advanced Magnetic Resonance Techniques. *Chem. Rev.* **2007**, *107*, 4331–4365.
- (2) de Lacey, A. L.; Fernandez, V. M.; Rousset, M.; Cammack, R. Activation and Inactivation of Hydrogenase Function and the Catalytic Cycle: Spectroelectrochemical Studies. *Chem. Rev.* **2007**, *107*, 4304–4330.
- (3) Fritsch, J.; Lenz, O.; Friedrich, B. Structure, Function and Biosynthesis of O<sub>2</sub>-Tolerant Hydrogenases. *Nat. Rev. Microbiol.* **2013**, *11*, 106–114.
- (4) Lubitz, W.; Ogata, H.; Rüdiger, O.; Reijerse, E. Hydrogenases. *Chem. Rev.* **2014**, *114*, 4081–4148.
- (5) Fritsch, J.; Scheerer, P.; Frielingsdorf, S.; Kroschinsky, S.; Friedrich, B.; Lenz, O.; Spahn, C. M. T. The Crystal Structure of an Oxygen-Tolerant Hydrogenase Uncovers a Novel Iron-Sulphur Centre. *Nature* **2011**, *479*, 249–252.
- (6) Frielingsdorf, S.; Fritsch, J.; Schmidt, A.; Hammer, M.; Löwenstein, J.; Siebert, E.; Pelmeshnikov, V.; Rippers, Y.; Lendzian, F.; Zebger, I.; et al. Redox-dependent Structural and Chemical Transformation of the [4Fe3S] Cluster in O<sub>2</sub>-Tolerant [NiFe] Hydrogenase. *Nat. Chem. Biol.* **2014**, *10*, 378–385.
- (7) Shomura, Y.; Yoon, K. S.; Nishihara, H.; Higuchi, Y. Structural Basis for a 4Fe-3S Cluster in the Oxygen-Tolerant Membrane-Bound NiFe-Hydrogenase. *Nature* **2011**, *479*, 253–256.
- (8) Volbeda, A.; Amara, P.; Darnault, C.; Mousesca, J. M.; Parkin, A.; Rössler, M. M.; Armstrong, F. A.; Fontecilla-Camps, J. C. X-Ray Crystallographic and Computational Studies of the O<sub>2</sub>-Tolerant [NiFe]-Hydrogenase 1 from *Escherichia coli*. *Proc. Natl. Acad. Sci. U. S. A.* **2012**, *109*, 5305–5310.
- (9) Saggi, M.; Zebger, I.; Ludwig, M.; Lenz, O.; Friedrich, B.; Hildebrandt, P.; Lendzian, F. Spectroscopic Insights into the Oxygen-Tolerant Membrane-associated [NiFe]-Hydrogenase of *Ralstonia eutropha* H16. *J. Biol. Chem.* **2009**, *284*, 16264–16276.
- (10) Goris, T.; Wait, A. F.; Saggi, M.; Fritsch, J.; Heidary, N.; Stein, M.; Zebger, I.; Lendzian, F.; Armstrong, F. A.; Friedrich, B.; Lenz, O. A Unique Iron-Sulfur Cluster is Crucial for Oxygen Tolerance of a [NiFe]-Hydrogenase. *Nat. Chem. Biol.* **2011**, *7*, 310–318.
- (11) Cracknell, J. A.; Wait, A. F.; Lenz, O.; Friedrich, B.; Armstrong, F. A. A Kinetic and Thermodynamic Understanding of O<sub>2</sub>-Tolerance in [NiFe]-Hydrogenases. *Proc. Natl. Acad. Sci. U. S. A.* **2009**, *106*, 20681–20686.
- (12) Wulff, P.; Day, C. C.; Sargent, F.; Armstrong, F. A. How Oxygen Reacts with Oxygen-Tolerant Respiratory [NiFe]-Hydrogenases. *Proc. Natl. Acad. Sci. U. S. A.* **2014**, *111*, 6606–6611.
- (13) Spiro, T.; Czernuszewicz, R.; Han, S. *Biological Applications of Raman Spectroscopy*; John Wiley & Sons, Inc: New York, 1988.
- (14) Siebert, F.; Hildebrandt, P. *Vibrational Spectroscopy in Life Science*; Wiley-VCH: Weinheim, 2007.
- (15) Siebert, E.; Horch, M.; Rippers, Y.; Fritsch, J.; Frielingsdorf, S.; Lenz, O.; Velazquez Escobar, F.; Siebert, F.; Paasche, L.; Kuhlmann, U.; et al. Resonance Raman Spectroscopy as a Tool to Monitor the Active Site of Hydrogenases. *Angew. Chem., Int. Ed.* **2013**, *52*, 5162–5165.
- (16) Horch, M.; Schoknecht, J.; Mroginski, M. A.; Lenz, O.; Hildebrandt, P.; Zebger, I. Resonance Raman Spectroscopy on [NiFe] Hydrogenase Provides Structural Insights into Catalytic Intermediates and Reactions. *J. Am. Chem. Soc.* **2014**, *136*, 9870–9873.
- (17) Shafaat, H. S.; Weber, K.; Petrenko, T.; Neese, F.; Lubitz, W. Key Hydride Vibrational Modes in [NiFe] Hydrogenase Model Compounds Studied by Resonance Raman Spectroscopy and Density Functional Calculation. *Inorg. Chem.* **2012**, *51*, 11787–11797.
- (18) Fritsch, J.; Löscher, S.; Sanganas, O.; Siebert, E.; Zebger, I.; Stein, M.; Ludwig, M.; de Lacey, A. L.; Dau, H.; Friedrich, B.; et al. [NiFe] and [FeS] Cofactors in the Membrane-Bound Hydrogenase of *Ralstonia eutropha* Investigated by X-Ray Absorption Spectroscopy: Insights into O<sub>2</sub>-Tolerant H<sub>2</sub> Cleavage. *Biochemistry* **2011**, *50*, 5858–5869.
- (19) Pelmeshnikov, V.; Kaupp, M. Redox-Dependent Structural Transformations of the [4Fe-3S] Proximal Cluster in O<sub>2</sub>-Tolerant Membrane-Bound [NiFe]-Hydrogenase: A DFT Study. *J. Am. Chem. Soc.* **2013**, *135*, 11809–11823.
- (20) Mroginski, M. A.; Mark, F.; Thiel, W.; Hildebrandt, P. Quantum Mechanics/Molecular Mechanics Calculation of the Raman Spectra of the Phycocyanobilin Chromophore in  $\alpha$ -C-Phycocyanin. *Biophys. J.* **2007**, *93*, 1885–1894.
- (21) Bleijlevens, B.; van Broekhuizen, F. A.; De Lacey, A. L.; Roseboom, W.; Fernandez, V. M.; Albracht, S. P. J. The Activation of the [NiFe]-Hydrogenase from *Allochromatium vinosum*. An Infrared Spectro-Electrochemical Study. *JBIC, J. Biol. Inorg. Chem.* **2004**, *9*, 743–752.
- (22) Nakamoto, K. *Applications in Coordination, Organometallic and Bioinorganic Chemistry*; John Wiley & Sons, Inc: New York, 2009.
- (23) Galinato, M.; Whaley, C.; Lehnert, N. Vibrational Analysis of the Model Complex [Fe(CO)<sub>3</sub>]<sub>2</sub> and Comparison to Iron-Only Hydrogenase: The Activation Scale of Hydrogenase Model Systems. *Inorg. Chem.* **2010**, *49*, 3201–3215.
- (24) Stromberg, C. J.; Kohnhorst, C. L.; van Meter, G. A.; Rakowski, E. A.; Caplins, B. C.; Gutowski, T. A.; Mehalko, J. L.; Heilweil, E. J. Terahertz, Infrared and Raman Vibrational Assignments of [FeFe]-Hydrogenase Model Compounds. *Vib. Spectrosc.* **2011**, *56*, 219–227.
- (25) Balzani, V.; Carassiti, V. *Photochemistry of Coordination Compounds*; Academic Press: London, NY, 1970.
- (26) Spearman, C. General Intelligence, Objectively Determined and Measured. *Am. J. Psychol.* **1904**, *15*, 201–292.
- (27) Mroginski, M. A.; Kaminski, S.; von Stetten, D.; Ringsdorf, S.; Gärtner, W.; Essen, L. O.; Hildebrandt, P. Structure of the Chromophore Binding Pocket in the Pr State of Plant Phytochrome PhyA. *J. Phys. Chem. B* **2011**, *115*, 1220–1231.
- (28) Salewski, J.; Velazquez Escobar, F.; Kaminski, S.; von Stetten, D.; Keidel, A.; Rippers, Y.; Michael, N.; Scheerer, P.; Piwowarski, P.; Bartl, F.; et al. The Structure of the Biliverdin Cofactor in the Pfr State of Bathy and Prototypical Phytochromes. *J. Biol. Chem.* **2013**, *288*, 16800–16814.
- (29) Pandelia, M. E.; Ogata, H.; Currell, L. J.; Flores, M.; Lubitz, W. Probing Intermediates in the Activation Cycle of [NiFe] Hydrogenase by Infrared Spectroscopy: the Ni-Sir State and its Light Sensitivity. *JBIC, J. Biol. Inorg. Chem.* **2009**, *14*, 1227–1241.
- (30) Pandelia, M. E.; Infossi, P.; Giudici-Orticoni, M. T.; Lubitz, W. The Oxygen-Tolerant Hydrogenase I from *Aquifex aeolicus* Weakly Interacts with Carbon Monoxide: An Electrochemical and Time-Resolved FTIR Study. *Biochemistry* **2010**, *49*, 8873–8881.
- (31) Osuka, H.; Shomura, Y.; Komori, H.; Shibata, N.; Nagao, S.; Higuchi, Y.; Hirota, S. Photosensitivity of the Ni-A state of [NiFe] Hydrogenase from *Desulfovibrio vulgaris* Miyazaki F with Visible Light. *Biochem. Biophys. Res. Commun.* **2013**, *430*, 284–288.
- (32) Ciaccafava, A.; Hamon, C.; Infossi, P.; Marchi, V.; Giudici-Orticoni, M. T.; Lojou, E. Light-Induced Reactivation of O<sub>2</sub>-Tolerant Membrane Bound Ni-Fe Hydrogenase from the Hyperthermophilic Bacterium *Aquifex aeolicus* under Turnover Conditions. *Phys. Chem. Chem. Phys.* **2013**, *15*, 16463–15467.



## 9 Appendix

```
1 !##### PROGRAMHEAD
2 #####
3
4 PROGRAM CORRELATION
5
6 ! This is a programm to calculate the pearson correlation coefficient
7 ! of
8 ! two given data sets x and y.
9
10 ! INPUT:
11 ! Datasets have to be delivered by anadditional file with the
12 ! following
13 ! format:
14
15 ! NELEMENTS (Number of elements that will be checked for correlation)
16 ! FILEx (Name of file that contains data set x)
17 ! FILEy (Name of file that contains data set y)
18
19 ! USAGE:
20 ! correlation.x < inputfile
21
22 ! OUTPUT:
23 ! MEANx | MEANY | STDEVx | STDEVy | SUMCOV*NELEMENTS | RHO | TVALUE(
24 ! NELEMENTS)
25
26 ! FORMULA used for pearson correlation coefficient RHO, TVALUE and
27 ! threshold for significance t-value T:
28
29 !
30 ! 
$$\text{RHO} = \frac{\text{SUMCOV}[(\text{DATAx}(i) - \text{MEANx}) * (\text{DATAy}(i) - \text{MEANY})]}{\text{SQRT}[\text{SUMSTDEVx} * \text{SUMSTDEVy}]}$$

31 !
32 ! 
$$\text{TVALUE} = \frac{\text{SQRT}(\text{DOF}) * \text{RHO}}{\text{SQRT}(1 - \text{RHO}^{**2})}$$

33 !
34 !
35 ! T = offset + A * exp(- DOF/B)
36 !
```

```

37 ! this exponential decay function is a fit to calculate the t-value for
    the
    ! threshold (to decide whether RHO is significant or not) for degrees
      of
39 ! freedom (DOF=NELEMENTS-2) between 30 and 100 as not all of them are
    ! given in a t-distribution table. They are fitted for a p-value of
      0.05
41 ! (5% probability that RHO occurred by chance).
    ! Fit values are: offset=1.658, A=0.12, B=27
43
45 ! NOTE:
47 ! There is also a shell script available (cor_coef; usage: cor_coef
    FILEx
    ! FILEy) which generates the input file and starts correlation.x
49 ! automatically
51 ! This source code is written by Yvonne Rippers.
53
55 !##### PROGRAMTAIL
    #####
57
59 !===== Definitions
    =====
61
63     IMPLICIT NONE
65     INTEGER :: NELEMENTS !sample size
67     INTEGER :: DOF !NELEMENTS -2
69     INTEGER :: i, j
71     REAL, DIMENSION(100) :: DATAx = 0, DATAy = 0
73     REAL, DIMENSION(100) :: COV = 0
75     REAL :: VALUE, SUMx, SUMy, SUMCOV, MEANx, MEANy
77     REAL :: SUMSTDEVx, SUMSTDEVy, STDEVx, STDEVy, RHO
79     REAL :: TVALUE, T
81     REAL, DIMENSION(30) :: TVALUE05 = 0 ! t-values for critical p-
    value of 0.05
83     REAL, PARAMETER :: offset = 1.658 ! parameter to approach
    critical
85     REAL, PARAMETER :: A = 0.12 ! t-value, if DOF is
    greater than
87     REAL, PARAMETER :: B = 27 ! 30
89     CHARACTER(len=40) :: FILEx, FILEy
91     CHARACTER(len=11) :: SIGNIFICANT
93
95 !----- needed formats
    -----
97
100     FORMAT(F12.6)
102
104     FORMAT(F9.2, ' | ', F9.2, ' | ', F9.2, ' | ', F9.2, ' | ', F9.2, ' | ',
    & F7.2, ' | ', F7.3, '(, I2, ) ', A11)

```

```

!----- initialize matrice for threshold t-values up to DOF = 30
-----
77
TVALUE05(1) = 6.314
79
TVALUE05(2) = 2.920
TVALUE05(3) = 2.353
81
TVALUE05(4) = 2.132
TVALUE05(5) = 2.015
83
TVALUE05(6) = 1.943
TVALUE05(7) = 1.895
85
TVALUE05(8) = 1.860
TVALUE05(9) = 1.833
87
TVALUE05(10) = 1.812
TVALUE05(11) = 1.796
89
TVALUE05(12) = 1.782
TVALUE05(13) = 1.771
91
TVALUE05(14) = 1.761
TVALUE05(15) = 1.753
93
TVALUE05(16) = 1.746
TVALUE05(17) = 1.740
95
TVALUE05(18) = 1.734
TVALUE05(19) = 1.729
97
TVALUE05(20) = 1.725
TVALUE05(21) = 1.721
99
TVALUE05(22) = 1.717
TVALUE05(23) = 1.714
101
TVALUE05(24) = 1.711
TVALUE05(25) = 1.708
103
TVALUE05(26) = 1.706
TVALUE05(27) = 1.703
105
TVALUE05(28) = 1.701
TVALUE05(29) = 1.699
107
TVALUE05(30) = 1.697

109 !===== Executions
=====
!----- get value for NELEMENTS and name of FILEx
-----
111
!      WRITE (*,*) 'gesamtzahl?'
113      READ (*,'(i3)') NELEMENTS
      IF ( NELEMENTS .GT. 100 ) THEN
115          WRITE (*,*) 'The delivered sample size', NELEMENTS,
&              'is greater than 100! Please contact programmer ',
117          &              '(Yvonne Rippers) or decrease number of elements.'
          STOP
119      ENDIF
!      WRITE (*,*) 'name FILEx?'
121      READ (*,'(A)') FILEx

```

```

123 !----- CONSTANT DATA SET X
      -----
124 !----- calculate mean value for data set x MEANx
      -----
125
126     OPEN (1, file=FILEx)
127
128     DO i=1, NELEMENTS
129         READ (1,10) VALUE
130         DATAx (i) = VALUE
131         SUMx = SUMx + VALUE
132     ENDDO
133
134     MEANx = SUMx / NELEMENTS
135
136 !----- calculate standard deviation for data set x STDEVx
      -----
137
138     DO i=1, NELEMENTS
139         SUMSTDEVx = SUMSTDEVx + ( DATAx (i) - MEANx )**2
140     ENDDO
141
142     STDEVx = SQRT(SUMSTDEVx / (NELEMENTS - 1))
143
144 !----- VARIABLE DATA SET Y -----
145 !----- read in variable data sets y from FILEy as long as input is
      given-----
146
147 50     READ (*,'(A)',end=100) FILEy
148         OPEN (2, file=FILEy)
149
150 !----- calculate mean value for data set y MEANy
      -----
151
152     SUMy = 0
153
154     DO i=1, NELEMENTS
155         read (2,10) VALUE
156         DATAy (i) = VALUE
157         SUMy = SUMy + VALUE
158     ENDDO
159
160     MEANy = SUMy / NELEMENTS
161
162 !----- calculate standard deviation for data set y STDEVy
      -----
163 !----- and covariance for data set x and y SUMCOV
      -----
164 !----- and pearsson correlation coefficient RHO
      -----

```

```

165      SUMSTDEVy = 0
167      SUMCOV = 0

169      DO i=1, NELEMENTS
          SUMSTDEVy = SUMSTDEVy + ( DATAy (i) - MEANy )**2
171          COV (i) = (DATAx (i) - MEANx) * (DATAy (i) - MEANy)
          SUMCOV = SUMCOV + COV (i)
173      ENDDO

175      STDEVy = SQRT(SUMSTDEVy / (NELEMENTS - 1))

177      RHO = SUMCOV / SQRT(SUMSTDEVx * SUMSTDEVy)

179      !----- calculate t-value
          -----

181      TVALUE = (SQRT(NELEMENTS - 2.0) * RHO)/SQRT( 1.0 - RHO**2 )

183      !----- test for significance
          -----

185      DOF = NELEMENTS - 2

187      IF ( DOF .GT. 30 ) THEN
          T = offset + A * EXP( - DOF/B )
189      ELSE
          T = TVALUE05(DOF)
191      ENDIF

193      IF ( ABS(TVALUE) .GE. T ) THEN
          SIGNIFICANT = "significant"
195      ELSE
          SIGNIFICANT = " "
197      ENDIF

199      !----- write results
          -----

201      WRITE (*,20) MEANx, MEANy, STDEVx, STDEVy, SUMCOV, RHO,
203      &TVALUE, NELEMENTS, SIGNIFICANT

205      CLOSE(2)

207      GOTO 50 !if there are more variable data sets y

209 100  CLOSE(1)

```

21 | END

source\_codes/correlation.f

```

2  #!/bin/bash
4  DATAx=$1
4  DATAy=$2
6  if [ $# -lt 2 ] ;
6  then echo "This script calculates the pearson correlation coefficient."
8      "
8      echo "Therefor two data sets x and y are needed!"
8      echo "Data set x?"
10     read DATAx
10     echo "Data set y?"
12     read DATAy
12 else TESTx=$(grep "" $DATAx | awk -F '\t' '{print $2}')
14     if [ "$TESTx" = "" ] ;
14         then DATAx=$1
16         else grep "" $DATAx | awk -F '\t' '{printf "%s \n",$2}' >
16         DATAx.tmp
16             DATAx=DATAx.tmp
18     fi
18     TESTy=$(grep "" $DATAy | awk -F '\t' '{print $2}')
20     if [ "$TESTy" = "" ] ;
20         then DATAy=$2
22         else grep "" $DATAy | awk -F '\t' '{printf "%s \n",$2}' >
22         DATAy.tmp
22             DATAy=DATAy.tmp
24     fi
24 fi
26
26 N_ELEMENTSx=$(cat $DATAx | wc -l) #Elemente einer Datei bestimmen
28 N_ELEMENTSy=$(cat $DATAy | wc -l) #Elemente einer Datei bestimmen
30
30 if [ "$N_ELEMENTSx" != "$N_ELEMENTSy" ] ;
32 then echo "Anzahl Elemente in $DATAx und $DATAy stimmt nicht überein!"
32     exit 1
34 else N_ELEMENTS=$N_ELEMENTSx
34 fi
36
36 cat > correlation_input <<END
38 $N_ELEMENTS
38 $DATAx
40 $DATAy
42 END

```

---

```
correlation.x < correlation_input
44
rm -f correlation_input
46 rm -f *.tmp
```

source\_codes/corcoef.sh



## Bibliography

- [1] R. Ahlrichs, M. Bär, M. Häser, H. Horn, and C. Kölmel, *Electronic structure calculations on workstation computers: The program system turbomole*, Chemical Physics Letters **162** (3), 165–169 (1989).
- [2] K. A. Bagley, E. C. Duin, W. Roseboom, S. P. J. Albracht, and W. H. Woodruffs, *Infrared-Detectable Groups Sense Changes in Charge Density on the Nickel Center in Hydrogenase from *Chromatium vinosum**, Biochemistry **34**, 5527–5535 (1995).
- [3] A. D. Becke, *Density-functional exchange-energy approximation with correct asymptotic behavior*, Phys. Rev. A **38** (6), 3098–3100 (1988).
- [4] J. Bley Müller, G. Gehlert, and H. Gülicher, *Statistik für Wirtschaftswissenschaftler*, Vahlen, 14 edn. (2004), 16 .
- [5] M. Brecht, M. Van Gastel, T. Buhrke, B. Friedrich, and W. Lubitz, *Direct Detection of a Hydrogen Ligand in the [NiFe] Center of the Regulatory H<sub>2</sub>-Sensing Hydrogenase from *Ralstonia eutropha* in Its Reduced State by HYSCORE and ENDOR Spectroscopy*, Journal of the American Chemical Society **125** (43), 13075–13083 (2003).
- [6] A. D. and Brooks, B. R. and Brooks, III, C. L. and Mackerell, Jr., Y. Nilsson, L. and Petrella, R. J. and Roux, B. and Won, Archontis, , L. G. and Bartels, C. and Boresch, S. and Caffisch, A. and Caves, , J. Cui, Q. and Dinner, A. R. and Feig, M. and Fischer, S. and Gao, J. Hodoscek, M. and Im, W. and Kuczera, K. and Lazaridis, T. and Ma, , C. B. and Ovchinnikov, V. and Paci, E. and Pastor, R. W. and Post, , R. M. Pu, J. Z. and Schaefer, M. and Tidor, B. and Venable, and M. Woodcock, H. L. and Wu, X. and Yang, W. and York, D. M. and Karplus, *CHARMM: The Biomolecular Simulation Program*, JOURNAL OF COMPUTATIONAL CHEMISTRY **30** (10, Sp. Iss. SI), 1545–1614 (2009).
- [7] M. Bruschi, M. Tiberti, A. Guerra, and L. De Gioia, *Disclosure of key stereoelectronic factors for efficient H<sub>2</sub> binding and cleavage in the active site of [NiFe]-hydrogenases*, Journal of the American Chemical Society **136**, 1803–1814 (2014).
- [8] D. A. Case, T. A. Darden, T. E. Cheatham, C. L. Simmerling, J. Wang, R. E. Duke, R. Luo, R. C. Walker, W. Zhang, K. M. Merz, B. Roberts, S. Hayik, A. Roitberg, G. Seabra, J. Swails, A. W. Goetz, I. Kolossváry, K. F. Wong, F. Paesani, J. Vanicek, R. M. Wolf, J. Liu, X. Wu, S. R. Brozell, T. Steinbrecher, H. Gohlke, Q. Cai, X. Ye, M. J. Hsieh, G. Cui, D. R. Roe, D. H. Mathews, M. G. Seetin, R. Salomon-Ferrer, C. Sagui, V. Babin, T. Luchko, S. Gusarov, A. Kovalenko, and P. A. Kollman, *AMBER 12* (2012).

- [9] S. Frielingsdorf, J. Fritsch, A. Schmidt, M. Hammer, J. Löwenstein, E. Siebert, V. Pelenschikov, T. Jaenicke, J. Kalms, Y. Rippers, F. Lenzian, I. Zebger, C. Teutloff, M. Kaupp, R. Bittl, P. Hildebrandt, B. Friedrich, O. Lenz, and P. Scheerer, *Reversible [4Fe-3S] cluster morphing in an O<sub>2</sub>-tolerant [NiFe] hydrogenase.*, *Nature Chemical Biology* **10**, 378–85 (2014).
- [10] M. J. Frisch, G. W. Trucks, H. B. Schlegel, G. E. Scuseria, M. A. Robb, J. R. Cheeseman, G. Scalmani, V. Barone, B. Mennucci, G. A. Petersson, H. Nakatsuji, M. Caricato, X. Li, H. P. Hratchian, A. F. Izmaylov, J. Bloino, G. Zheng, J. L. Sonnenberg, M. Hada, M. Ehara, K. Toyota, R. Fukuda, J. Hasegawa, M. Ishida, T. Nakajima, Y. Honda, O. Kitao, H. Nakai, T. Vreven, J. A. Montgomery Jr., J. E. Peralta, F. Ogliaro, M. Bearpark, J. J. Heyd, E. Brothers, K. N. Kudin, V. N. Staroverov, R. Kobayashi, J. Normand, K. Raghavachari, A. Rendell, J. C. Burant, S. S. Iyengar, J. Tomasi, M. Cossi, N. Rega, J. M. Millam, M. Klene, J. E. Knox, J. B. Cross, V. Bakken, C. Adamo, J. Jaramillo, R. Gomperts, R. E. Stratmann, O. Yazyev, A. J. Austin, R. Cammi, C. Pomelli, J. W. Ochterski, R. L. Martin, K. Morokuma, V. G. Zakrzewski, G. A. Voth, P. Salvador, J. J. Dannenberg, S. Dapprich, A. D. Daniels, i. Farkas, J. B. Foresman, J. V. Ortiz, J. Cioslowski, and D. J. Fox, *Gaussian09*.
- [11] J. Fritsch, P. Scheerer, S. Frielingsdorf, S. Kroschinsky, B. Friedrich, O. Lenz, and C. M. T. Spahn, *The crystal structure of an oxygen-tolerant hydrogenase uncovers a novel iron-sulphur centre*, *Nature* **479**, 249–252 (2011).
- [12] J. Fritsch, L. Simone, O. Sanganas, E. Siebert, I. Zebger, M. Stein, M. Ludwig, A. L. De Lacey, H. Dau, O. Lenz, and M. Haumann, *[NiFe] and [FeS] Cofactors in the Membrane-Bound Hydrogenase of Ralstonia eutropha Investigated by X-ray Absorption Spectroscopy: Insights into O<sub>2</sub> -Tolerant H<sub>2</sub> Cleavage*, *Biochemistry* **50**, 5858–5869 (2011).
- [13] R. P. Happe, W. Roseboom, A. J. Pierik, and S. P. J. Albracht, *Biological activation[!] of hydrogen*, *Nature* **385**, 126 (1997).
- [14] E. J. Heller, R. L. Sundberg, and D. Tannor, *Simple Aspects of Raman Scattering*, *Journal of Physical Chemistry* **86**, 1822–1833 (1982).
- [15] P. Hildebrandt and F. Siebert, *Vibrational Spectroscopy in Life Science*, Hildebrandt2007 (2007), 320 .
- [16] R. W. Hockney, *The potential calculation and some applications*, *Methods in Computational Physics* **9**, 135–211 (1970).
- [17] W. Koch and M. C. Holthausen, *A Chemist's Guide to Density Functional Theory*, Wiley-VCH, 2 edn. (2001), 1–309 .

- [18] W. Kohn and L. J. Sham, *Self-Consistent Equations Including Exchange and Correlation Effects*, Physical Review **140**, A1133–A1138 (1965).
- [19] H. A. KRAMERS, *No Title*, Z. Phys **30**, 521.
- [20] H. A. Kramers and W. Heisenberg, *Über die Streuung von Strahlung durch Atome*, Zeitschrift für Physik 681–708 (1925).
- [21] R. D. E. L. KRONIG, *ON THE THEORY OF DISPERSION OF X-RAYS*, J. Opt. Soc. Am. **12** (6), 547–556 (1926).
- [22] G. J. Kubas, *Fundamentals of H<sub>2</sub> binding and reactivity on transition metals underlying hydrogenase function and H<sub>2</sub> production and storage*, Chemical Reviews **107** (10), 4152–4205 (2007).
- [23] S. Kurkin, S. J. George, R. N. F. Thorneley, and S. P. J. Albracht, *Hydrogen-induced activation of the [NiFe]-hydrogenase from Allochromatium vinosum as studied by stopped-flow infrared spectroscopy*, Biochemistry **43**, 6820–6831 (2004).
- [24] A. L. de Lacey, E. C. Hatchikian, A. Volbeda, M. Frey, J. C. Fontecilla-Camps, and V. M. Fernandez, *Infrared-Spectroelectrochemical Characterization of the [NiFe] Hydrogenase of Desulfovibrio gigas*, Journal of the American Chemical Society **119**, 7181–7189 (1997).
- [25] C. Lee, W. Yang, and R. G. Parr, *Development of the Colle-Salvetti correlation-energy formula into a functional of the electron density*, Phys. Rev. B **37** (2), 785–789 (1988).
- [26] W. Lubitz, E. Reijerse, and M. van Gastel, *[NiFe] and [FeFe] hydrogenases studied by advanced magnetic resonance techniques.*, Chemical Reviews **107**, 4331–4365 (2007).
- [27] R. Mertens and A. Liese, *Biotechnological applications of hydrogenases*, Current Opinion in Biotechnology **15** (4), 343–348 (2004).
- [28] M. A. Mroginiski, F. Mark, W. Thiel, and P. Hildebrandt, *Quantum mechanics/molecular mechanics calculation of the Raman spectra of the phycocyanobilin chromophore in alpha-C-phycocyanin.*, Biophysical Journal **93**, 1885–1894 (2007).
- [29] M. Nonella, G. Mathias, and P. Tavan, *Infrared Spectrum of p-Benzoquinone in Water Obtained from a QM/MM Hybrid Molecular Dynamics Simulation*, Journal of Physical Chemistry A **107**, 8638–8647 (2003).
- [30] H. Ogata, S. Hirota, A. Nakahara, H. Komori, N. Shibata, T. Kato, K. Kano, and Y. Higuchi, *Activation process of [NiFe] hydrogenase elucidated by high-resolution X-ray analyses: Conversion of the ready to the unready state*, Structure **13** (11), 1635–1642 (2005).

- [31] H. Ogata, W. Lubitz, and Y. Higuchi, *[NiFe] hydrogenases: structural and spectroscopic studies of the reaction mechanism.*, Dalton Transactions **37**, 7577–7587 (2009).
- [32] H. Ogata, K. Nishikawa, and W. Lubitz, *Hydrogens detected by subatomic resolution protein crystallography in a [NiFe] hydrogenase*, Nature **520**, 571–574 (2015).
- [33] J. P. Perdew, *Erratum: Density-functional approximation for the correlation energy of the inhomogeneous electron gas*, Phys. Rev. B **34** (10), 7406 (1986).
- [34] W. L. Peticolas and T. Rush III, *Ab initio calculations of the ultraviolet resonance Raman spectra of uracil*, Journal of Computational Chemistry **16**, 1261–1270 (1995).
- [35] K. S. Pitzer, *Potential energies for rotation about single bonds*, Discussions of the Faraday Society **10**, 66 (1951).
- [36] P. L. Polavarapu, *Ab initio vibrational Raman and Raman optical activity spectra*, Journal of Physical Chemistry **94**, 8106–8112 (1990).
- [37] P. Pulay, G. Fogarasi, F. Pang, and J. E. Boggs, *Systematic ab Initio Gradient Calculation of Molecular Geometries, Force Constants, and Dipole Moment Derivatives*, Journal of the American Chemical Society **101**, 2550–2560 (1979).
- [38] J. A. Rice, *Mathematical Statistics and Data Analysis*, Pacific Grove, CA, 3 edn. (2007).
- [39] Y. Rippers, M. Horch, P. Hildebrandt, I. Zebger, and M. A. Mroginski, *Revealing the absolute configuration of the CO and CN- ligands at the active site of a [NiFe] hydrogenase*, ChemPhysChem **13** (17), 3852–3856 (2012).
- [40] T. Rush III, R. Kumble, A. Mukherjee, M. E. Blackwood, and T. G. Spiro, *Modeling the Soret-Resonant Raman Intensities of Metalloporphyrins and Heme Proteins. 1. Nickel Porphine*, Journal of Physical Chemistry **100**, 12076–12085 (1996).
- [41] M. Saggiu, M. Ludwig, B. Friedrich, P. Hildebrandt, R. Bittl, F. Lenzian, O. Lenz, and I. Zebger, *Impact of amino acid substitutions near the catalytic site on the spectral properties of an O<sub>2</sub>-tolerant membrane-bound [NiFe] hydrogenase.*, ChemPhysChem **11**, 1215–24 (2010).
- [42] M. Saggiu, I. Zebger, M. Ludwig, O. Lenz, B. Friedrich, P. Hildebrandt, and F. Lenzian, *Spectroscopic Insights into the Oxygen-tolerant Membrane-associated [NiFe] Hydrogenase of *Ralstonia eutropha* H16*, Journal of Biological Chemistry **284**, 16264–16276 (2009).
- [43] W. R. P. Scott, P. H. Hunenberger, I. G. Tironi, A. E. Mark, S. R. Billeter, J. Fennen, A. E. Torda, T. Huber, P. Kruger, and W. F. van Gunsteren, *The GROMOS Biomolecular Simulation Program Package*, Journal of Physical Chemistry A **103**, 3596–3607 (1999).

- [44] E. Siebert, M. Horch, Y. Rippers, J. Fritsch, S. Frielingsdorf, O. Lenz, F. Velazquezescobar, F. Siebert, L. Paasche, U. Kuhlmann, F. Lenzian, M. A. Mroginski, I. Zebger, and P. Hildebrandt, *Resonance Raman Spectroscopy as a Tool to Monitor the Active Site of Hydrogenases*, *Angewandte Chemie - International Edition* **52**, 5162–5165 (2013).
- [45] E. Siebert, Y. Rippers, S. Frielingsdorf, J. Fritsch, A. Schmidt, J. Kalms, S. Katz, O. Lenz, P. Scheerer, L. Paasche, V. Pelmeshikov, U. Kuhlmann, M. A. Mroginski, I. Zebger, and P. Hildebrandt, *Resonance Raman spectroscopic analysis of the [NiFe] active site and the [4Fe-3S] cluster of an O<sub>2</sub>-tolerant membrane-bound hydrogenase in the crystalline state*, *The Journal of Physical Chemistry* .
- [46] M. Stephenson and L. H. Stickland, *Hydrogenase: A bacterial enzyme activating molecular hydrogen. I. The properties of the enzyme*, *Biochemical Journal* (1931).
- [47] W. C. Swope, H. C. Andersen, P. H. Berens, and K. R. Wilson, *A computer simulation method for the calculation of equilibrium constants for the formation of physical clusters of molecules: Application to small water clusters*, *Journal of Chemical Physics* **76**, 637–649 (1982).
- [48] A. Volbeda, M. H. Charon, C. Piras, E. C. Hatchikian, M. Frey, and J. C. Fontecilla-Camps, *Crystal structure of the nickel-iron hydrogenase from *Desulfovibrio gigas**, *Nature* **373**, 580–587 (1995).
- [49] A. Volbeda, E. Garcin, C. Piras, A. L. D. Lacey, V. M. Fernandez, E. C. Hatchikian, M. Frey, and J. C. Fontecilla-camps, *Structure of the [NiFe] Hydrogenase Active Site: Evidence for Biologically Uncommon Fe Ligands*, *Journal of the American Chemical Society* **118**, 12989–12996 (1996).
- [50] A. Warshel and P. Dauber, *Calculations of resonance Raman spectra of conjugated molecules*, *Journal of Chemical Physics* **66**, 5477–5488 (1977).
- [51] E. B. Wilson and P. C. Cross, *Molecular Vibrations: The Theory of Infrared and Raman Vibrational Spectra (Dover Books on Chemistry)* (2001), 388 .



# Acknowledgement

Ich danke Peter Hildebrandt und Maria Andrea Mroginski sehr für die Möglichkeit, meine Doktorarbeit in ihren Arbeitsgruppen durchführen zu dürfen, und für die Freiheit bei der Themenwahl und Vorgehensweise zur Lösung von Problemen.

Bei Ingo Zebger, Tillmann Utesch, Elisabeth Siebert und besonders Marius Horch möchte ich mich für die intensive Zusammenarbeit und zahlreichen fruchtbaren Diskussionen bedanken.

Allen Freunden und Kollegen der Arbeitsgruppen von Peter Hildebrandt und Maria Andrea Mroginski danke ich sehr für das entspannte Klima am Arbeitsplatz.

Ganz besonders danke ich Johannes Salewski. Seine starke emotionale und tatkräftige Unterstützung hat sehr zur Erstellung dieser Arbeit beigetragen.

Dann danke ich meinen Eltern, ohne deren finanzielle Unterstützung das Studium der Chemie kaum möglich gewesen wäre. Besonders danke ich meinem Vater, der mir durch seinen Glauben an mich und meine Fähigkeiten den Mut und den Ehrgeiz gegeben hat, bis hierher zu kommen.

Cornelia Butzner-Salewski und Hans Detlef Butzner danke ich sehr für ihre liebevolle und herzliche Unterstützung in vielen, nicht immer guten, Lebenslagen während der Doktorarbeit.